ABSTRACT

Title of Thesis:	SEISMIC OBSERVATIONS OF FLUVIAL ENERGY DISSIPATION
	Phillip James Goodling, Master of Science, 2018
Thesis Directed By:	Dr. Karen Prestegaard, Department of Geology

Observing microseismic waves excited by turbulent flow is an emerging way to document river dynamics during extreme flood events. This thesis records fluvial-seismic observations in two contrasting systems at different scales. Two single-seismometer particle motion methods are introduced to characterize the seismic signal produced by rivers. In the large-scale system, the Oroville Dam spillway is observed when it is a simple rectangular channel and when it is damaged by erosion. The small-scale system is along the cobble-bed Northwest Branch of the Anacostia River. Particle motion analyses and the scaling between seismic power and discharge are suitable to characterize flow turbulence at the large-scale system. In the small-scale system, particle motion methods are found to be unsuitable and the scaling of seismic power is unable to resolve observed variability in flow dynamics within the study reach. This work suggests that methods of fluvial seismology are best suited to large-scale systems.

SEISMIC OBSERVATIONS OF FLUVIAL ENERGY DISSIPATION

by

Phillip James Goodling

Thesis submitted to the Faculty of the Graduate School of the
University of Maryland, College Park, in partial fulfillment
of the requirements for the degree of
Master of Science
2018

Advisory Committee:
Dr. Karen Prestegaard, Chair
Dr. Vedran Lekic
Dr. Daniel Lathrop

Dedication

To my loving boyfriend Adam, my biggest supporter through trials and triumphs alike.

Acknowledgements

This work was supported by the Maryland Water Resources Research Center (project ID: 2017MD341B) and by a 2017 Scholar Award from the Cosmos Club Foundation.

The author thanks the California Department of Water Resources for providing the LiDAR and discharge data used in this study and the Computational Infrastructure for Geodynamics (http://geodynamics.org), which is funded by the National Science Foundation under awards EAR-0949446 and EAR-1550901, for access to SPECFEM2D. Data from seismometer BK ORV is from the Berkeley Digital Seismic Network (BDSN), doi:10.7932/BDSN, operated by the UC Berkeley Seismological Laboratory, which is archived at the Northern California Earthquake Data Center (NCEDC), doi: 10.7932/NCEDC. The continuous color scales used in this thesis are perceptually uniform, developed by Peter Kovesi, and licensed under a Creative Commons license (Kovesi, 2015). The author thanks the Maryland National Capital Park and Planning Commission for permission research the Northwest Branch within Burnt Mills East Special Park.

The author thanks undergraduates Dakota Sparks and Kevin Mei (University of Maryland, College Park) and Anant Hariharan (Brown University) for providing field assistance at the Northwest Branch research site.

This thesis would not be possible without the incredible patience, support, and enthusiasm by Ved Lekic and Karen Prestegaard.

Table of Contents

List of Tables

List of Figures

in the colorbar coincides with the timing of the Oroville Dam crisis, and allows two distinct regimes to be identified. Seismic amplitudes are greater by ~0.5 μm s^{-1} after the uncontrolled channel erosion begins on February 7th, and remains greater even as discharge decreases to earlier levels, demonstrating that hysteresis is observed. This hysteresis is greatest in the 0.5-1 Hz frequency band. Note the changing x axis range in panels a through c.

Figure 8: Analysis of the relationship between mean dominant eigenvector power and discharge for the current analysis and two previous flood control release events is shown in 6a-6c. The discharge of each interval is shown in Figure 5d. The scaling exponent of seismic power with discharge before the flood control spillway erosion, $Q^{1.75}$, is more similar to the scaling observed with two prior release events with Q1.70 and $Q^{1.87}$ in 2006 and 2011, respectively, as compared to a power scaling of $Q^{3.26}$ following the development of the chasm from erosion.

Figure 9: Two polarization attributes for the five time intervals of interest are presented in two dimensional histograms. Dashed green lines in the first column of figures indicates the azimuth range of the spillway relative to the seismometer (See Fig. 3). Each hour within the time interval of interest has a polarization value at 7201 frequencies. These are distributed among 100 bins evenly spaced in frequency, and are shaded by normalized probability. The polarization attributes for the three intervals of interest after the spillway damage are similar, and differ dramatically from the attributes in the pre-crisis interval. Polarization attributes are interpretable only when the degree of polarization is sufficiently great (β^2>0.5). Regions shaded grey indicate frequencies at which β^2<0.5 and the values are not interpretable.

Figure 10: In the 5-10 Hz band, hourly mean azimuth ($\boldsymbol{\Theta_H}$) is displayed in Fig. 8a-c, with 95% error bars. The mean azimuth is highly variable for discharge less than 500 m3 s-1 for the flood control releases in 2017 (Fig. 8a), 2006 (Fig. 8b) and 2011 (Fig. 8c). In Figure 8a, during the "Pre-Chasm" time interval shaded green, the mean horizontal azimuth values point to the bottom of the flood control spillway (183°, see Figure 1c). After the high releases have formed a chasm that starts in the middle of the flood control spillway, the azimuths consistently point to the channel midpoint. The "Post-Chasm" azimuth when discharge is approximately 1400 m^3 s^{-1} is noticeably distinct from the "Pre-Chasm" flows around 1400 m^3 s^{-1}. During times when the channel is undamaged (Fig. 8b and Fig. 8c), the mean azimuth is sensitive to changes in discharge as turbulence develops in the middle of the flood control spillway. Due to the 180º indeterminacy, $\boldsymbol{\Theta_H}$ shown in this figure is constrained between 90º and 270º, the direction of the outflow channel.

Figure 11: Polarization attributes computed using FDPA of synthetic seismograms computed using SPECFEM2D are shown in 11a and 11c; with corresponding simulated topographies. The distributed source of the spillway is approximated by five sources spaced 100 meters apart with a source frequency of 5-10 Hz. Random noise was added to the results of the simulation to approximate background seismic noise. Fig 11a and 11b display the horizontal component seismic wavefield during a single time step in each simulation. In the flat topography simulation (Fig. 11a), the vertical-horizontal phase difference is closer to ±90° than in the simulation that includes the realistic hillslope topography (Fig. 11c). With a vertically incident force (0° source angle), the phase difference is lowest, while with increasing incidence angles, the vertical motion becomes less like a classical Rayleigh wave below 5 Hz.

Figure 12: Mean azimuths for the five time intervals of interest mapped onto aerial imagery reveal the Emergency Discharge, High Discharge, and Post-Chasm mean azimuths point to the top of the spillway damage, where a steep drop creates a waterfall. The location of the initial damage, shown as a triangle, is estimated from photographs of the damage (see supplement).

Chapter 1: Introduction

Motivation

Information on where and how rivers dissipate energy can be used to assess structures designed to restore rivers or mitigate floods. For example, this information can improve estimates of velocity, bed material erosion and transport, and flow behavior during floods. Average energy dissipation over a river reach is related to the turbulent intensity induced by the relative roughness of the streambed, resulting in potential and kinetic energy losses. These are quantified in fluvial geomorphology as the loss of potential energy per unit time (stream power) or as an empirical flow resistance parameter. To measure these parameters with high spatial and/or temporal resolution of these metrics, either in-stream measurements of velocity (for spatial resolution), or both discharge and water surface gradient (for temporal resolution) must be collected. Acquiring these data is labor-intensive and may be hazardous at high river discharges. Therefore, there is a paucity of data on the spatial distribution of energy dissipation during most flows and on the temporal evolution of energy dissipation during floods. In this thesis, I seek to improve fluvial-seismic methods, so that direct measurement of one form of dissipated energy (river-excited seismic energy) can better provide information on where and how rivers dissipate energy. In the first two chapters of this thesis, I introduce seismic analytical techniques new to fluvial seismology to evaluate a large-scale turbulent flow in a hydraulically engineered structure. In the third chapter, I observe a flashy and urbanized stream and explore the practical applicability of relating seismic observations to metrics of energy dissipation in this study environment.

Background

Energy Dissipation in Rivers

Characterizing energy dissipation in rivers is a classic problem in fluvial geomorphology and requires constraints spanning a broad range of spatial and temporal scales. Gravity acts upon water flowing in a river. Resisting this force are viscous forces of the fluid itself (kinematic viscosity) and resisting forces generated by the flow. These flow-generated resisting forces include the effect of turbulent fluctuations (eddy viscosity), which is related to the rate that momentum is transferred by eddies in the flow. They also include pressure gradients induced by roughness elements protruding into the flow. Additional forces including surface tension and centrifugal forces can also resist the force of gravity. Natural rivers contain fully turbulent flow, in which eddies transport energy between layers of different velocity. As an eddy transfers water from a region of low velocity to high velocity (and vice versa), momentum is transferred and energy is released.

Energy dissipation increases as features on the flow boundary generate turbulence or cause deviations from uniform flow; these features vary with bed grain size, channel shape, bed profiles, planform geometry, and other characteristics of the river (Powell, 2014; Leopold et al., 1960). A number of parameters have been developed to describe these sources of energy dissipation. Grain resistance (sometimes called skin resistance or skin friction) dissipates energy as individual roughness elements protrude into the flow and create a pressure gradient. The amount of grain resistance is determined by the size, shape, and spacing of the grains in the river. Grains or grain clusters significantly contribute to flow resistance in gravel-bed and boulder-bed streams where they are large enough to protrude beyond the thickness of the basal

laminar sublayer (Dingman, 1984). Stream beds with sand sized particles are deformed into ripples and dunes that contribute to form resistance (or form drag). Rivers also have larger morphological features that cause deviations from uniform flow and contribute to "internal distortion resistance" (Leopold et al., 1960). These features include gravel bars (e.g. Prestegaard, 1983), river meanders (e.g. Leopold et al., 1960), step-pool sequences (e.g. MacFarlane and Wohl, 2003), and woody debris (e.g. Curran and Wohl, 2003). Energy is expended as spill resistance by abrupt changes in flow at hydraulic jumps, flow separations, or waterfalls.

The above list of dissipative mechanisms is not exhaustive or mutually exclusive, but all transfer energy to dissipated forms such as heat, sound, sediment entrainment, and ground vibrations (seismic energy). At the reach scale, variability in dissipative mechanisms varies spatially, vertically through the water column, and temporally through flood events. For example, the presence of a gravel bar or other channel complexity may lead to a localized increase in energy dissipation (Figure 1). During flood events, a hydraulic jump may develop in a river section, greatly increasing energy dissipation at a threshold discharge.

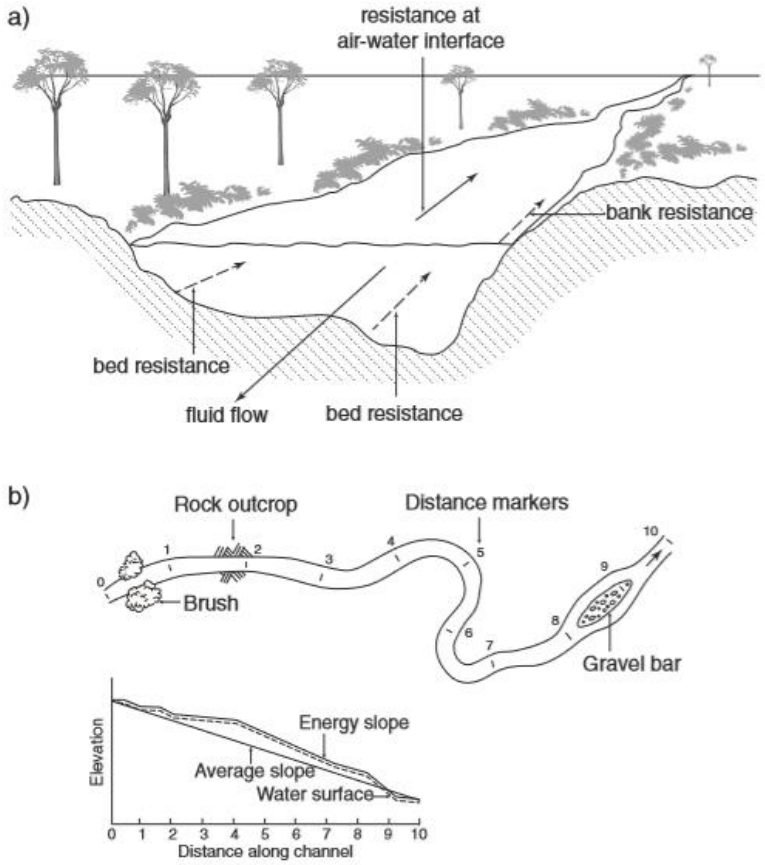

Figure 1: a) In fluvial geomorphology, a river's energy expenditure is typically characterized by flow resistance factors. b) The energy expenditure in a river is not uniform and is increased by features of the channel bed (bed particles, vegetation) and deviations from uniform flow such as large vegetation, channel bends, and gravel bars.

Previous work has suggested that the steady-state morphology of a river channel is achieved when energy is most evenly spatially dissipated throughout the reach at bankfull discharge, which is the discharge that performs the most morphological work. Langbein and Leopold (1964) hypothesized that the steady-state channel shape will minimize the variance of the channel widths, depths, and velocities in a reach. The cost of this spatial optimization for bankfull discharge is a higher overall energy dissipation at bankfull discharge and more spatially variable energy expenditure at lower discharge. At these lower discharges, channel features including bed particles and

bedforms provide energy dissipation as form drag. At bankfull discharge, these features are much less important because they are more submerged. While the partitioning of energy dissipation between types of flow resistance is largely unexplored in relation to the minimum variance hypothesis, it follows that at bankfull discharge the proportion of energy dissipation from spill resistance and internal distortion resistance becomes greater than at low flows.

Three measures of energy dissipation in fully turbulent flow near a boundary are 1) the ratio of the mean velocity ($\overline{U}$) and shear velocity (U*), 2) the unit stream power (ω) and 3) the basal shear stress (τ). Shear velocity is directly related to τ, and water density, ρ, as $u^* = \sqrt{\tau/\rho}$. For fully turbulent flow, the mean velocity of the flow increases with the logarithm of distance from the boundary (Dingman, 1984). This is formulated in the Prandtl-Von Kármán "Law of the Wall", stating that:

$$\overline{U}/_{U^*} = \frac{1}{\kappa}\ln\left(\frac{z}{z_0}\right) \qquad (1)$$

where $\overline{U}$ is the mean velocity, U^* is the shear velocity, κ is Von Kármán's constant (0.4 for a smooth wall), z is the height above the boundary, and z_0 is the distance from the boundary where velocity is zero. The value of z_0 is related to the roughness height, k_s. In natural rivers, k_s is taken to be D_{84} or some multiple of it due to the effects of clustering or bed topography. The shear velocity and shear stress are function of the increase in downstream velocity away from the boundary, therefore it represents the turbulent mixing of the flow generated by boundary roughness and is directly related to variations in the three dimensional velocity time series. The above formulation is appropriate for uniform turbulent flow and it does not incorporate internal distortion or

other contributions to turbulence and energy dissipation that are not components of the flow boundary. The value of the dimensionless velocity, $\overline{U}/_{U^*}$, decreases with greater energy dissipation.

The total $\overline{U}/_{U^*}$ of a river reach can be computed by separately evaluating the numerator ($\overline{U}$) and denominator (U^*). The cross-sectional averaged velocity ($\overline{U}$) can be calculated by dividing the discharge (Q) by the cross-sectional area (A). The mean shear velocity of a channel reach can be calculated by:

$$U^* = (gRS_e)^{0.5} \quad (2)$$

where S_e is the energy gradient, R is the hydraulic radius, and g is the acceleration due to gravity.

Stream power is the rate of energy expenditure (loss of potential energy) per unit channel length. It includes all forms of energy expenditure and its formulation assumes that the length of channel being examined has no significant water inputs and the flow is not accelerating in the channel reach. To account for changes in channel width, the stream power is often divided by channel width to obtain a unit stream power (ω) as:

$$\omega = \frac{\rho g Q S_e}{b} \quad (4)$$

Where g is the acceleration due to gravity, Q is the discharge, S_e is the energy gradient, and b is the channel width. Because the river slope varies as a flood wave passes through a channel reach, it will not have a constant relationship to discharge. However, most previous work investigating how unit stream power is related to

sediment transport during floods in natural rivers assumes a single constant value for energy gradient that is equal to the channel bed slope (i.e. Yang, 1974).

Fluvial Seismology

Fluvial seismology is an emerging approach to study dynamic geomorphological processes. The fluvial seismic approach seeks to characterize dynamic river processes by analyzing seismic waves excited by the flowing water and transported material. These tools have the distinct advantage of being remotely-deployable, do not have to contact the flow, and integrate flow information from across a channel section. They also have the potential to provide information on traditionally difficult-to-measure non-linear processes such as bedload transport and turbulent energy dissipation in rivers. However, they have the disadvantage of signal contamination by seismic energy from numerous environmental and anthropogenic sources. The challenges of using this approach include signal processing challenges to exclude unwanted seismic contributions and interpretative challenges in relating the seismic information back to concepts in fluvial geomorphology.

The excitation of seismic energy requires that fluctuating forces are applied to the ground surface (Figure 2). In open-channel turbulent flow, the fluctuating forces applied to the bed could be from a range of sources, including small turbulent eddies within the flow, large coherent flow structures, and fluid-air interactions from breaking waves (Gimbert et al., 2014). Fluctuating forces could also be from the intermittent impacts of material transported in the river transmitted through the river banks (Tsai et al., 2012). The frequency of the fluctuating forces determines the frequency at which seismic energy is excited.

The field of fluvial seismology has rapidly advanced over the last 10 years. Early work in the field focused on distinguishing the separate seismic contributions of river bedload and turbulent energy dissipation. Most of the prior observational work has focused on monitoring bedload transport in high gradient streams (e.g. Govi, et al., 1993; Burtin et al., 2008; Hsu, et al., 2011; Burtin et al., 2011; Roth et al., 2014; Roth et al., 2016; Roth et al., 2017, Anthony et al., 2018) or during controlled dam releases (Schmandt et al., 2013; Schmandt et al., 2017). In these early studies, hysteresis between the seismic amplitude and river discharge during storm events or dam releases is commonly observed and attributed to bedload transport. Some of these studies have included simultaneous bedload flux measurements and passive seismic monitoring in order to calibrate the relationship between hysteresis and bedload flux (Govi, et al., 1993; Roth et al., 2014; Roth et al., 2016)).

Two physical models have been put forward to predict the seismic power spectral density produced by saltating bedload (Tsai et al., 2012) and by turbulent flow over a rough bed (Gimbert et al., 2014). In the Tsai et al. (2012) model, bedload impacts are modeled as forces produced by each grain reaching its terminal velocity as it bounces along the riverbed. They integrate this force over all grain sizes in a log-normal distribution, and assume random impacts in time to create a force history within the river. Because vertical grain impacts are assumed, the analysis is conducted as if each impact is an impulse that generates a Rayleigh surface wave. In the Gimbert et al. (2014) model, the force history acting on the bed is integrated, using empirical turbulent scaling relationships based on the assumed velocity structure of the law of the wall for turbulent flows. In their model, only the energy dissipation by grain resistance is

considered. The pressure fluctuations applied on the bed are therefore strongly controlled by 1) the grain size distribution that generates the bed roughness and 2) the river depth (which is proportional to basal shear stress for a uniform channel with a constant gradient). When combined, these two models predict that the onset of bedload transport would generate hysteresis in the seismic amplitude- discharge relationship.

More recent work has shown that temporal changes in channel form may generate variability in the portion of the seismic energy attributed to the turbulently flowing water alone. Gimbert et al. (2016) observed seismic energy created by flow in subglacial conduits. Based on a dimensional analysis, they predict the scaling between discharge (Q) and seismic power (P) will be different if the ice conduit size adjusts to discharge compared to the scenario in which changes in discharge are entirely accommodated by increases in flow velocity (and thus turbulent intensity). At different times, their observed data from the Mendenhall Glacier in Alaska follow both scaling relationships, perhaps indicating different times when conduit adjustment is occurring. Recent work by Roth et al. (2017) suggests that hysteresis between seismic power and discharge may also result from riverbed particle rearrangement, which may change the energy dissipation by form drag before and after the flood wave. Anthony et al. (2018) observed a decrease in scaling between Q and P at high Q, for low frequency signals interpreted to be excited by macro turbulent eddies. The authors suggest that this mechanism scales strongly with river stage until bankfull stage, when out-of-bank flooding occurs.

The physical models that have been devloped in fluvial seismology have established a groundwork for interpreting the seismic energy produced by rivers.

However, there is as disconnect between observations of seismic energy and geomorphic theory about how energy is dissipated in rivers at the reach scale. To characterize the energy released by the turbulently flowing water, every study to date has compared the scaling of seismic observations to the river discharge. River discharge, however, is not a direct measure of the forces applied to the river bed. Comparing seismic energy to other metrics of energy dissipation such as shear stress, stream power, or measures of flow resistance would be more appropriate, since they may not scale directly with discharge when the river slope varies throughout the course of a flood.

If seismic techniques are able to observe the spatial and temporal variability of energy dissipation in rivers, they may help refine geomorphologic concepts. To date, only a few attempts to characterize the spatial location of seismic energy generated by turbulent flow have been undertaken. A study by Burtin, et al. (2010) developed noise correlation function envelopes to identify the segments of the Trisuli River that generated the most seismic energy at a given frequency. The greatest coherence between seismometer pairs (and inferred greatest seismic energy production) was located along river segments with the steepest river slopes and highest estimated incision rates. This approach is a promising one, though it requires an extensive array of seismometers. While Schmandt et al. (2017) and Anthony et al. (2018) have considered along-stream fluvial-seismic variability, more work is needed to assist in how these methods could be applied to improve geomorphic understanding.

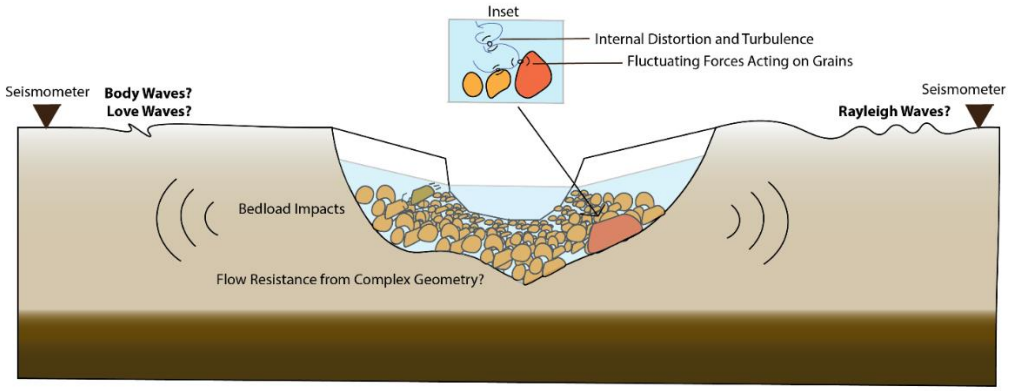

Figure 2: Fluctuating forces are applied to the bed excite seismic energy, which travels beyond the river banks.

Hypotheses

This thesis seeks to address two related hypotheses:

Hypothesis 1

When water flows continuously through an irregular channel, energy dissipation will be distributed unevenly. Uneven energy dissipation at the damaged Oroville Dam flood control spillway can be characterized with a single three-component seismometer using particle motion analysis. Frequency-Dependent Polarization Analysis (FDPA; Park et al., 1987) will characterize the location of greatest energy dissipation while Instantaneous Polarization Analysis (Morozov and Smithson, 1996) will characterize the spatial distribution of energy loss.

Hypothesis 2

Over the course of a flood, near channel seismometers will observe seismic signals related to temporal changes in energy dissipation in a river. The variations of seismic power and frequency will correlate better with the established metrics of fluvial

energy dissipation, shear stress, U/U* and unit stream power, than with river discharge alone.

Approach

This section describes the following chapters, which seek to address the above hypotheses. The chapters describe both an opportunistic study (the Oroville Dam spillway erosion crisis) and a designed study (Northwest Branch of the Anacostia River) that occur at different scales.

Chapter 2 describes the Oroville Dam Spillway Erosion Crisis, describes Frequency Dependent Polarization Analysis (FDPA; Park, Vernon, and Lindberg, 1987), and describes polarization attributes of the spillway-excited seismic energy in order to evaluate the first hypothesis. This chapter was published by Copernicus Publications in the journal Earth Surface Dynamics on May 9th, 2018 under a Creative Commons Attribution 4.0 License. The authors retain copyright, and the paper is reproduced here with full permission of the three authors. The supplemental materials to the paper are provided in Appendix A.

Chapter 3 is a reanalysis of the data presented in Chapter 2, to attempt to characterize the spatial distribution of energy loss along Oroville Dam's flood control spillway rather than only the location of greatest energy dissipation. In this chapter, the IPA method is introduced, a synthetic example distinguishes the method from FDPA, and the Oroville Dam dataset is analyzed and interpreted.

Chapter 4 presents data collected to test the second hypothesis. In this chapter, hydraulic and seismic data collected along an urbanized stream for a total of six months in 2017 and 2018. The data are analyzed to evaluate the along-stream variability of

fluvial energy dissipation. The scaling of seismic power with discharge, shear stress, U/U*, and stream power is examined to address the second hypothesis. FDPA is applied to the data to evaluate its performance in characterizing fluvial energy dissipation at the scale of a small river reach.

To conclude, I compile data reported in Chapter 2 from the Oroville Dam spillway and in Chapter 4 for the Northwest Branch of the Anacostia River along with data from for other studies to evaluate relationships between seismic power and unit stream power to evaluate the variation among fluvial-seismic studies.

Chapter 2: Seismic Signature of Turbulence during the 2017 Oroville Dam Spillway Erosion Crisis

Introduction

Dam spillways are typically designed with features, such as steps or changes in slope, that generate controlled turbulent eddies. These eddies entrain air into the flow, increase energy dissipation, and lower the mean flow velocity (Hunt and Kadavy, 2010a; Hunt and Kadavy, 2010b). Some of this dissipated energy is transferred as lift and drag forces to the bottom of the spillway channel. If a defect in the spillway channel is present, increased turbulence and associated forces can quickly enlarge the defect, eroding the spillway and underlying embankment (USBR, 2014). In some cases, erosion propagates headwards, undermining the structural integrity of the dam (USBR, 2014). Structural elements and routine maintenance are designed to minimize these channel defects, however, they can develop quickly during extreme flows. Therefore, real-time monitoring of spillway turbulence during times of high release could provide

early warning of the onset of erosion. Although turbulence can be characterized with photographic images or measurements of velocity time series with submerged or overhead instrumentation, these procedures may be impractical on large structures or during catastrophic events. Seismic monitoring may provide a way to continuously evaluate turbulent intensity and associated erosion from safely outside channels or hydraulic structures.

Seismic waves have previously been used to characterize the geotechnical suitability of earthen dams and internal dam seepage using passive seismic interferometry (e.g. Planès et al., 2016), but have not been used to characterize open-channel turbulence in dam spillways. Because turbulence affects erosional processes in both hydraulic structures and natural rivers, techniques from the seismic river monitoring (fluvial-seismic) literature provide guidance. In the past decade, many authors have used near-channel seismometers to monitor rivers during monsoons (e.g. Burtin et al., 2008); natural floods (e.g. Govi, et al., 1993; Hsu, et al., 2011; Burtin et al., 2011; Roth et al., 2016) and controlled floods (Schmandt et al., 2013; Schmandt et al., 2017). In many of these studies, the authors seek to separate the various sources of seismic energy, including precipitation, bedload transport, and flow turbulence (e.g. Roth et al., 2016). Bedload transport is traditionally difficult to monitor, therefore, research has been focused on isolating this source. Characterizing turbulence in rivers has been given less consideration in the fluvial-seismic literature, even though macroturbulent eddies place important controls on channel erosion (Franca and Brocchini, 2015) and may be important in spillway erosion. A forward mechanistic model by Gimbert, et al. (2014) estimates the power spectral density of seismic energy

produced by turbulently flowing water in a simple rectangular channel, in principle making it possible to use seismic data to invert for river depth and bed shear stress. This model, however, is based on assumptions of spatially uniform turbulence created by bed grain size; it ignores other sources of turbulence common in natural rivers and in engineered structures such as deviations from spatial uniformity. Recent work (Roth, et al., 2017) suggests that hysteresis between seismic power and discharge may also result from riverbed particle rearrangement, which leads to different turbulent characteristics within the flow. This fluvial seismic body of work suggests seismic monitoring may be able to resolve hydraulic changes in a dam spillway setting.

A near-spillway seismometer records seismic energy excited by a number of sources from different directions across a range of frequencies. These potential sources include primary and secondary microseisms, anthropogenic noise, wind, rain, earthquakes, and nearby rivers. Without a way to differentiate among these sources by direction and frequency, interpreting seismic observations will be limited. This challenge was highlighted by Roth et al. (2016) and Roth et al. (2017), who indicated that the turbulent signal from a waterfall downstream of their study river reach may have dominated the observed low-frequency signals. Previous studies have attempted to locate the source of fluvial seismic energy by using arrays of seismometers, primarily by observing the variability in seismic amplitudes around the river section of interest (Burtin et al., 2011, and Schmandt et al., 2017). A study by Burtin, et al. (2010) developed noise correlation function envelopes to identify segments of the Trisuli River that generated the most seismic energy at a given frequency. The greatest coherence between seismometer pairs (and inferred greatest seismic energy production) was

located along river segments with the steepest river slopes and highest estimated incision rates. This approach is a promising one, though it requires an extensive array of seismometers. A single-seismometer method for distinguishing various sources of seismic energy at different frequencies is more likely to be implemented in monitoring hydraulic structures and may be advantageous for fluvial seismic studies.

Discerning among seismic sources using a single station requires an evaluation of the three-dimensional ground motion recorded by a three-component seismometer. In traditional earthquake seismology, these motions indicate the arrival of body waves (P and S) and surface waves (Rayleigh and Love). For continuous ambient seismic sources such as turbulence, the phase relationships between the signals in each component can provide information on the wave type and its propagation direction. Several researchers have suggested that turbulence may excite Rayleigh surface waves whereas sliding and rolling bedload transport may excite Love surface waves, though these authors relied on comparing the seismic power of the three components rather than analyzing phase relationships among the components (Schmandt et al., 2013; Barrière et al., 2015; Roth et al., 2015). While recent forward models to estimate the power spectral density of seismic energy produced by moving bedload and turbulently flowing water can accommodate the excitation of various seismic waves, their applications to date assume that only Rayleigh waves are excited (Tsai et al., 2012; Gimbert et al., 2014). This assumption has not been quantitatively tested. Identifying the surface wave type excited by turbulent sources will help to identify the dominant mechanisms generating seismic waves in spillways and natural channels.

In this study we employ a single-seismometer method to observe variations in turbulence intensity and location within a dam spillway. Our goals are to 1) evaluate the scaling exponent between seismic power and discharge for different turbulence and channel roughness conditions; 2) determine if a single-seismometer source location technique can be used to resolve changes in the location of flow turbulence in a spillway channel; and, 3) evaluate the surface wave type excited by spillway turbulence and erosion. The study site is the flood control spillway of the Oroville Dam, California, USA. Seismic and discharge data collected during the erosional event that damaged the flood control spillway in February and March 2017 provide a natural experiment for this study, during which a simple and straight channel was abruptly eroded into a complex one.

Oroville Dam Crisis

The Oroville dam, located 100 km north of Sacramento, CA in the Sierra Nevada foothills, is the tallest dam in the United States (Fig. 3a). The dam spans the Feather River and provides hydroelectric power, flood control, and water storage for irrigation. Completed in 1968, the dam is constructed on Mesozoic volcanic rocks contained in the Smartville Complex (Saucedo and Wagner, 1992). The dam is built adjacent to the Long Ravine Fault; therefore, a permanent seismic station was placed approximately 2 km from the dam site in 1963 to monitor possible reservoir-induced earthquakes (Lahr et al., 1976). Several studies have linked the unusually large drawdown and refilling of the reservoir in 1974-1975 to a 5.7 magnitude earthquake on 1 August 1975 located 12 km south of the reservoir (Beck, 1976; Lahr et al., 1976). In 1992, the Berkeley Seismological Laboratory installed a Streckeisen STS-1 broadband

three-component seismometer at the site as station BK ORV (BDSN, 2017). We are not aware of any studies that have investigated ground motion generated by the flood control spillway.

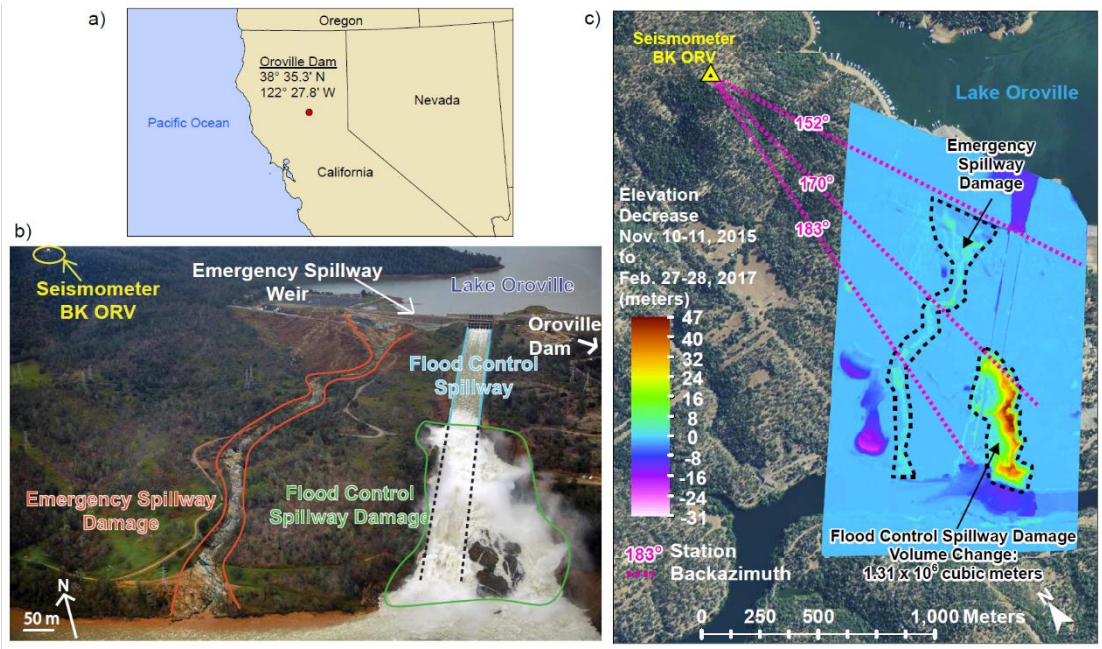

Figure 3: a) Location of the Oroville Dam in Northern California. b) The damage created along the Flood Control and Emergency Spillways of Oroville Dam in February and March, 2017. The seismometer used in this study is located approximately 2 km from the spillway. Photo credit: Dan Kolke, Department of Water Resources. Image taken on 2/15/2017. Estimated discharge during photograph is 2,800 m3 s-1. c) A digital elevation model created from LiDAR points provided by the California Department of Water Resources. The elevation difference from a November 2015 elevation survey and a late February 2017 survey shows that the crisis incised a chasm up to 47 m deep. The volume of the main chasm is 1.3×10^6 m^3. The incision resulting from the use of the emergency spillway is less than 20 m deep. The back-azimuth (clockwise from north) in degrees is displayed for the top of the flood control spillway, the top of the chasm, and the bottom of the flood control spillway. The seismometer is at an average 13º slope above the base of the flood control spillway and an average 8o slope above the top of the flood control spillway.

At approximately 9 am PST on February 7th, 2017, during a controlled dam release of approximately 1400 m^3 s^{-1}, a section of the concrete flood control spillway failed, leaving a defect in the spillway. A subsequent preliminary root cause analysis identified construction and maintenance flaws as the source of this initial defect (Bea, 2017; ODSIIFT, 2017a; ODSIIFT, 2017b). Ongoing heavy rainfall and runoff from the upstream watershed filled the reservoir to near capacity. Reservoir managers increased

the discharge through the damaged spillway in a series of tests and ultimately raised the discharge to over 1500 $m^3 s^{-1}$. This discharge and associated high flow velocities resulted in turbulent scour around the defect, rapidly eroding the underlying embankment and incising a gully that bypassed the concrete spillway channel. Dam managers then limited the flood control spillway discharge to below 1800 $m^3 s^{-1}$ (California Department of Water Resources, 2017a). High incoming discharge from the Feather River raised the reservoir level to capacity, which activated an emergency spillway weir for the first time in the dam's 48-year history.

Discharges up to 360 $m^3 s^{-1}$ flowed over the emergency spillway weir beginning at 8:00 am PST on February 11th while managers released approximately 1500 $m^3 s^{-1}$ through the primary flood control spillway. Within 32 hours, rapid erosion at the base of the emergency spillway weir threatened to compromise its stability, triggering concerns of catastrophic failure. Managers increased the discharge through the previously damaged flood control spillway to 3000 $m^3 s^{-1}$ and evacuated 180,000 people from the downstream city of Oroville, California. Elevated flood control spillway discharges lowered the reservoir level and stopped discharge through the emergency spillway weir on February 12th, 38 hours after activation. Elevated discharges continued through the damaged flood control spillway through the end of March, causing tens of meters of vertical incision into the weathered, sheared bedrock underlying the spillway (Bea, 2017). Figures 3b and 3c show the position of the seismometer and erosion incurred during the event. The seismometer is 1.4 km from the top of the flood control spillway channel and 1.9 km from the bottom of the channel. Using LiDAR data collected in 2015 and March 23rd, 2017, we compute that 1.3 x 10^6

m^3 of material were removed from the flood control spillway damage area during the crisis, resulting in a vertical incision into the hillside of up to 47 m (Fig. 3c; see Supplemental Information) (California Department of Water Resources, 2017b).

Methods

Data Collection and Approach

In this study, we evaluate seismic signals detected during the Oroville Dam Erosion Crisis at broadband seismometer BK ORV, operated by the Berkeley Digital Seismological Network (BDSN, 2017). We divide the crisis period into five time intervals of constant discharge, each of which is longer than 15 hours in duration (Fig. 4). During each of these discharge intervals, channel geometry and discharge remain similar, allowing us to document the differences across intervals in the spillway-generated seismic signal. The five time intervals of interest are:

1) "Pre-Chasm" interval: 18 hours of ~1400 m^3 s^{-1} routine flood control spillway release before the initial spillway damage on February 7th,
2) "Emergency Discharge" interval: 38-hour interval when the emergency spillway weir was active and ~1500 m^3 s^{-1} was released through the flood control spillway
3) "High Discharge" interval: 78-hour interval when ~3,000 m^3 s^{-1} were released through the damaged flood control spillway,
4) "Post-Chasm" interval: 87-hour interval of ~1400 m^3 s^{-1} discharge through the damaged flood control spillway, and
5) "Zero Outflow" interval: 93-hour interval of zero discharge through the flood control spillway, which serves as a control interval.

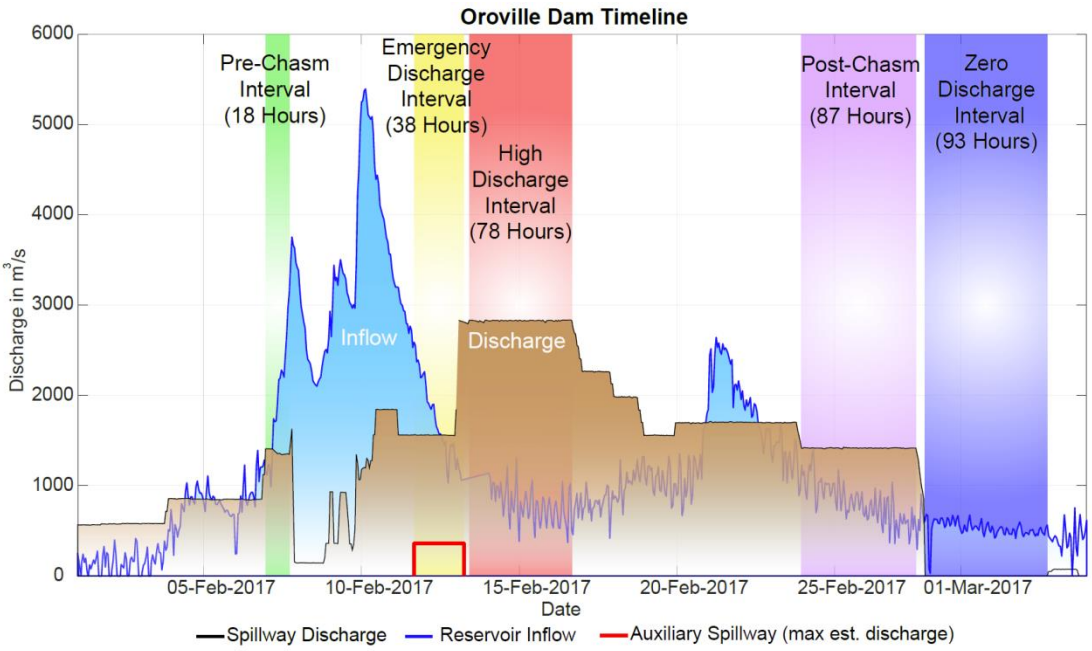

Figure 4: Discharge and inflow at Oroville Dam in early 2017, as reported by the California Department of Water Resources. The five time intervals of constant discharge in early 2017 used in this study are highlighted and labeled. The "Pre-Chasm" and "Post-Chasm" time intervals have approximately equal discharge, but very different channel geometries. Data gaps in discharge and inflow data are linearly interpolated in this figure. The inflows reported are from the Feather River to Lake Oroville. The discharge displayed for the emergency spillway weir is the maximum reported by CA DWR media updates, as no quantified measurements have been published for this data.

To encompass the erosion crisis period, we complied seismic data and spillway discharge data from 1/1/2017 to 4/1/2017. For comparison to the erosion crisis, we also compiled seismic data and spillway discharge for the second and third highest release periods during which continuous discharge and seismic data are available. These intervals are from 02/25/2006 to 03/18/2006 and 03/01/2011 to 06/01/2011. The seismic and discharge data for these intervals were processed identically to the 2017 data. The Northern California Earthquake Data Center is the source of the seismic data for this study and instrument response was causally removed (Haney et al., 2012). The California Department of Water Resources' California Data Exchange Center is the

source of all discharge data reported in this study (California Department of Water Resources, 2017c).

Frequency Dependent Polarization Analysis

We expect that contributions to spillway-generated seismic energy will produce energy across a range of frequencies, analogous to observations in natural channels (Gimbert et al., 2014). Energy sources in different frequency bands may also excite a variety of seismic wave types, which result in different ground particle motions and seismic amplitudes. We extract particle motion polarization attributes at each frequency by applying Frequency Dependent Polarization Analysis (FDPA) to the single-station three-component data (Park et al., 1987). The approach in this study is similar to ambient noise analysis applied to seismometer networks, in which the particle motion from ambient noise is characterized (e.g. McNamara and Buland, 2003; Koper and Hawley 2010; Koper and Burlacu, 2015). Following Koper and Hawley (2010), for each component (u_x, u_y, u_z), an hour of record (as ground velocity) is selected and divided into 19 sub-windows that each overlap 50%. Each sub-window is tapered with a Hanning window, converted to ground acceleration, and the Fourier transform is computed. At each frequency considered (up to the half the sampling frequency), the Fourier coefficients from each of three components are arranged into a 3x19 matrix, from which the 3x3 cross-spectral covariance matrix is estimated. The eigenvector corresponding to the largest eigenvalue of each 3x3 matrix describes the particle motion ellipsoid within the hour of observation at each frequency (Park et al., 1987). Henceforth, we refer to this as the dominant eigenvector. The complex-valued coefficients of this dominant eigenvector describe a particle motion ellipsoid at each

frequency, whose properties are analyzed in this paper. The time averaging inherent to this methodology minimizes the influence of transient seismic sources such as earthquakes or intermittent anthropogenic noise. The application of FDPA is useful for identifying polarization characteristics at a range of frequencies, yet for weakly polarized seismic energy the polarization attributes are highly variable with time. Therefore, it is more meaningful to analyze the probability distributions of polarization attributes in time intervals of strong seismic polarization (Koper and Hawley, 2010).

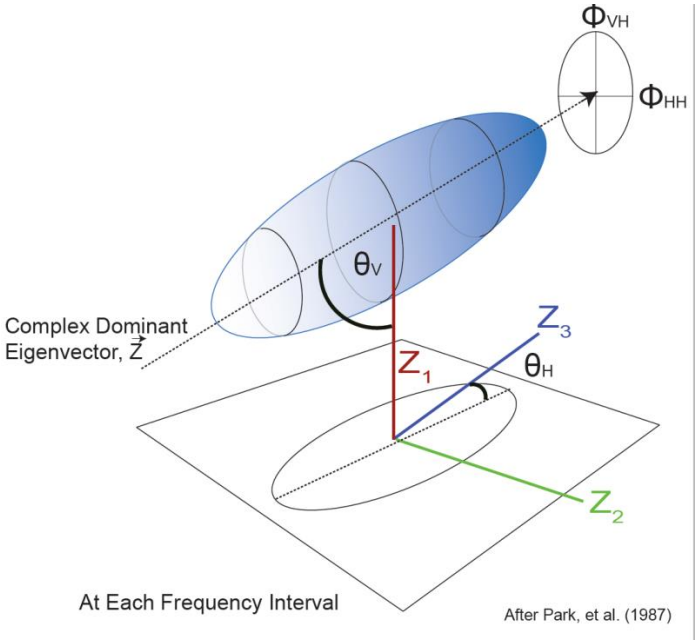

Figure 5: Diagram of particle motion defined by the dominant eigenvector. The particle motion at each frequency is analyzed by considering the dominant eigenvector of the spectral covariance matrix; the complex-valued components of this eigenvector can be visualized as describing a particle motion in an ellipsoid (Park, et al.,1987). The orientation of the eigenvector and the phase relationships between the components of the eigenvector yield the polarization attributes.

We compute the polarization attributes used in this paper from the complex components of the dominant eigenvector, $\vec{Z}$ [z_1, z_2, z_3] (Fig. 5). For the benefit of the reader, we briefly summarize their computation below and refer the reader to Park et al. (1987) for additional discussion. Each complex component of $\vec{Z}$ can be thought of

as describing the particle motion at a particular frequency in each of the three orthogonal directions. The azimuth (Θ_H) of the ellipsoid, measured clockwise-from-north, is determined by calculating the angle between the horizontal components of z_2 and z_3 on the real plane:

$$\Theta_H = \tan^{-1}\left[\frac{Re(z_3 e^{i\theta_h})}{Re(z_2 e^{i\theta_h})}\right], \quad (5)$$

where θ_h is the phase angle at which the horizontal acceleration is maximized:

$$\theta_h = -\frac{1}{2}\arg({z_2}^2 + {z_3}^2) + \frac{l\pi}{2} \quad (6)$$

where *l* corresponds to the smallest non-negative integer that maximizes the expression:

$$|z_2|^2 cos^2(\theta_h + \arg(z_2)) + |z_3|^2 cos^2(\theta_h + \arg(z_3)) \quad (7)$$

The range of Θ_H is restricted such that $0° < \Theta_H \leq 180°$ if $Re(z_1 z_3^*) < 0$ and $180° < \Theta_H \leq 360°$ if $Re(z_1 z_3^*) \geq 0$.

Analogously, the angle of incidence (Θ_V), measured from the vertical, is computed from the major axis of the particle motion ellipsoid by finding the angle on the real plane between the vertical axis, z_1, and the total horizontal acceleration, z_H:

$$\Theta_V = \tan^{-1}\left[\left|\frac{Re(z_1 e^{i\theta_v})}{Re(z_H e^{i\theta_v})}\right|\right], \quad (8)$$

where: $$z_H = \sqrt{z_2^2 + z_3^2} \quad (9)$$

and $\theta_v$is the phase angle at which total acceleration is maximized:

$$\theta_v = -\frac{1}{2}\arg({z_1}^2 + {z_2}^2 + {z_3}^2) + \frac{m\pi}{2} \quad (10)$$

where *m*, corresponds to the smallest non-negative integer that maximizes the expression:

$$|z_1|^2 cos^2(\theta_v + \arg(z_1)) + |z_2|^2 cos^2(\theta_v + \arg(z_2)) + |z_3|^2 cos^2(\theta_v + \arg(z_3)) \quad (11)$$

If $Im\left(\sqrt{{z_2}^2 + {z_3}^2}\right) < 0°$, the sign is reversed to restrict Θ_V such that $0° < \Theta_V \leq 90°$.

We consider two additional angles to describe the particle motion. First, the phase angle difference between the two horizontal components z_2 and z_3 (ϕ_{hh}) of the primary eigenvector, restricted to within -180° and 180°; and second, the vertical-horizontal phase angle difference (ϕ_{vh}), computed from the phase angle difference between θ_h (Eq. 2) and z_1, restricted to lie between -90° and 90°. Following Koper and Hawley (2010), we also compute the degree of polarization (β^2) defined by Samson (1983), which is zero when the three component eigenvalues are equal, and is one when the data are described by a single non-zero eigenvalue, such as for a single propagating seismic wave. We emphasize that FDPA methods characterize the dominant seismic source rather than describing the particle motion associated with all sources of seismic energy.

Results

In the following analysis, we present the polarization attributes in one hour intervals aligned with the hourly discharge data and assume each hour has a consistent seismic character. We then evaluate the variability of all of the hourly polarization attributes within each constant discharge time interval and throughout the dam erosion crisis.

Seismic Power Variation with Changing Spillway Discharge

We expect the seismic power generated by the flood control spillway to vary with spillway discharge. The power associated with the dominant eigenvector during

the five constant-discharge time intervals is shown in fig 6. In the figure, the mean hourly power values within each time interval are plotted with a one-standard-deviation envelope representing the variability in power within each constant-discharge interval. In all five time intervals of interest, a microseismic peak between 0.1 and 0.3 Hz is visible, consistent with the ocean-generated microseism (McNamara and Buland, 2004). Interestingly, there is greater "Pre-Chasm" power at frequencies below 0.05 Hz and around 0.25 Hz than the three time intervals after the chasm has developed. This may be attributable to variability in wave heights in the northern Pacific Ocean. The greatest difference between the "Zero Discharge" and all other time intervals is in the 0.5-5 Hz frequency range, with differences of up to ~30 dB between the "Zero Discharge" and "High Discharge" intervals. Spillway turbulence is therefore observable in this frequency band, even before the beginning of the erosion crisis. Between 0.5 and 1 Hz, the difference in power between the approximately equal discharge "Pre-Chasm" and "Post-Chasm" time interval is greatest, suggesting that increased turbulence resulting from the spillway damage is observable in this frequency band. In the rest of this study, we focus on this frequency range (0.5 to 1 Hz) to evaluate scaling in seismic power and discharge, though differences in the signal are visible across a broad frequency band (0.2 and 12 Hz). At 0.7 Hz, a peak is prominent in the "Post-Chasm" power, possibly reflecting that the "Post-Chasm" time interval has the most eroded and incised channel shape. These observations indicate seismic power during the five constant-discharge time intervals is sensitive to the turbulent intensity, as inferred from channel geometry.

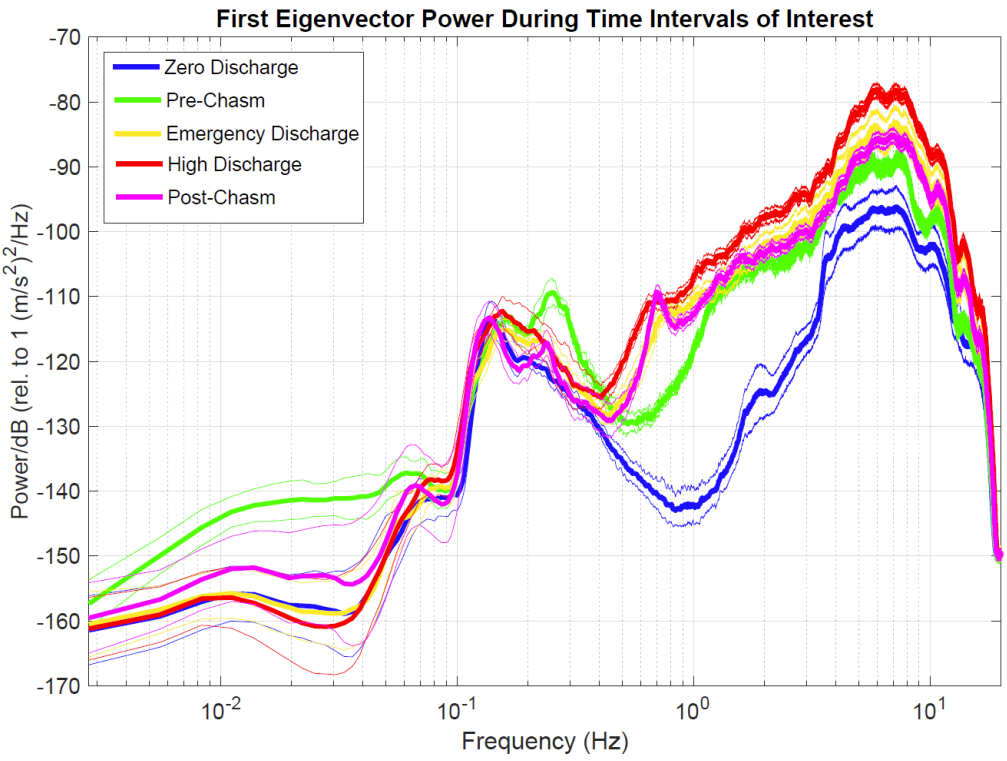

Figure 6: Power-per-frequency output for each of the five studied intervals, shown with one standard deviation error bars. There is a significant increase (up to 30dB) in the average power of this eigenvector during the four time intervals with discharge, particularly between 0.5 and 12 Hz. The power during three time intervals following spillway damage exceeds the 'Pre-Chasm' at frequencies above 0.5 Hz.

To further investigate the relationship between seismic power and variations in spillway discharge, we compute the hourly mean amplitude in the 0.5 to 1 Hz frequency band and compare it to discharge. In Fig. 7, the hourly mean amplitude of the dominant eigenvector is shown for the 2017 crisis period (Fig. 7a) and the 2006 and 2011 release periods (Fig. 7b and Fig. 7c). Figure 7d shows the release discharges of the 2017, 2006, and 2011 releases. Counterclockwise hysteresis is present in the 2017 period containing the erosion crisis, which is not present in 2006 or 2011 periods which maintain a consistent channel form.

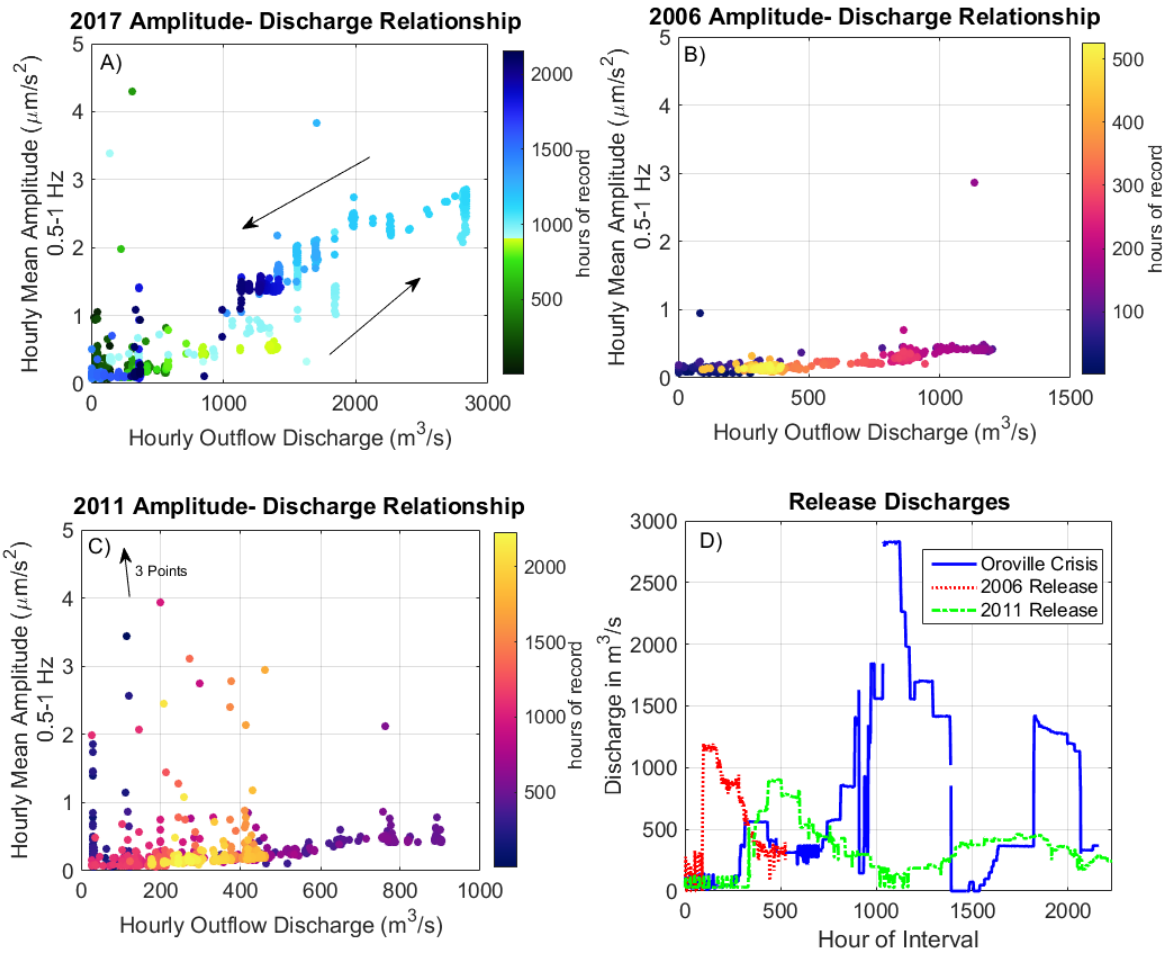

Figure 7: The plot of mean hourly amplitude of the dominant eigenvector in the 0.5-1 Hz frequency band vs hourly discharge shows that the two correlate strongly. The abrupt change in the colorbar coincides with the timing of the Oroville Dam crisis, and allows two distinct regimes to be identified. Seismic amplitudes are greater by ~0.5 µm s-1 after the uncontrolled channel erosion begins on February 7th, and remains greater even as discharge decreases to earlier levels, demonstrating that hysteresis is observed. This hysteresis is greatest in the 0.5-1 Hz frequency band. Note the changing x axis range in panels a through c.

In figure 8a, the hourly mean power of the dominant eigenvector is shown for the entire 2017 interval of record as a function of discharge. There is significant variability in hourly mean power for intervals with low discharge, possibly related to other sources of noise including anthropogenic noise created during spillway repair efforts, wind noise, or distant fluvial or marine sources. Below a discharge of approximately 200 m^3 s^{-1}, there does not appear to be a relationship between dominant

eigenvector power and discharge. We therefore interpret 200 m^3 s^{-1} as the threshold discharge above which signals emanating from the Oroville spillway become the dominant source of seismic. Figure S2 in the supplemental materials shows the dominant eigenvector power for all discharges. We limit our analysis of scaling between discharge and mean hourly eigenvector power to hours when discharge exceeded 200 m^3 s^{-1}, and to hours with spillway use as reported by the California Department of Water Resources. In figure 8a, the scaling relationship between discharge (Q) and power before the crisis is: $P_w \propto Q^{1.75}$. After the spillway defect occurs, the scaling exponent is greater, with $P_w \propto Q^{3.26}$. Figures 8b and 8c display the power-discharge relationships for the 2006 and 2011 release periods. The scaling exponent for these release events is similar ($P_w \propto Q^{1.70-1.87}$) to the pre-crisis scaling, though there is more scatter in the 2011 seismic record. The coefficients, exponents, and estimates of uncertainty are provided in Table 1. The change in the scaling relationship between discharge and seismic power is consistent with the inferred increase in turbulent energy dissipation following the damage to the flood control spillway (see discussion).

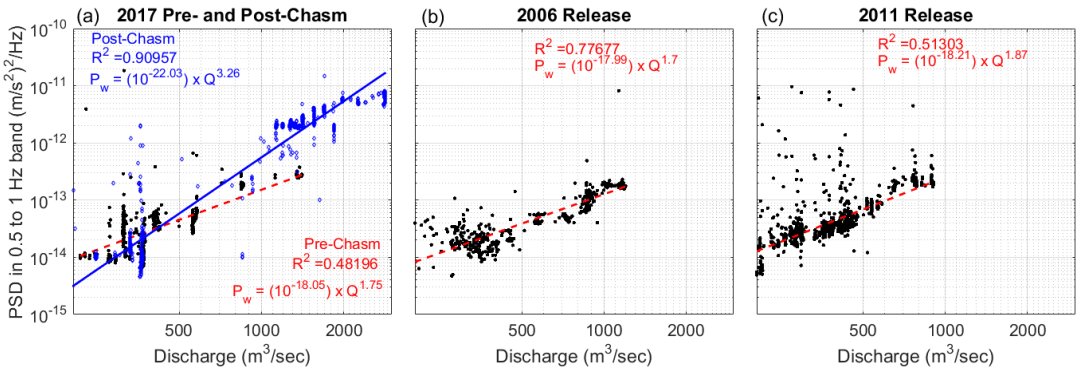

Figure 8: Analysis of the relationship between mean dominant eigenvector power and discharge for the current analysis and two previous flood control release events is shown in 6a-6c. The discharge of each interval is shown in Figure 5d. The scaling exponent of seismic power with discharge before the flood control spillway erosion, $Q^{1.75}$, is more similar to the scaling observed with two prior release events with $Q^{1.70}$ and $Q^{1.87}$ in 2006 and 2011, respectively, as compared to a power scaling of $Q^{3.26}$ following the development of the chasm from erosion.

		95% Confidence Intervals			95% Confidence Intervals	
Time Interval	Logarithm of Coefficient (Base 10)	Lower Bound	Upper Bound	Exponent	Lower Bound	Upper Bound
2017 Pre-Crisis	-18.055	-18.438	-17.671	1.7452	1.6016	1.8888
2017 Post-Crisis	-22.033	-22.225	-21.841	3.2602	3.1965	3.3238
2006 Release	-17.994	-18.225	-17.763	1.6994	1.6157	1.783
2011 Release	-18.207	-18.448	-17.967	1.8698	1.7776	1.962

Table 1: Coefficients, exponents, and uncertainty for power functions fit by least-square regression (shown in Fig. 8).

Polarization attributes

To examine the potential source of seismic waves across a range of frequencies, we display the azimuth and vertical-horizontal phase difference in fig.9 for the five time intervals of interest. All five polarization attributes are provided in the supplemental materials. To evaluate the variability of polarization within each constant discharge interval, the probability density functions (PDFs) of all the hourly polarization results are plotted together in fig. 9. In the figure, the polarization attributes are binned into 100 evenly-spaced frequency bins from 0.1 to 15 Hz and the PDFs are normalized so that within in each frequency bin, the probability sums to one. The brighter colors indicate highly focused attributes and the darker colors indicate broadly distributed attributes. When ground motion is insufficiently polarized, polarization attributes are not interpretable (Samson, 1983). We select a cutoff β^2 at 0.5 as our threshold criterion for interpreting polarization attributes; Koper and Hawley (2010)

selected a β^2 cutoff value of 0.6. Frequency ranges that are not interpretable by this criterion are shaded grey in figure 9.

The three time intervals after the spillway damage occurred ('Emergency Discharge', 'High Discharge', and 'Post-Chasm Discharge') display similar polarization attributes. The discharge through the emergency spillway weir, which reached a maximum of 360 m^3 s^{-1}, is masked by the ~1500 m^3 s^{-1} discharge in the primary spillway during this time (California Department of Water Resources, 2017d). When compared to the time intervals with discharge, the 'Zero Discharge' time interval contains less polarized three-component motion. Based on our threshold criterion, polarization attributes are not interpretable for a broad range of frequencies. At zero discharge, only polarization attributes at frequencies near 1 Hz, 4 Hz, and 10 Hz are interpretable, representing the ambient noise environment of the station. During the four intervals with non-zero discharge, a broad range of frequencies below 12 Hz are interpretable. There is a significant increase in polarization after the flood control spillway damage in a narrow frequency band around 0.7 Hz. From 1 to 5 Hz, the β^2 decreases from the "Pre-Chasm" discharge to the three "Post-Chasm" discharge intervals. The decrease in β^2 may be attributable to a mixing of seismic sources contributing to the ground motion (see discussion).

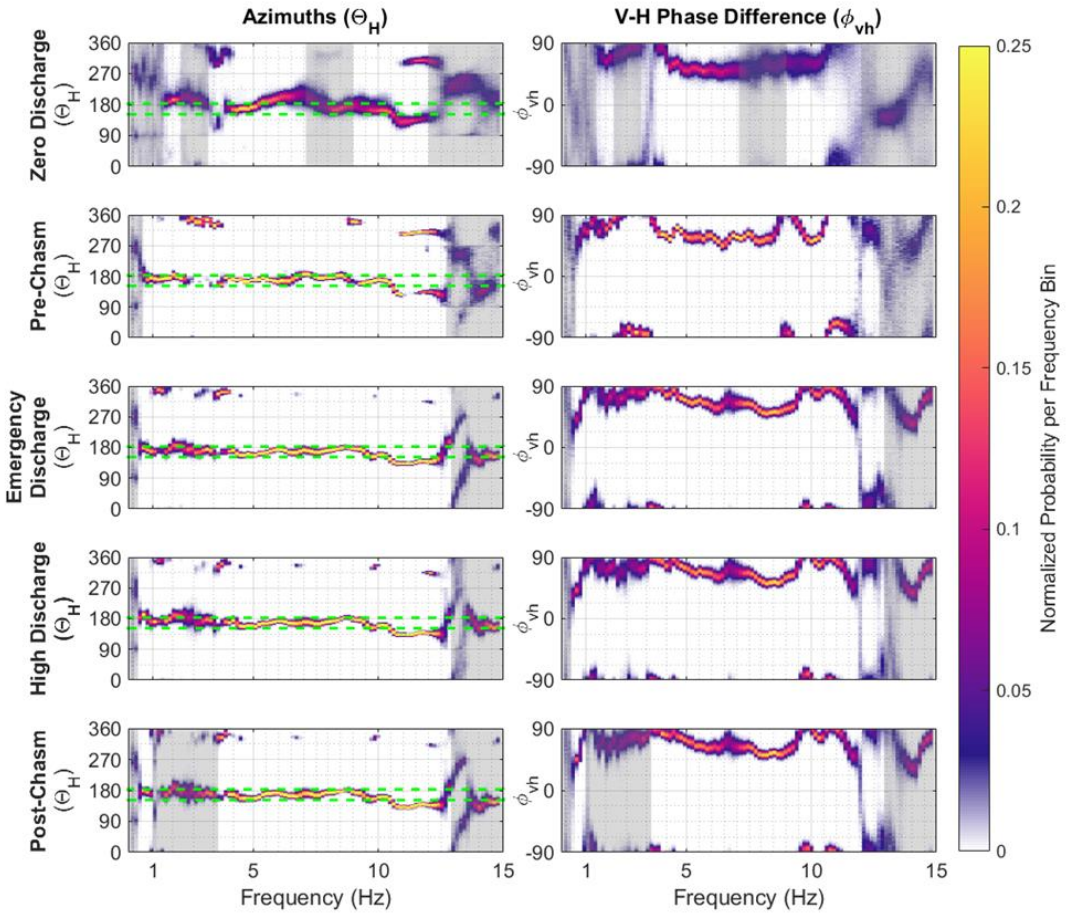

Figure 9: Two polarization attributes for the five time intervals of interest are presented in two dimensional histograms. Dashed green lines in the first column of figures indicates the azimuth range of the spillway relative to the seismometer (See Fig. 3). Each hour within the time interval of interest has a polarization value at 7201 frequencies. These are distributed among 100 bins evenly spaced in frequency, and are shaded by normalized probability. The polarization attributes for the three intervals of interest after the spillway damage are similar, and differ dramatically from the attributes in the pre-crisis interval. Polarization attributes are interpretable only when the degree of polarization is sufficiently great (β^2>0.5). Regions shaded grey indicate frequencies at which β^2<0.5 and the values are not interpretable.

Horizontal Azimuth

To resolve the potential changes in seismic source location resulting from the flood control spillway damage, we evaluate the horizontal azimuth, which is computed for each frequency bin in fig. 9. The horizontal azimuth (Θ_H) of the dominant particle motion ellipsoid represents the azimuth of the incoming wave if the motion is Rayleigh-like or a P-wave. Park et al. (1987) and Koper and Hawley (2010) caution interpreting

Θ_H as the azimuth if the horizontal-horizontal (ϕ_{hh}) phase difference is within 20° of ±90°, because the azimuth is not defined for a horizontal circular motion. At zero discharge, the horizontal azimuth is somewhat variable; multiple sources of seismic energy with equal amplitudes may be present in the absence of spillway discharge (Fig. 9). During the time intervals with spillway discharge, horizontal azimuth is generally consistent from 5-8 Hz, then it stair-steps to lower azimuths at frequencies near 10 Hz.

In order to compute summary statistics of the horizontal azimuth, we select a frequency band of 5-10 Hz. This band has a degree of polarization above 0.5 for all time intervals with discharge and has a horizontal phase angle difference (ϕ_{hh}) outside of 20° from 90°/-90 (for which the azimuth is not defined). As directional data such as azimuth require special statistical treatment, we employ the CircStat Matlab toolbox for circular statistics to compute an hourly mean azimuth with 95% confidence intervals (Berens, 2009). Due to the 180° ambiguity in azimuth estimates, we consider valid any mean azimuths that lie between 90° and 270°, and add or subtract 180° from the mean azimuths that lie outside these bounds. This choice is supported by the strong relationship observed between power and changes in discharge which indicate that the flood control spillway channel (between 152° and 183°) is the primary seismic source across a broad range of frequencies **(**See Fig. 3c). We compute the uncertainty on the mean using 2000 random bootstrap samples with replacement. Table 2 displays the mean 5-10 Hz azimuth within each time interval, with 95% confidence interval error bars. Figure 8a displays the average hourly 5-10 Hz Θ_H as a function of flood control spillway discharge, with hourly 95% confidence intervals for the 2017 period. For

comparison, fig. 10b and 10c display the same data for the 2006 and 2011 release periods.

Time Interval	5-10 Hz Mean Θ_H (deg.)	Lower 95% CI (deg.)	Upper 95% CI (deg.)
Zero Discharge	186.76	186.67	186.87
Pre-Chasm	174.28	174.16	174.38
Emergency Discharge	169.11	169.05	169.17
High Discharge	169.78	169.73	169.82
Post-Chasm	168.96	168.92	169.00

Table 2: Distribution statistics for the mean azimuth within the five time intervals of interest. The 95% confidence intervals (CI) on the mean are determined by collecting 2000 random bootstrap samples with replacement.

At low spillway discharges, the horizontal azimuth values are variable but generally point southward towards the Feather River and town of Oroville (183° to 250°), whereas during time intervals with elevated discharge the azimuth values point more consistently toward the flood control spillway channel, centered at 171°. During times when the spillway is undamaged, the hourly mean azimuth changes systematically with spillway discharge above about 500 m^3 s^{-1}. The hourly mean azimuth moves from the base of the flood control spillway towards the middle of the spillway with increasing discharge. After the erosion damage begins (Fig. 10a), the azimuths point more towards the top of the chasm, where a large waterfall develops as a result of the erosion damage. Above 1000 m^3 s^{-1}, the azimuths point consistently to the middle of the outflow channel. The azimuths around a discharge of 1400 m^3 s^{-1} are different before the erosion crisis occurred (bright green shading) and after a chasm is present (dark blue shading). This distinction indicates that the FDPA-derived azimuths

are sensitive to changes in the turbulence regime under normal spillway operation and when erosion damage is present (see discussion).

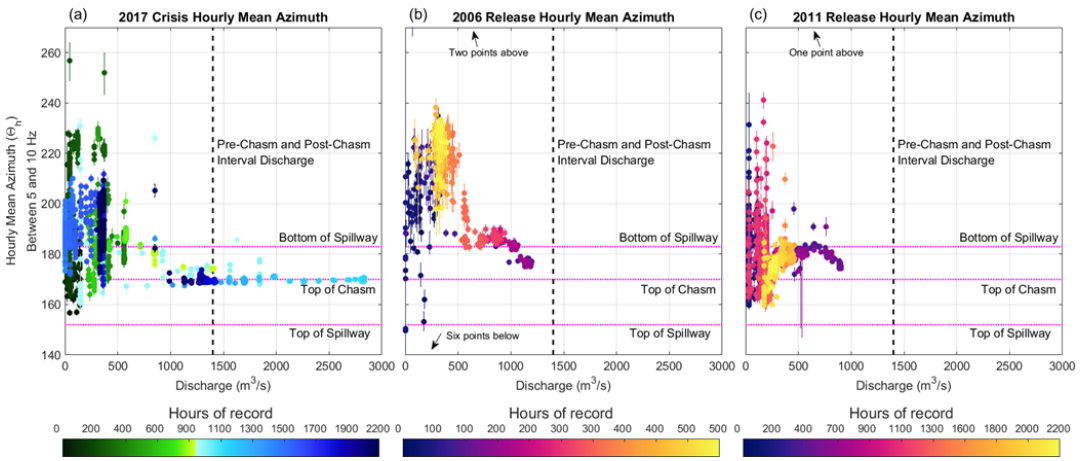

Figure 10: In the 5-10 Hz band, hourly mean azimuth (Θ_H) is displayed in Fig. 8a-c, with 95% error bars. The mean azimuth is highly variable for discharge less than 500 m3 s-1 for the flood control releases in 2017 (Fig. 8a), 2006 (Fig. 8b) and 2011 (Fig. 8c). In Figure 8a, during the "Pre-Chasm" time interval shaded green, the mean horizontal azimuth values point to the bottom of the flood control spillway (183°, see Figure 1c). After the high releases have formed a chasm that starts in the middle of the flood control spillway, the azimuths consistently point to the channel midpoint. The "Post-Chasm" azimuth when discharge is approximately 1400 m3 s-1 is noticeably distinct from the "Pre-Chasm" flows around 1400 m3 s-1. During times when the channel is undamaged (Fig. 8b and Fig. 8c), the mean azimuth is sensitive to changes in discharge as turbulence develops in the middle of the flood control spillway. Due to the 180º indeterminacy, Θ_H shown in this figure is constrained between 90º and 270º, the direction of the outflow channel.

Incident Angle

The vertical angle of the dominant eigenvector represents the incidence angle of the incoming wave for body waves or tilt of elliptical motion for Rayleigh waves. Park et al. (1987) and Koper and Hawley (2010) caution interpreting this metric if ϕ_{vh} is within 20° of ±90°, because the vertical incidence angle of vertical circular motion is not defined. At a broad range of frequencies this criterion is not met during time intervals with discharge (see discussion). In all five time intervals of interest, the Θ_V values are highly variable (see supplemental material).

Vertical-Horizontal Phase Difference

To evaluate the possible surface wave type (i.e. Rayleigh or Love), we assess the vertical-horizontal phase difference. For a Rayleigh wave in an isotropic medium, the vertical-horizontal phase difference will be ±90°. In certain anisotropic structures, the vertical-horizontal phase difference for a Rayleigh wave will deviate from ±90° (Crampin, 1975). In fig. 9, the vertical-horizontal phase angle (ϕ_{vh}) is consistently near ±90° for frequencies below 5 Hz when discharge is occurring, which is consistent with a Rayleigh-like wave. At frequencies of up to 8 Hz, which account for most of the power, there is a decreasing vertical-horizontal phase angle to approximately 50°. At 8 Hz, the vertical-horizontal phase angle is 50° in the "Pre-Chasm" time interval and near 90° in the "Post-Chasm" time interval. These deviations from ±90° are unexpected and explored in the discussion.

Horizontal Phase Difference

For all of the time intervals of interest, the ϕ_{hh} is between ±180° and ±90° for most frequencies, suggesting horizontal elliptical particle motion. At 8 Hz, the "Pre-Chasm" and "Post-Chasm" time intervals seem to change from near -180° to near -115° phase difference, suggesting a change from linear horizontal motion to more elliptical horizontal motion at frequencies near 8 Hz.

Topographic Effects on Vertical-Horizontal Phase Angle

We observe consistent deviations from the expected vertical-horizontal phase difference of ±90° between 5 and 10 Hz, even during the "Pre-Chasm" interval (Fig. 9). To investigate the possible reasons behind these deviations, we consider the effect of the irregular hillside topography on the polarization results by computing synthetic

seismograms using the 2D spectral-element solver package SPECFEM2D 7.0.0 (Tromp et al., 2008; Komatitsch et al., 2012). All geospatial data were processed in ESRI ArcMap 10.4. First, a 2013 ⅓ arc-second resolution digital elevation model was acquired from the USGS National Elevation Dataset at www.nationalmap.gov. The raster was reprojected to Universal Transverse Mercator Zone 10N to acquire northing and easting coordinates in a conformal (angle-preserving) coordinate system. Elevation data (in m, NAVD 88) were extracted from each grid cell along a profile line between top of the spillway erosion damage and the seismometer in this study. The topographic profile was meshed into the model domain using the built-in xmeshfem2d program. To minimize model boundary effects, the lower model boundary extends over 4 km below the surface. We also generated a rectangular model grid with a flat surface in SPECFEM2D for comparison. We select a density of 2700 kg m^{-3}, increase P wave velocity linearly with depth from 4 km s^{-1} at the surface to 6 km s^{-1} at 4 km depth, and assume a Poisson solid.

In both the topographic and flat surface simulations, continuous signals were used as the seismic source, and were applied independently at five locations spaced 100 meters apart and representing a spatially distributed source along the Oroville flood control spillway channel projected onto a 2D profile line (See Supplemental Materials Fig. S3). Each independent source consists of a four-minute random signal varying between 0 and 1 filtered using a second order Butterworth filter between 5 and 10 Hz. Deviations from Rayleigh-like wave polarizations are observed at these frequencies (fig. 9). The angle of incidence of the continuous seismic source was varied between 0°, 45°, and 90° with respect to the vertical. Synthetic seismograms were simulated at

the location of the BK ORV seismometer, with random noise added to the resulting synthetic seismograms to approximate background seismic sources. As the simulations are carried out in a 2D geometry, the results may only be used to evaluate the effect of topography on vertical-horizontal phase differences. The results of the simulations show that for vertically incident fluctuating forces applied along the Oroville flood control spillway , the particle motion is Rayleigh-like (vertical-horizontal phase difference is near ±90°) for a flat topography (Fig. 11a). As the fluctuating force is applied at angles of 45° and 90° to the surface, the vertical-horizontal phase becomes less Rayleigh-like below 5 Hz. Realistic topography also appears to significantly affect the particle motion, which becomes less Rayleigh-like, as vertical-horizontal phase differences decrease from ±90° to ±45° between 5 and 10 Hz (Fig. 11c). This is consistent with the conversion of Rayleigh energy to body-waves as the seismic waves propagate up a non-uniform slope (e.g. McLaughlin and Jih, 1986).

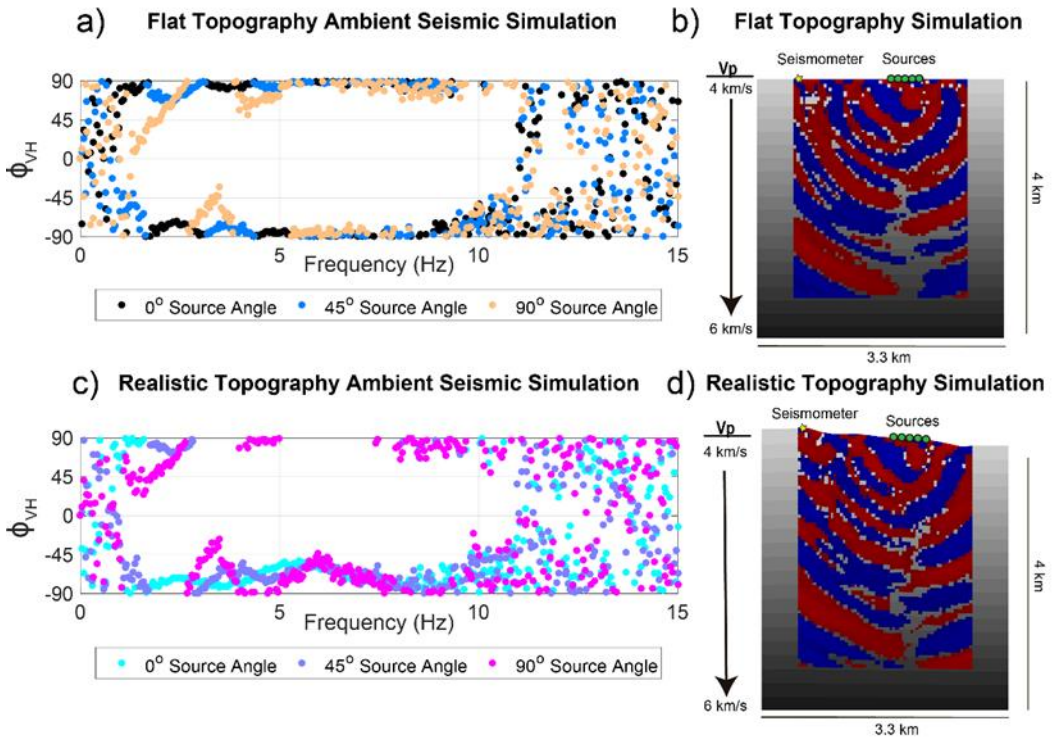

Figure 11: Polarization attributes computed using FDPA of synthetic seismograms computed using SPECFEM2D are shown in 11a and 11c; with corresponding simulated topographies. The distributed source of the spillway is approximated by five sources spaced 100 meters apart with a source frequency of 5-10 Hz. Random noise was added to the results of the simulation to approximate background seismic noise. Fig 11a and 11b display the horizontal component seismic wavefield during a single time step in each simulation. In the flat topography simulation (Fig. 11a), the vertical-horizontal phase difference is closer to ±90° than in the simulation that includes the realistic hillslope topography (Fig. 11c). With a vertically incident force (0° source angle), the phase difference is lowest, while with increasing incidence angles, the vertical motion becomes less like a classical Rayleigh wave below 5 Hz.

Discussion

The changing geometry of the flood control spillway and the increase in flow turbulence during the Oroville Dam Erosion Crisis are reflected in the FDPA results, most notably in dominant eigenvector power and horizontal azimuth. During the crisis, large volumes of material (1.3 x 10^6 m^3 according to our analysis of LiDAR data) were transported, which previous work has shown can contribute to the overall sesimic signal (Tsai, et al., 2012). Therefore, one might expect bedload transport to be the dominant source of seismic energy. Yet, there are compelling lines of evidence that suggest that the majority of the signal is flow or turbulence-generated. The fastest rate of material

transport on the Oroville flood control spillway was likely during the early part of the crisis timeline. Water entering the flood control spillway is from the surface of the reservoir. Unlike a natural river, it does not carry bedload or coarse suspended sediment, so any transported material must be entrained from the spillway itself or the adjacent hillside. Early in the Oroville dam crisis, weathered saprolite and concrete blocks were undercut and eroded, while later in the crisis, the water from the spillway flowed over harder volcanic rocks. If the seismic signal was generated by a transient transport pulse, we would expect a rapid jump and decay in the amplitude of the seismic waves coming from the spillway. If greater erosion occurred at the beginning of the crisis and if transported material were the primary source of the seismic energy, we would expect clockwise power-discharge hysteresis (higher energy dissipation with rising discharge) in this system. Instead, we observe counterclockwise hysteresis in this relationship, which suggests that energy dissipation increased due after erosion increased bed complexity and turbulence. Although our analysis does not enable us rule out all other seismic sources such as material transport, we think that the changes in FDPA results are consistent with changes in the turbulent flow regime caused by erosional changes in channel geometry.

Counterclockwise hysteresis in the discharge-power relationship is consistent with the increased channel roughness and larger size of macroturbulent eddies resulting from the Oroville Dam erosion crisis. Because of the dissimilarity of the system to a natural channel, we are unable fully to implement theoretical models of fluvial seismic energy generation, but we are able to examine whether the scaling relationships within these models are consistent with our data. The theoretical scaling relationship between

water-generated vertical component power (P_W) and discharge (Q) for water turbulence alone with a simple channel geometry is $P_W \propto Q^{1.25}$(Gimbert et al., 2014; Gimbert et al., 2016). Roth et al. 2017, found a $P_W \propto Q^{1.49-1.93}$ in the 35 - 55 Hz band. In the 0.5 to 1 Hz band for the smooth channel (2006, 2011, and pre-crisis 2017) the observed scaling of dominant eigenvector power and turbulence is $P_W \propto Q^{1.69-1.88}$, similar to the scaling observed by Roth et al. 2017. After the spillway erosion crisis, the scaling exponent is much higher ($P_W \propto Q^{3.28}$). We observe similar scaling relationships for the vertical component power (without polarization analysis); the power function relationships for 2006, 2011, and pre-crisis 2017 data scale as $P_W \propto Q^{1.74-1.98}$ and the post-crisis 2017 scaling relationships is $P_W \propto Q^{3.26}$.

The increased scaling exponent following the crisis likely corresponds to the addition of new sources of turbulent energy dissipation generated from the rougher channel morphology associated with exposed bedrock and waterfall. For a uniform turbulent flow, as expected in the hydraulically smooth, constant-width channel geometry present during the 2005-2006 flood, discharge is log-linearly related to flow depth according to the Law of the Wall and ground motion is generated by fluctuating forces applied by scaled eddies within the flow, analogous to the processes described by Gimbert et al. (2014). After damage is created in the channel, several mechanisms likely increase the energy dissipated by the flow at a given discharge. The first is that the erosion damage introduced a steep vertical drop in the base of the channel, developing a waterfall. A waterfall will violate assumptions in the Gimbert et al. (2014) model formulation and lead to greater water velocities (from free fall) impacting the bed than would be found in a continuous turbulent channel flow. Second, the irregular

channel shape resulting from erosion provides obstructions to the flowing water that create local pressure gradients around the obstacles. These pressure gradients cause a deflection in the flow and an increase in the shearing between flows of different velocities, increasing the energy dissipated by the turbulence in the flow. Third, erosion during the 2017 event incised a 47-meter-deep, V-shaped channel, which increased flow depths for the same discharge and changed the distribution of shear stresses applied to the bed. Greater flow depths would also allow for larger eddies to form. Our results suggest that the additional energy dissipated by these forms of turbulence is observed as an increase in the scaling relationship between discharge and seismic power. Our observations support the use of the exponent in the $P_W \propto Q$ power function to observe changing channel geometries in supply-limited fluvial systems (as in Gimbert et al., 2016), but are unable to identify a particular source mechanism.

The FDPA polarization attributes reveal the seismic character of open channel turbulent flow, which is distinct from the background seismic character ('Zero Discharge' interval) across a broad range of frequencies (fig. 9; supplemental material). The three time intervals with discharge following the flood control spillway damage have similar polarization attributes, while the "Pre-Chasm" time interval is identifiable by a higher degree of polarization at frequencies below 3 Hz, and the absence of a 0.7 Hz sharp peak in dominant eigenvector power (fig. 6) and degree of polarization. The decrease in degree of polarization is consistent with mixed seismic waveforms from multiple sources (Rayleigh, Love, P, and S) being introduced by the chasm channel complexity and increased turbulent energy dissipation. We are unable to attribute a source to the 0.7 Hz anomaly, but we note that around 0.7 Hz we observe azimuths of

about 180°, an incidence angle of about 25° from vertical, a vertical-horizontal phase difference about 45°, and broadly distributed horizontal-horizontal phase difference. The azimuth is consistent with the base of the flood control spillway, though the vertical incidence is steeper than the 13° slope of the hillside.

The greatest hysteresis in the power and discharge relationship is observed at low frequencies (0.5 to 1 Hz), however, the greatest hysteresis in azimuth is observed at higher frequencies (5-10 Hz). This difference may be due to the greater sensitivity to source location that is provided by the higher frequencies, which have shorter wavelengths. For a Rayleigh wave traveling through rock at approximately 3 km s^{-1}, the wavelength of a 0.5-1 Hz wave is 6 km to 3 km, significantly longer than the 1 km long flood control spillway, meaning that changes in source location along the spillway may not be observable in azimuths computed at low frequencies. However, at 5 to 10 Hz, the wavelength is 0.6 to 0.3 km, which is sufficient to identify distinct segments of the flood control spillway.

The hourly 5-10 Hz mean azimuths (fig. 10) are sensitive to changes in discharge even when no damage is present (fig 10b and 10c). Aerial photographs of the spillway at a range of discharges reveal that the location of the transition from smooth to visibly white and aerated turbulent flow in the bottom half the spillway is sensitive to changes in discharge (See fig. S5 in the supplement). In the dam engineering literature, the onset of surface turbulence is referred to as the inception point and represents where the turbulent boundary layer reaches the free surface (Hunt and Kadavy, 2010). The aerated flow region downstream of the inception point indicates increased energy dissipation. Due to the geometry of the spillway channel with respect

to the seismometer, as the inception point moves up the spillway channel it approaches the seismometer. We expect the closest portion of the aerated flow region to be the largest source of seismic energy under undamaged conditions; seismic energy excited further from the seismometer will be subject to more geometrical spreading and attenuation.

The hourly 5-10 Hz mean azimuths are also sensitive to changes throughout the dam erosion crisis. During the 2017 period, the 'Pre-Chasm' and 'Post-Chasm' time intervals have a statistically significant difference in mean azimuth of 5.32°. The 'Emergency Discharge', 'High Discharge', and 'Post-Chasm' time intervals have mean azimuths within a 1° range. To interpret these results, we reviewed available aerial photography throughout the Oroville Crisis and extracted an elevation profile along the length of the flood control spillway using the LiDAR measurements provided by the CADWR. The imagery review reveals that the top of the erosion damage propagated upstream a distance of approximately 120 meters (approx. 2.8° azimuth) between February 7th and February 27th-28th (fig. 12). The upstream end of the erosion damage forms a waterfall. FDPA results from the 'Emergency Discharge', 'High Discharge', and 'Post-Chasm' time intervals are able to identify the waterfall at the top of the erosion damage. The 'Emergency Discharge' time interval has an azimuth within 1° of the immediately following 'High Discharge' interval, indicating that 360 $m^3 s^{-1}$ released through the emergency spillway did not generate sufficient energy to mask the concurrent flood control spillway releases at that time.

The particle motion of seismic waves produced by the Oroville dam spillway is mostly Rayleigh-like, particularly at frequencies below 3 Hz, though we also observe

consistent deviation from the expected Rayleigh ϕ_{vh} values (-90° and 90°) at frequencies from 5-10 Hz. This could be explained by the presence of anisotropy (Crampin, 1975) or Love and/or body waves, which induce shifts in ϕ_{vh} but our SPECFEM2D modeling indicates that realistic topography is also a viable explanation for the polarization attributes we observe, noticeably ϕ_{vh}. Therefore, our analysis is limited to time-varying changes in polarization attributes rather than interpreting the surface and/or body waveforms created by the flood control spillway. We see the greatest difference in ϕ_{vh} and ϕ_{hh} between the "Pre-Chasm" and "Post-Chasm" time intervals below 3 Hz and in the 9-11 Hz band, potentially indicating that more Rayleigh energy is produced at these frequencies after the channel geometry becomes more eroded and incised.

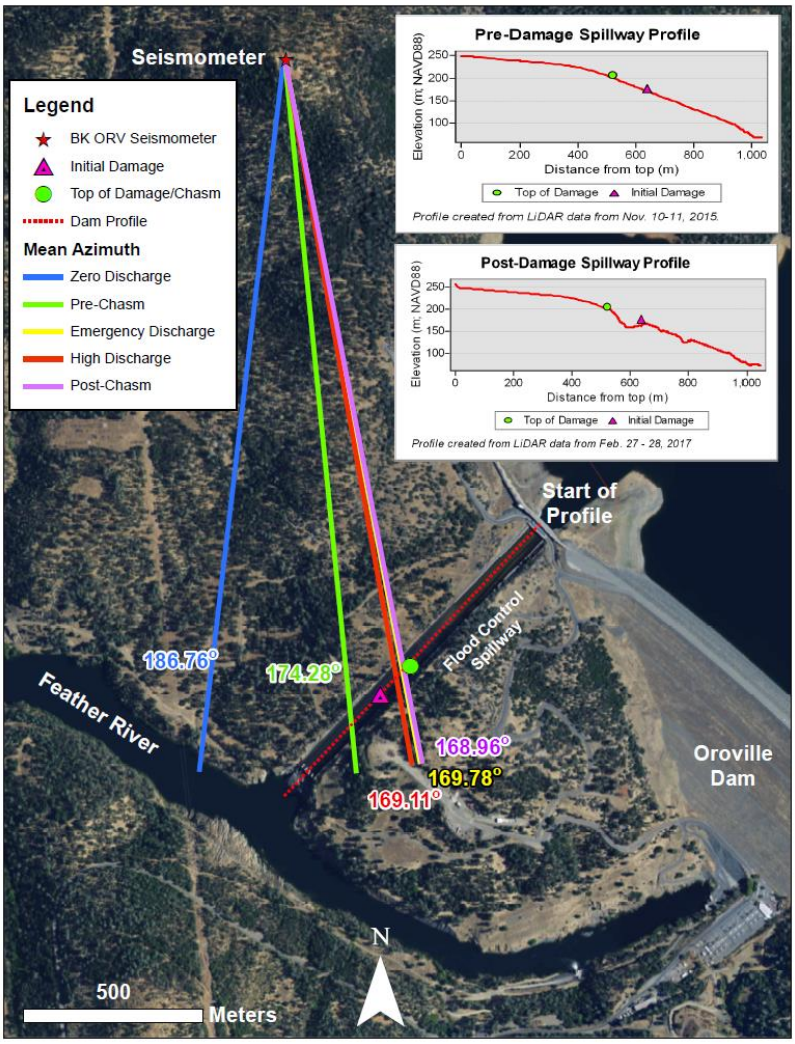

Figure 12: Mean azimuths for the five time intervals of interest mapped onto aerial imagery reveal the Emergency Discharge, High Discharge, and Post-Chasm mean azimuths point to the top of the spillway damage, where a steep drop creates a waterfall. The location of the initial damage, shown as a triangle, is estimated from photographs of the damage (see supplement). The location of the damage top, shown as a circle, is estimated from aerial photography and high-resolution LiDAR points collected after most of the damage occurred.

Conclusion

Our analysis of the seismic data collected during the Oroville Dam erosion crisis identified several techniques that are potentially useful for dam spillway monitoring and can be applied to fluvial studies. We evaluated the single-station FDPA method to locate the region of greatest flow turbulence. To our knowledge, this is the

first application of FDPA methods to analysis of a hydrodynamic signal. We were able to resolve changes in the mean azimuth of the turbulence-generated 5-10 Hz seismic waves under normal spillway conditions (2006 and 2011 release periods) when varying discharge and velocity generate changes in the location of the aeration zone inception point. During high spillway discharges and the onset of spillway damage (2017 crisis), the data analysis techniques were used to pinpoint the upstream location of spillway erosion as identified by the increased turbulence. This technique is promising for fluvial studies to identify potential seismic energy interference from nearby waterfalls (i.e. Roth et al. 2016) or in otherwise noisy study environments. The vertical-horizontal phase difference of the spillway-generated energy is consistent with a Rayleigh wave propagating up the dam non-uniform hillslope.

We find that for constant discharge conditions and varying amounts of spillway damage and associated macroturbulence, counter-clockwise hysteresis in the discharge-seismic power relationship indicates that the turbulent structures created by the spillway damage excite seismic energy more effectively. This observation is consistent with the increased energy dissipation by macroturbulent eddies and stepped flows considered in spillway design (Hunt and Kadavy, 2010a). This observation is also consistent with the fluvial geomorphology literature that argues a significant proportion of total energy dissipation is caused by macroturbulent eddies in natural rivers (Leopold et al., 1960; Bathurst, 1980; Prestegaard, 1983; Powell, 2014). Therefore, seismic monitoring may be a tool to quantify macroturbulent eddies and associated flow resistance in complex natural channels. The results of this study are consistent with those of Roth et al. (2017), who suggested changes in channel

morphology as a cause of water turbulence-associated hysteresis in natural channels. This study also implies that the Gimbert et al. (2014) model will under-predict seismic energy released in rivers with irregularly-shaped channels, waterfalls, and macroturbulent eddies. In this study, we observed that the generation of irregular channel morphology by damage to the spillway produced greater scaling exponents in the seismic power discharge relationship than the pre-damaged spillway, which produced scaling exponents similar to those predicted by the Gimbert et al. (2014) model.

Although results of this work can be applied to spillway monitoring and natural channel observations, we highlight several limitations of the methods used in this study. The long intervals of constant or known discharge in spillway operations are dissimilar from the sharp increases and decreases in discharge observed in most rivers hydrographs. In this study, we assumed that during intervals of constant discharge flow turbulence generated seismic motions with the same polarization attributes. Therefore, uncertainty was estimated by documenting the variability of polarization attributes during these time intervals of constant discharge. Due to the hazardous conditions surrounding the spillway channel, inferences on the mechanisms and degree of turbulence are limited to interpretations of aerial photography. This study was limited to the hourly resolution of reported discharge and the sampling frequency and sensitivity of the broadband seismometer in the study. For natural rivers, further research is needed to understand the appropriate time window length and sampling frequency to characterize turbulence at various scales.

Chapter 3: Instantaneous Polarization Analysis of Oroville Dam Spillway Erosion Crisis

The analysis in Chapter 2 showed that Frequency-Dependent Polarization Analysis (FDPA) is a suitable analytical technique for characterizing the dominant seismic source characteristics of a turbulent source. By interpreting the mean azimuth given by FDPA, the method identified the location of greatest energy dissipation. However, in many fluvial settings, the seismic energy will not have a single source, so techniques that can provide information on the distribution of fluvial-seismic energy might be beneficial. The analysis below is focused on presenting the distribution of IPA results and FDPA results to investigate if either of the methods are suitable to characterize the other sources of seismic energy besides the waterfall. The primary goals of this re-analysis are to determine if the methods are able to identify: 1) The signal from the "Emergency Discharge" period in which water flowed over the emergency spillway; 2) The evolution of the eroded chasm in the lower half of the spillway channel below the waterfall; and, 3) The position of the hydroelectric dam power plant, which was periodically active before and after the crisis event.

Instantaneous Polarization Analysis (IPA) Methodology

Extracting moment-by moment polarization attributes as described by Morozov and Smithson (1996) starts with constructing an analytic representation of the three-component real-valued signal $\vec{u}(t)$. This involves introducing an imaginary component equal to the Hilbert Transform of $\vec{u}(t)$. The result is a vector complex-valued function of time, $\vec{u}^c(t)$, which can also be represented in the Euler form:

$$\vec{u}^c(t) = \vec{u}(t) + iH\big(\vec{u}(t)\big) = \vec{A}^c(t)e^{i\varphi(t)},$$

where the real-valued scalar function $\varphi(t)$ is the instantaneous phase, and the complex-valued vector function $\vec{A}^c(t)$ contains all information about the amplitude, polarization, and phase-shifts between components of the signal. In this representation, the time-variation of the polarization and amplitude is separated from the comparatively more rapid time-variation of the phase of the signal. Physically, three-component particle motion can be fully represented as relatively rapid motion – specified by $\varphi(t)$ – along an elliptical orbit, whose semimajor $\vec{a}(t)$ and semiminor axes $\vec{b}(t)$ can change in length and orientation with time, but always remain orthogonal (Figure 13) .The real-valued vectors $\vec{a}(t)$ and $\vec{b}(t)$ can be computed at each time instant as

$$\vec{a}(t) = Re\left[e^{-i\psi_0}\vec{u}^c(t)\right] \tag{12}$$

And

$$\vec{b}(t) = Re\left[e^{-i(\psi_0+\pi/2)}\vec{u}^c(t)\right] \tag{13}$$

by finding the phase angle ψ_0 that maximizes the damped quadratic form:

$$\Phi(\psi) = \sum_{k=x,y,z}\left[Re[e^{-i\psi}u_k^c(t)]\right]^2 + \varepsilon\left(\sum_{k=x,y,z} Re\left[e^{-i\psi}u_k^c(t)\right]\right)^2, \tag{14}$$

where, ε is a small damping parameter. Then, we extract the polarization attributes as:

Amplitude: $A(t) = |\vec{a}(t)| = \sqrt{\vec{a}^*(t)\vec{a}(t)}$ (15)

Ellipticity: $\sigma(t) = {|\vec{b}(t)|}/{|\vec{a}(t)|}$ (16)

Strike of semimajor axis: $\alpha(t) = \arctan\left(\frac{\vec{a}_x(t)}{\vec{a}_y(t)}\right)$ (17)

Dip of semimajor axis: $\beta(t) = arctan(\frac{\overline{-\vec{a}_z(t)}}{\sqrt{\vec{a}_x(t)^2 + \vec{a}_y(t)^2}})$ (18)

Horizontal-vertical phase difference: $\phi_{hz} = arg\left(e^{i\varphi(t)}[u_x^c(t) + u_y^c(t)]\right) - arg\left(e^{i\varphi(t)}u_z^c(t)\right)$ (19)

Horizontal-horizontal phase difference: $\phi_{xy} = arg\left(e^{i\varphi(t)}u_x^c(t)\right) - arg\left(e^{i\varphi(t)}u_y^c(t)\right)$ (20)

The ellipticity is unity when the particle motion ellipsoid is perfectly circular and naught when perfectly linear. Since values of the phase φ are always determined with an uncertainty of π, there is $\pm$180° uncertainty in strike, $\pm$90° uncertainty in dip.

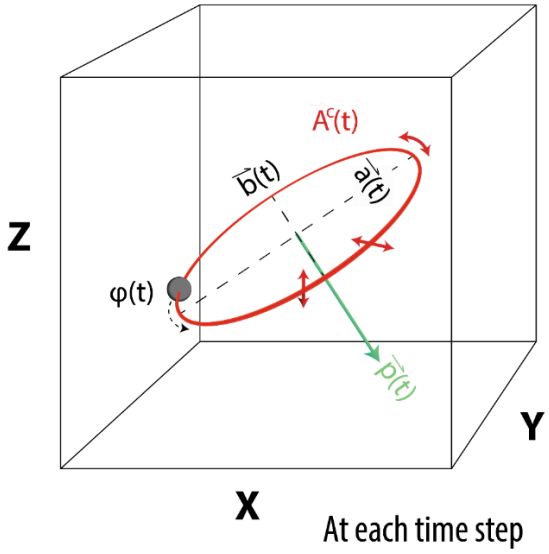

Figure 13: Illustration of the representation of a three component signal as an ellipse whose semimajor and semiminor axes vary moment-by-moment orbited by a fast-varying phase.

The polarization vectors $\vec{a}(t)$ and $\vec{b}(t)$ define a plane within the polarization ellipsoid, therefore, when the particle motion is elliptical but with a larger horizontal amplitude than vertical amplitude, it will appear as if the motion is horizontally

polarized. To overcome this uncertainty in orientation, we define a polarization vector $\overrightarrow{p}(t)$ which is perpendicular to the ellipse and equal to the cross product of $\vec{a}(t)$ and $\vec{b}(t)$. We redefine the strike and dip of the polarization vector as $\alpha_p(t)$ and $\beta_p(t)$ as above in terms of $\vec{p}(t)$, which are reliable when the particle motion is elliptical.

In order to apply the instantaneous polarization to a particular frequency band, the signal must first be filtered. In this study, a 4th-order Butterworth zero-phase filter over a set frequency band is applied to $\vec{u}(t)$ prior to instantaneous analysis.

Morozov and Smithson (1996) also describe an instantaneous directional filter as a way to selectively view the portion of the signal arriving from a specified direction. In this method, the complex three-component signal $\vec{u}^c(t)$ is first projected onto the major axis of the polarization ellipse $\vec{a}(t)$ (at each moment). Because the magnitude of the major axis varies, the major axis is first normalized so that:

$$\vec{u}_a^c(t) = \vec{u}^c(t) \cdot a_n = \vec{u}^c(t) \cdot \frac{\vec{a}(t)}{\sqrt{|\vec{a}(t)|^2}} \tag{21}$$

The projected complex three-component signal is then projected onto the specified direction of interest, a unit vector $\vec{d}$:

$$\vec{u}_d(t) = \vec{d} \cdot \vec{u}_a^c(t) \tag{22}$$

The resulting signal has the original units, but the values represent only the portion of the signal whose instantaneous major axis is aligned with the specified direction.

Instantaneous polarization results are determined as a function of time at the same sampling rate as the input seismic data, which is a much higher time resolution than the available river discharge and other flow characteristics for comparison at the

Oroville site. Therefore, the instantaneous polarization results in this study are accumulated into histograms for time windows of fixed length that correspond to the hydraulic data availability. For the Oroville Dam dataset, the selected time window is 1 hour. The underlying assumption of this approach is that the seismic signal is constant throughout the time window. Transient signals such as passing planes, thunder, or earthquakes are assumed to be suppressed by the large number of samples within the time window. It is expected that contributions from multiple seismic sources may result in multimodal distributions of attribute histograms.

Synthetic Comparison between FDPA and IPA

A simple synthetic illustration can illustrate the difference between the FDPA method used in Chapter 2 and IPA. In this simulation, two Rayleigh waves with random noise added in are simulated as arriving from 250^o and 120^o azimuth. The relative amplitude of the two waves is varied from zero (only Rayleigh wave from 250 ^{o}) to 100 percent (only Rayleigh wave from 120^o). The mean azimuth returned by the FDPA method represents the azimuth of the wave whose amplitude is greatest (Figure 14a). The mean IPA azimuth represents a weighted average of the two wave directions. To further illustrate the difference between the two methods, the distribution of the two directional attributes is shown in Figure 14b for 40% of the second Rayleigh wave. The distribution of the strike of the polarization vector provided by IPA is bimodal between the two sources and is able to simultaneously identify both sources. The distribution of the FDPA Θ_H values is unimodal and primarily points to the first Rayleigh wave. The information provided by the IPA method in this scenario has the potential to be more useful than FDPA for fluvial-

seismic studies with varying source contributions along a fluvial source (e.g. Burtin et al., 2010).

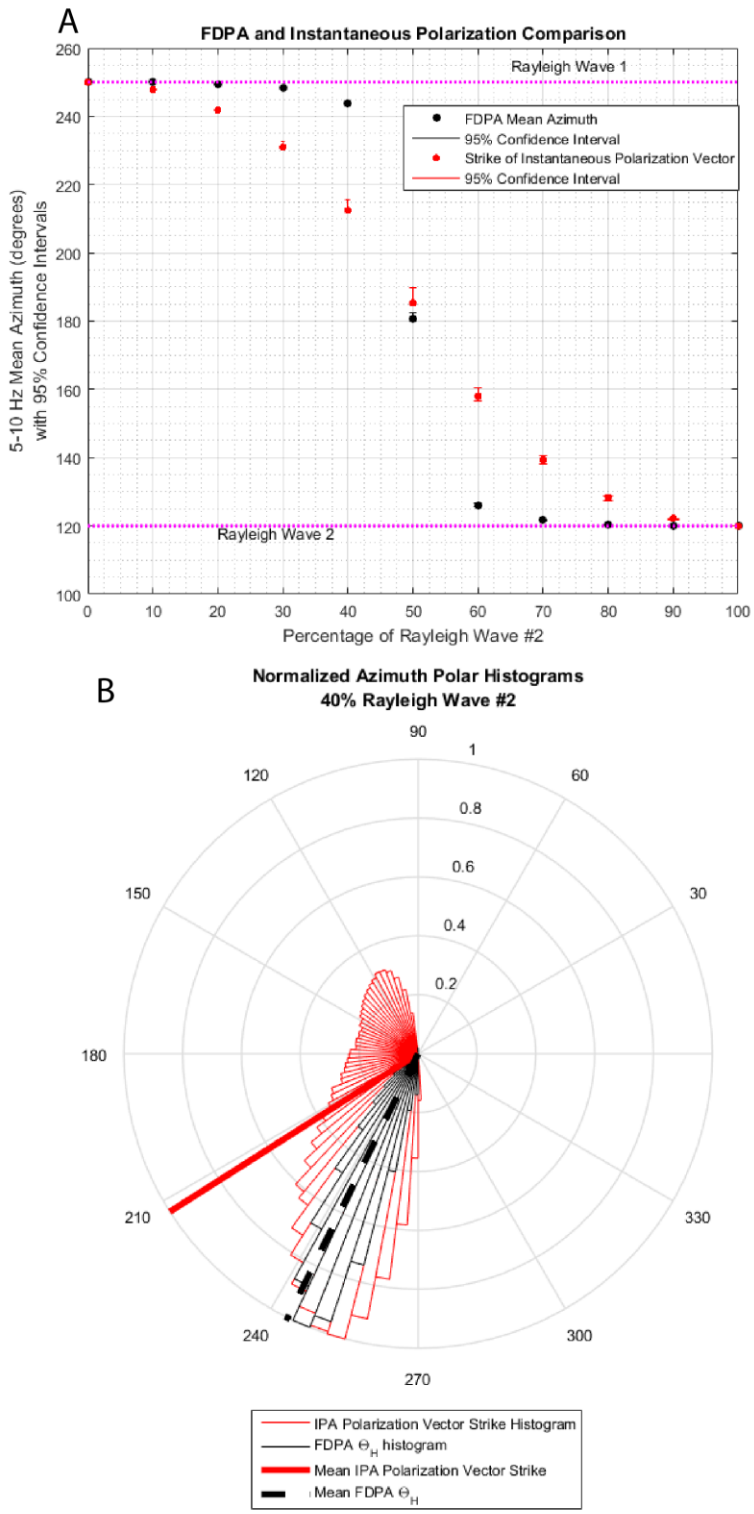

Figure 14: The mean directional attributes returned by IPA and FDPA describing two synthetic Rayleigh waves arriving from different directions are shown in 14a for varying amplitudes of Rayleigh wave 2. In 14b, the distribution of these directional attributes are shown for an azimuth of Rayleigh wave number 2 that is 40% of Rayleigh wave 1.

Oroville Dam Crisis IPA Results

The IPA results in the 5-10 Hz frequency band for the 2017 study period are presented in Figure 15. This frequency band was selected because it was identified in Chapter 2 as the frequency band in which the polarization attributes are most sensitive to variations in spillway discharge. The IPA results are presented as a time series of the hourly histograms throughout the 2017 study period. In each hour, the histograms are normalized so that the attributes sum to one. As a comparison, the same 2006 and 2011 time release periods evaluated in Chapter 2 were also evaluated using IPA. The figures displaying these results are shown in Appendix B. The results during these periods are consistent with the pre-crisis 2017 period, so 2006 and 2011 time periods are not discussed separately.

In Figure 15a, the average amplitude of the polarization vector shows a strong relationship with spillway discharge above a spillway discharge of about 500 m^3/s and does not show any hysteresis with discharge. This is consistent with the results in Chapter 2, in which hysteresis in the relationship between discharge and seismic amplitude was only observed at lower frequencies (0.5-1 Hz).

The instantaneous polarization vector strike of the 5-10 Hz seismic signal presented in Figure 15b compares favorably with FDPA Θ_H results presented in Chapter 2. During periods with high spillway discharge, the distribution of the polarization attributes narrows, indicating the results are sensitive to the spillway activity. The distribution of strikes determined using the polarization vector is unimodal, while the distribution strike of the major axis is bimodal (Figure 15c), due to flipping. The strike of the polarization vector points to approximately 175° during

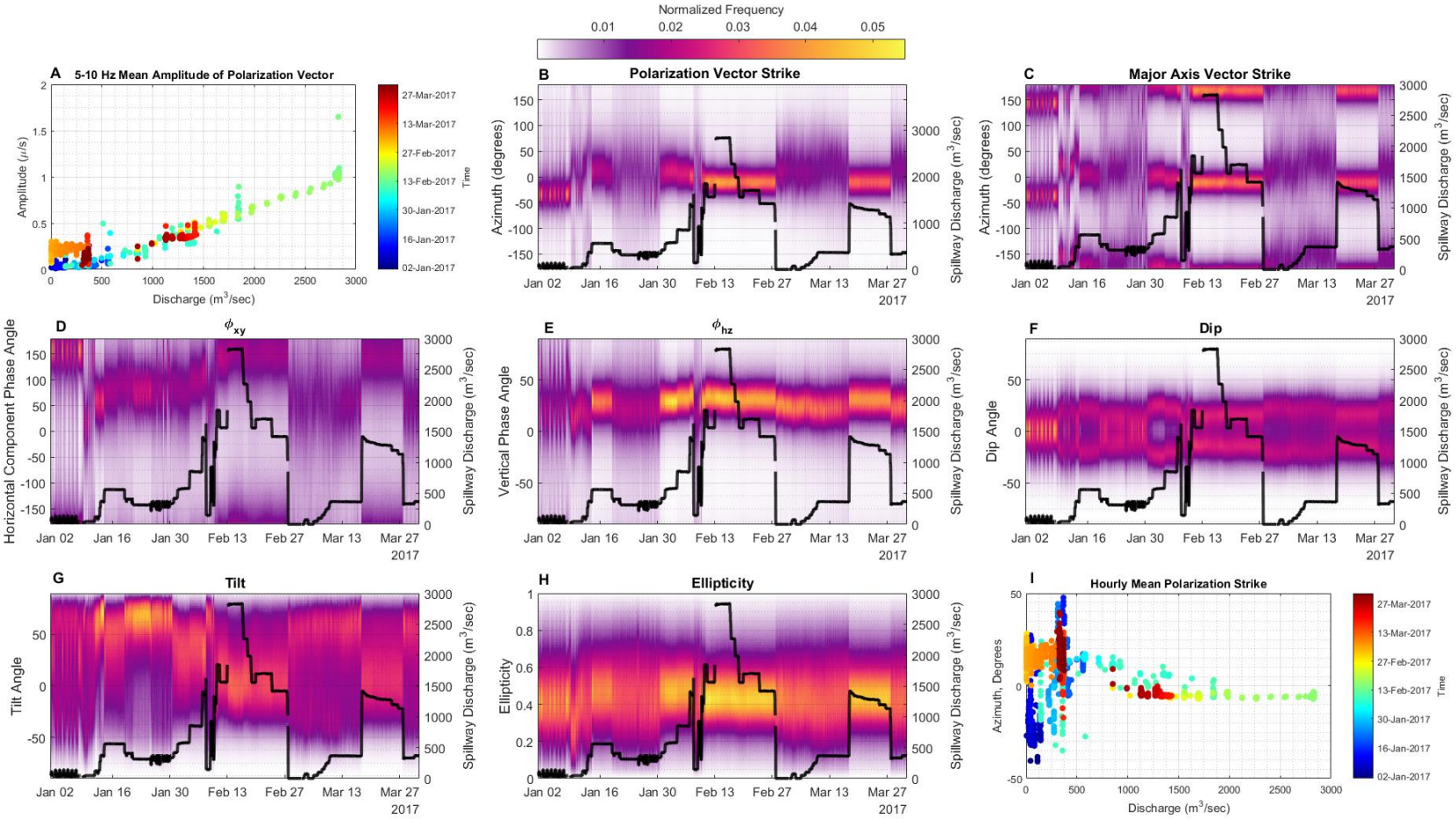

Figure 15: IPA attributes for the 2017 Oroville Dam Crisis period discussed in Chapter 2. Figures B-H are presented as hourly histograms of the IPA attributes, normalized so that in each hour, the frequencies sum to one. On these figures, the spillway discharge is shown as a dark line. Gaps exist in the discharge record.

the high discharge periods. During low discharge periods, the distribution is much broader. There is a hysteresis in the relationship between mean hourly polarization vector strike and spillway discharge (Figure 15i), similar to the hysteresis in FDPA mean azimuth described in Chapter 2.

The phase difference between horizontal components is close to -180° and 180° during the periods of highest discharge, indicating linear horizontal particle motion consistent with the passing of a Rayleigh wave (Figure 15d). Before the crisis event in early February, the horizontal phase difference has a weak relationship with discharge, excluding the early January period of hydroelectric power generation (discussed later). The vertical-horizontal phase difference (Figure 15e) consistently deviates from an expected value for a Rayleigh wave of +/- 90°. This is consistent with observations reported in Chapter 2. SPECFEM2D modeling shows that the hillside topography between the spillway and the BK ORV seismometer is a feasible reason for the deviation from +-90°. This deviation appears to be present even when the spillway discharge is very low or zero, indicating that ambient noise traveling to the station even from non-spillway sources may be affected by the hillslope topography.

The dip angle represents the angle of the major axis below the horizontal plane. The results shown in Figure 15f that the dip angle is bimodal, corresponding to the flipping of the major axis strike. Dip angles during the highest discharge are about 15° below the horizontal. The slope of the hillside between the seismometer and the spillway is approximately 13°, so this may represent the travel of the Rayleigh wave up the hillslope. The incidence angle of the wave as estimated by FDPA was not consistent in the 5-10 Hz frequency band. The tilt angle (Figure 15g) refers to the angle

of the polarization vector below the horizontal plane. The tilt is highly variable and broadly distributed. The ellipticity (Figure 15h) of the instantaneous polarization ellipse is typically between 0.3 and 0.7, indicating the deviations from the perfectly circular motion anticipated for a pure Rayleigh wave.

The 5-10 Hz instantaneous polarization result histograms, presented in hourly bins, provide information on how the polarization of the signal changes throughout the Oroville Dam erosion crisis. The results also provide information on the changing non-spillway seismic signal before and after the crisis. In January 2017, hydroelectric power generation activities appear to be detected by the seismometer, with the distribution of polarization vector strikes narrowed and pointing to the dam, where hydroelectric power is generated by releasing water through turbines. The dip of the major axis and the horizontal phase angle are both narrowly distributed, with the dip angle near zero and the horizontal phase angle near 180°. In late February and early March, the spillway discharge drops to zero, and at this time the hydroelectric power plant was closed due to blockage from the crisis debris. The hydroelectric power plant was unable to function from February 13th until March 4th, when it began to operate at a highly reduced capacity. The polarization attributes in late February are more broadly distributed and has a dip near 20° and a more circular horizontal phase angle. The source of this energy could be the Feather River. During the time period when the emergency spillway was active (directly before and during the initial maximum spillway discharge), no change is observed in the instantaneous polarization attributes, indicating that the method is unable to resolve the emergency spillway operation.

The polarization attribute of greatest interest to fluvial –seismic researchers for discerning between seismic sources is the one indicating the source direction of the signal. In Chapter 2, the hourly mean FDPA azimuths were discussed. To evaluate the differences between the FDPA and IPA methods, a comparison of the hourly means during the 2017 study period is presented in Figure 16**.** At low discharge, there is the greatest differences between the FDPA and IPA, signaling that the two methods characterize the motion of a weakly-polarized signal in different ways. This is to be expected, as one method involves eigenanalysis and the other does not. At high discharge, the two methods both return consistent mean azimuthal values, although there is an offset of approximately 5° between the two means. This is likely due to a difference in the distribution of azimuth values as demonstrated in the earlier synthetic example.

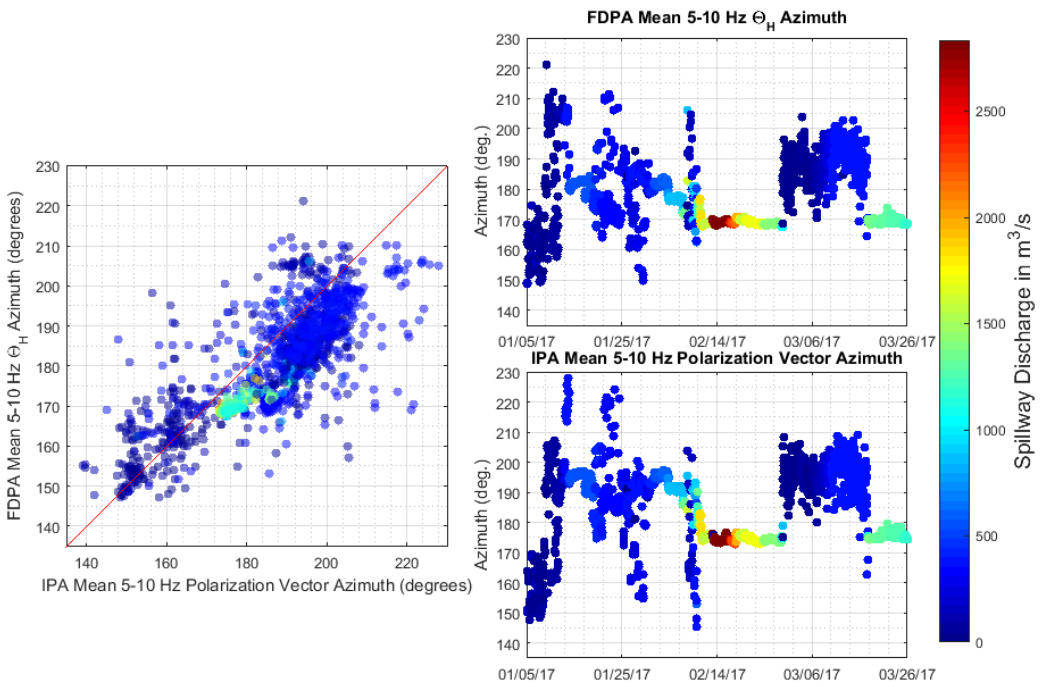

Figure 16: Left- The mean azimuth returned by IPA and FDPA fall generally along the red 1:1 line, with greater scatter at low discharge (blue colors). However, even at high discharge, there is a discrepancy of approximately 5 degrees. Right- At high discharge, both methods return a consistent mean azimuth.

In order to compare the distributions of the FDPA and IPA directional results, the strike of the polarization vector, the instantaneous directional filter results, and hourly histograms of the 5-10 Hz FDPA results are presented in Figure 17. The FDPA results were not presented this way in Chapter 2. The results show that the FDPA results in the 5-10 Hz band are more narrowly distributed than are the instantaneous results. The instantaneous directional filter results are the most broadly distributed in azimuth, although the results show the variations in the amplitude of the seismic signal that are less apparent in the histograms of azimuthal results.

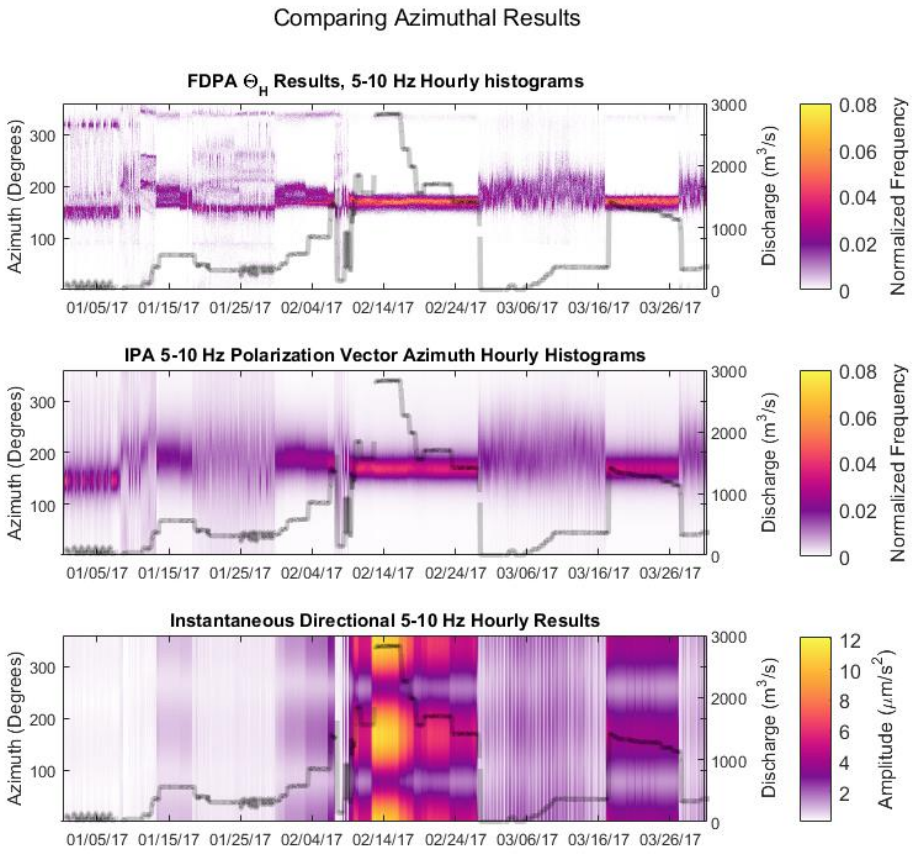

Figure 17: Top- Hourly 5-10 Hz FDPA azimuth histograms resolve multiple sources during in January and February, which are not apparent in the 5-10 Hz IPA results (Middle). The Directional Filter Results (Bottom) has the broadest azimuthal results and contains a 180º uncertainty, but has the advantage of being in units of seismic amplitude. In all three figures, the spillway discharge is shown as a black line.

Discussion

Contrary to the simple synthetic example shown earlier in this chapter, the FDPA hourly histograms of azimuth results appears best able to identify the distribution of energy dissipation. Both the IPA and FDPA methods are able to identify the hydroelectric turbines beneath the Oroville Dam as a source in early January. However, only FDPA results are able to discern additional sources during mid-January. The FDPA method may also be more effective at identifying the hydroelectric turbines because it may produce seismic energy at a different frequency within the 5-10 Hz

frequency band than the flood control spillway. The IPA has lower azimuthal resolution than the FDPA method, which is attributed to the eigenanalysis within the FDPA method, which is effective at minimizing the effect of background noise.

Using the distribution of hourly azimuth estimates rather than the mean azimuth is more effective because of the non-uniform temporal distribution of azimuth estimates. For the 5-10 Hz band, in which the Oroville data is sufficiently polarized, this is an effective method. This work implies that fluvial-seismic locations should be determined with the distribution of FDPA results rather than IPA results for a strongly polarized signal. At the Oroville Dam, the histogram of azimuthal results may be used to identify portions of the flood control spillway that are contributing greatest to the observed seismic signal. The use of the histograms represents a much greater directional resolution than presented in Chapter 2. Figure 18 below shows the normalized histogram of FDPA Θ_H results along with the spillway channel geometry for a time interval after the crisis occurred, in 1 degree azimuthal bins. The observed energy is distributed along the base of the spillway channel, where a large chasm was eroded. The mean azimuth, which was analyzed in Chapter 2, is presented as a red line in the figure. As the distribution of Hourly Θ_H results is skewed towards the base of the channel, the mean predicts the position of the greatest seismic energy generation is further up the channel than is visible looking at the distribution of Θ_H results.

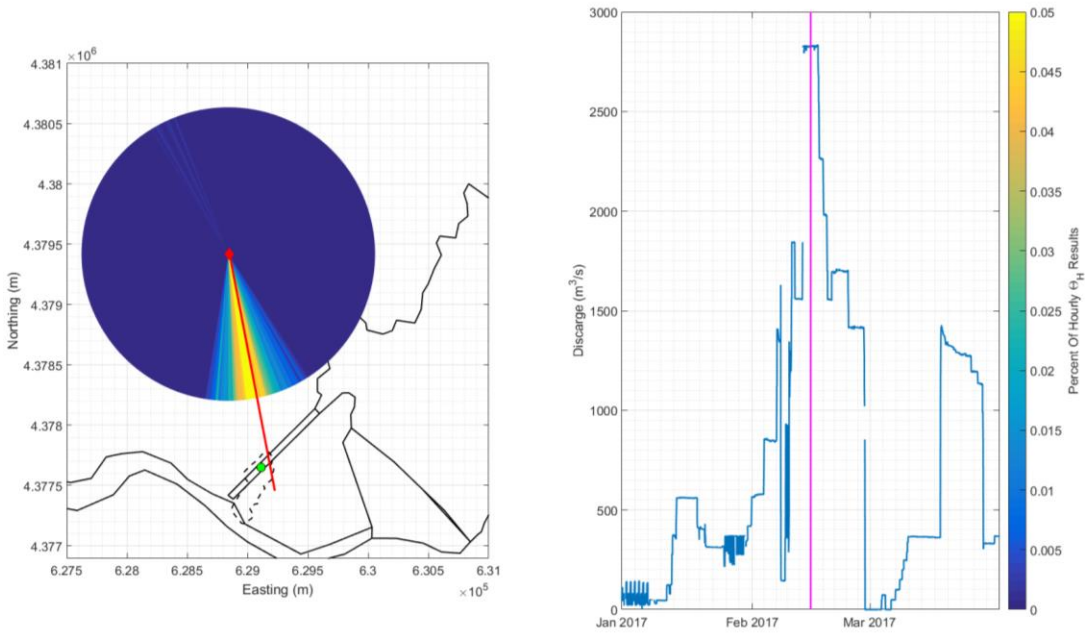

Figure 18: Left) The normalized FDPA azimuth results are shown as a polar histogram centered on the BK ORV seismometer (shown as a red diamond) for a single hour during maximum discharge. The outline of the Oroville Reservoir, flood control spillway, and Feather River are shown in black. The green dot shows the location of the initial damage to the spillway and the dashed black line shows the extent of the spillway damage determined from aerial photography. The red line shows the mean azimuth. Right) The spillway discharge reported during the 2017 time interval, with the vertical pink line showing the hour presented in the left panel.

Chapter 4: Seismic and Hydraulic Monitoring of Storm Events, Northwest Branch Anacostia River, MD

Introduction

Turbulently flowing water expends energy to transport bed material and form a three-dimensional natural river channel morphology. As there is a complex feedback between the channel morphology, bed material, and turbulent energy expenditure, natural rivers channels in equilibrium are described as self-formed. Early seminal studies investigating stable channel morphologies focused on channel shape formed by the bankfull stage, which is identified as performing the most geomorphic work. One hypothesis put forward about the distribution of energy dissipation at bankfull stage is that a river with a mobile bed will adjust to minimize the along-channel variance of the depth, slope, and velocity at bankfull stage (Langbein and Leopold, 1966). One potential cost of this minimization is that at lower stage there is increased variability in shear stress among riffles, pools, and portions of meanders.

The riffle-pool sequences in gravel-bed rivers are commonly-observed features, suggesting their importance in channel maintenance though the mechanism behind their formation and maintenance remains an area of active research. The mechanism is related to the minimum variance hypothesis, though it is more explicitly stated as a hypothesized "velocity reversal" or "shear stress reversal" (Wilkinson et al., 2004). In this hypothesis, at low flow greater shear stress (or velocity) is observed in the steeper riffles, while at high flow the deeper pools contain greater shear stress (or velocity). In this model, with increasing discharge sediment is first moved from the riffles into the pools, then scoured out of the pools to maintain to the channel morphology. To

maintain continuity, riffles are shallower and wider while pools are deeper and narrower. At this time, numerical and field studies have not conclusively confirmed or rejected the hypothesis. Difficulties in observing the shear stress at many points along a river profile during dynamic flood events may limit the number of studies evaluating dynamic energy expenditure.

Short-lived flashy storm events in urbanized watersheds are particularly challenging to study, though understanding energy dissipation during these events may enhance channel restoration design. With increasing impervious surface area in the watershed, generally an increase in total runoff leads to high peak stormflow. A consequence of the discharge peaks is scoured and incised banks and increased sediment yields. In an effort to preserve river ecosystem functions and minimize downstream sedimentation, there is considerable interest in channel restoration design for small to mid-size urbanized streams. While channel and bank modifications may have design goals ranging from creating fish habitat to protecting along-stream infrastructure, for these features to be long-lived they should incorporate natural river function to the extent possible. Understanding fluvial energy dissipation in urbanized streams therefore has direct practical implications, though due to the short-lived and intense nature of urban stream hydrographs make evaluating this a technical challenge.

Fluvial seismology, the observation of small seismic waves to infer in-channel dynamics, has the potential to characterize dissipative energy losses in short-lived and intense urban stream floods. Early studies in fluvial seismology focused on large rivers that excite larger amplitude seismic waves. Relatively fewer studies have focused on smaller streams, though these studies have reported success in identifying the river-

excited signals. Some studies have reported storm hydrograph results (Roth et al. 2016; Barriere et al., 2015; Burtin et al., 2011), while others have reported snowmelt and/or controlled flood releases (Anthony et al., 2018). In these studies, seismometers are typically placed within 5-10 meters of the channel, a distance necessitated by the low seismic signal/noise ratio for small streams. This short distance may lead the seismic observations to reflect a local portion of the stream rather than provide channel-integrated information. Local stream observations may be beneficial if the goal is to evaluate along-stream variability in fluvial energy dissipation, though it may limit interpretation in the context of broader stream mechanics if localized features tend to dominate.

In this study, a reach in an urbanized stream with short-lived hydrographs was selected for hydraulic and seismic observation. Hydraulic observation consisted of evaluating the discharge, basal shear stress, stream power, and ratio of mean velocity to shear velocity (U/U*). Most previous fluvial-seismic studies have compared seismic results to the discharge, though this may make comparisons among studies difficult since the river slope is not taken into account. The basal shear stress is a more direct evaluation of the fluctuating forces at the base of the channel, and some authors have discussed power variations in terms of shear stress (Burtin et al., 2011; Gimbert et al., 2014). Stream power is also a physical unit of energy expenditure. Some authors have suggested fluvial-seismic energy should be linearly related to stream power (Roth et al., 2016). The U/U* ratio is a unitless measure of hydraulic roughness (flow resistance) that is used to compare the turbulent energy expenditure among fluvial systems (Powell, 2014). The primary objective was to characterize the along-stream variability

of these metrics of energy dissipation and determine if seismic observations at the river reach scale were able to resolve this variability.

Methods

Study Area Description

The site selected for this study is a straight, incised reach of the Northwest Branch of the Anacostia River, which is contained in a suburbanized watershed north of Washington, DC (See Figure 19). The river crosses the Atlantic Fall Line knickzone and the geological boundary between crystalline Piedmont bedrock and poorly consolidated Coastal Plain sediments before joining the Northeast Branch of the Anacostia near the tidal limit. The selected reach is a 100-meter long boulder and cobble bedded stream reach located downstream of the steep Fall Line knickzone. The bed sediment is a thin veneer over bedrock. It also has, steep banks, due to channel incision, which is a result upstream the Fall Line knickzone above the Piedmont-Coastal Plain boundary. A consequence of this incision is that many floods remain within the channel, providing a wide range of in-channel flows and correspondingly high values of flow velocities and turbulent intensities. The suburban development in upstream watershed areas generates rapid response from impervious surfaces; this runoff is conveyed by storm sewers to the heads of short tributaries that line the incised portion of the stream. This interaction between urban hydrology and watershed geomorphology results in two hydrograph responses to precipitation events: an initial tributary response as overland flow runoff is conveyed to the short, steep tributaries and a delayed response generated by the movement of the flood wave down the main

channel. The time separation between these two responses is dependent on the precipitation intensity and spatial distribution of precipitation in the watershed.

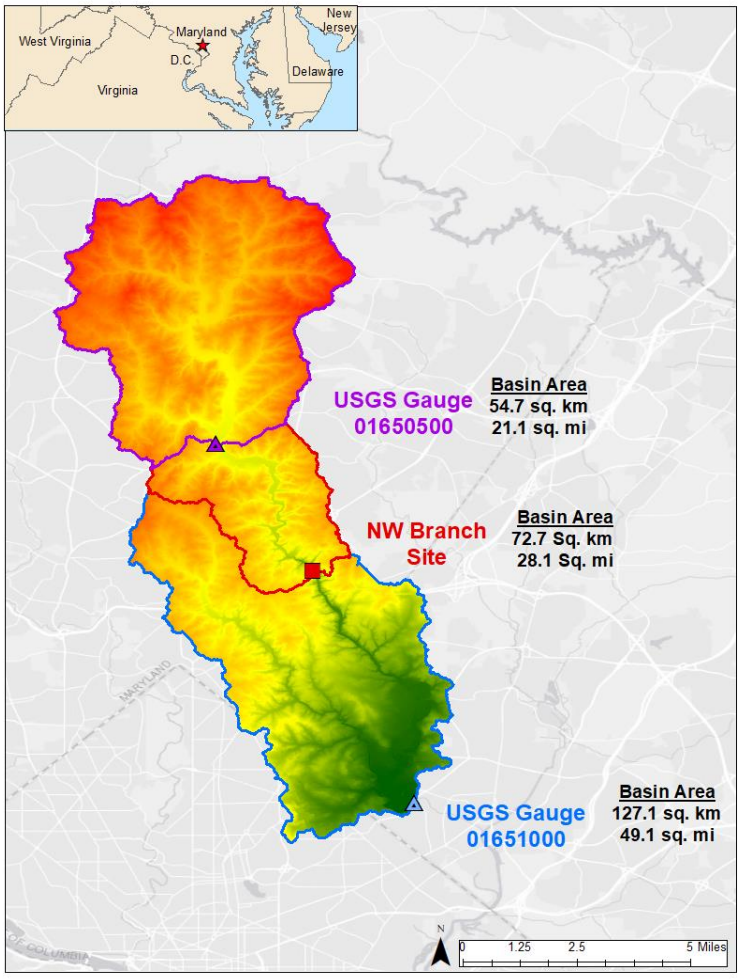

Figure 19: The Northwest Branch study reach is between two USGS gauges and located in Montgomery County, Maryland. The upstream gauge (1650500) is in Colesville, MD and the downstream gauge (1651000) is in Hyattsville, MD.

Discharge at the Study Reach

The study reach is bounded by two USGS stream gauges which report the discharge of the Northwest Branch at 15 minute intervals, providing a constraint on the discharge through the study reach. The instantaneous annual flood peak recurrence interval was calculated for both the upstream and downstream USGS gauges, using 79

and 78 years of data, respectively. The downstream and upstream USGS gauges have a similar basin area-normalized discharge below the 10 year storm (Figure 20). Therefore, for storms smaller than the 10 year storm, normalizing the discharge by basin area is appropriate. The largest storm during the study period is the approximately 8.5-10 year storm (instantaneous peak normalized discharge recorded as 13.2 m^3/km^2).

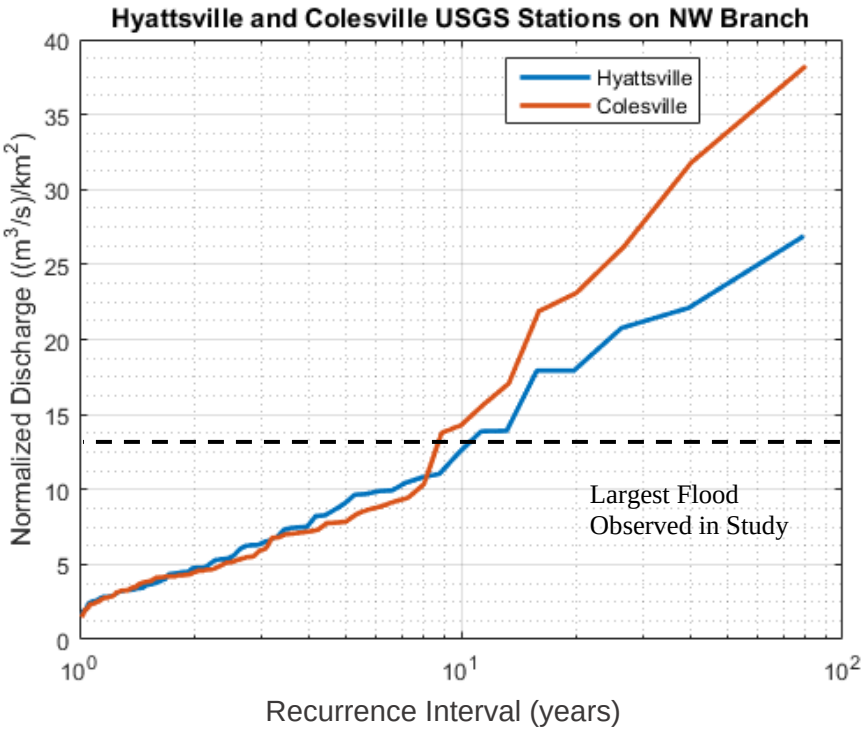

Figure 20: The USGS gauges upstream and downstream of the research site have similar basin-normalized discharges instantaneous peak discharges that occur on average more frequently than 10 years. This supports the use of basin area normalization to estimate discharge at the study reach on Northwest Branch.

To establish a record of continuous discharge (and water surface elevation, discussed later) at the research site, U20L HOBO® pressure transducers pressure transducers were affixed to metal posts driven into the stream bed. The pressure transducers sample the pressure every five minutes, which is corrected to a water depth using the hydrostatic pressure. A single barometric pressure transducer deployed at the site is used to correct for barometric pressure variations using proprietary HOBOware®

software. The in-stream sensors record temperature, allowing an account for variations in fluid density with temperature. Water depth accuracy listed by the manufacturer is 0.4 cm of water depth. The top of each pressure transducer's metal stake was surveyed. Using simultaneous water depth readings and water surface elevation measurements, a continuous record of water surface elevation is created by applying a correction value each time the pressure transducer was re-deployed.

The discharge at the study reach is calculated by establishing a rating curve between the water surface elevation at the study reach and the upstream USGS gauge station near Colesville, MD. Its response to storm hydrographs was similar to the stage response at the study reach, except for an initial tributary response at the study reach. When this tributary response is removed and a 30-minute time lag between the two signals (as determined by cross correlation) is applied, a polynomial function is fit to the stage-discharge relationship to establish a continual record of discharge at the study reach (see Fig. 21). The basin-area normalized discharge at the Colesville USGS station was multiplied by the watershed area of the study reach. The upstream pressure transducer used to create the rating curve was moved between the 2017 and 2018 study periods, so a rating curve was created for each of the different time periods using the same methodology.

Hydraulic and seismic monitoring was conducted during two separate study periods: July 28th – December 21st, 2017 and July 7th – August 15th, 2018. Thirteen storm events are identified in the 2017 time interval (shown in Fig. 22, top panel). The 2018 time period (Fig. 22, bottom panel) had elevated discharge above baseflow during a series of heavy rain events, so the 2018 period is not broken into discrete flood events.

Table 3 shows the flood events considered in this study, as well as identifying the seismic deployment number.

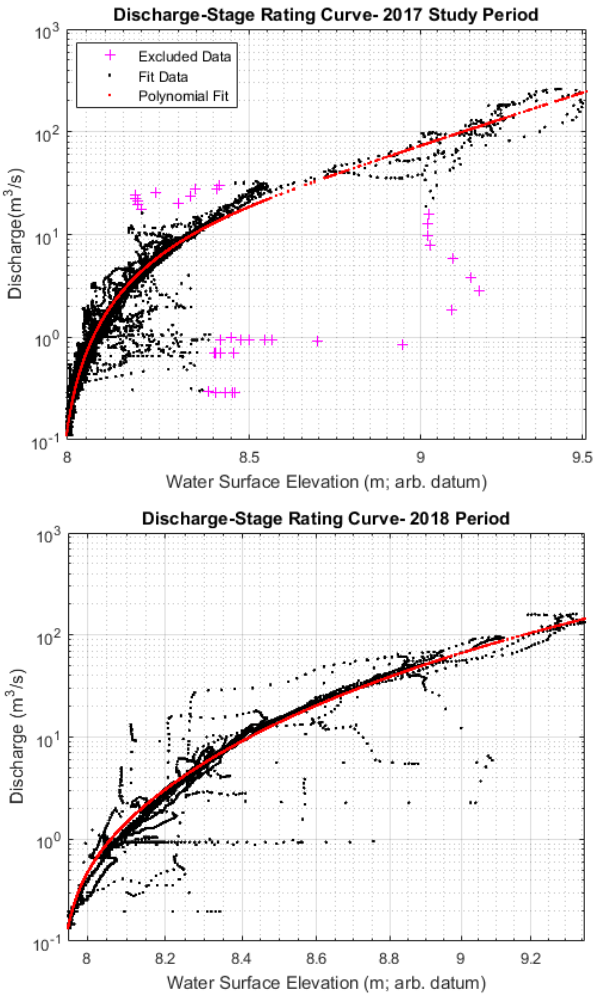

Figure 21: Rating curves used to calculate discharge at the study river reach. The rating curve is built on the relationship between water surface elevation at the upstream pressure transducer and discharge at the upstream USGS gauge. Basin area normalization and a time lag are applied. There is a local tributary response to storm events, which is excluded for the rating curve fit (purple markers).

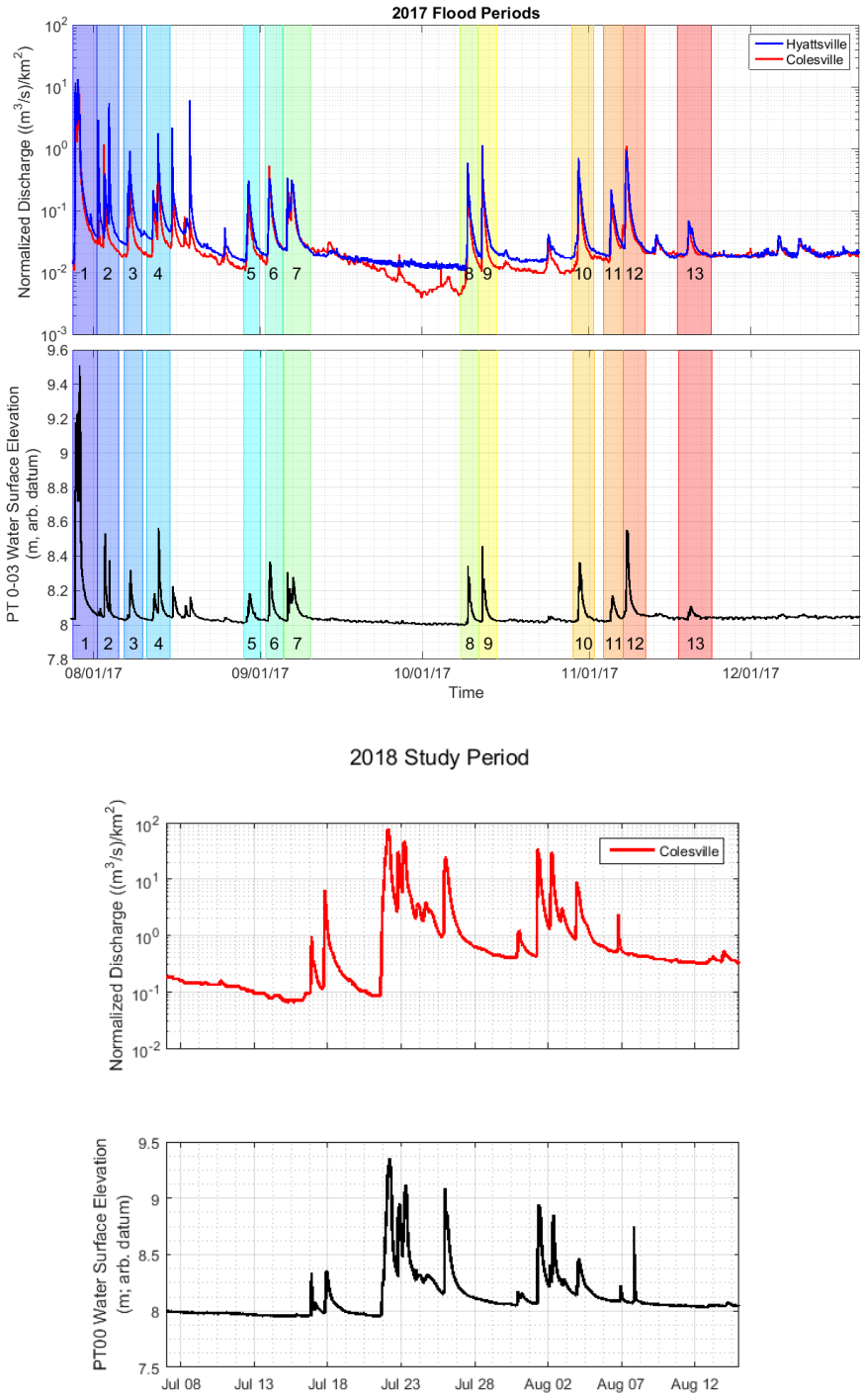

Figure 22: The 2017 (top panel) and 2018 (bottom panel) periods of discharge record at the Norwest Branch research site. The 2017 record is subset into 13 flood events, the 2018 period, which contains numerous overlapping flood hydrographs, is not.

Flood Number or Interval name	Start Time (UTC)	End Time (UTC)	Peak Discharge (cubic meters per second)	Node Deployment Number	Used In Scaling Analysis
1	7/28/2017 5:00	8/1/2017 16:00	95.43	1	Y
2	8/1/2017 16:00	8/5/2017 17:00	8.04	1	Y
3	8/6/2017 17:00	8/10/2017 2:00	3.47	1	Y
4	8/10/2017 22:30	8/15/2017 6:00	8.81	1	Y
5	8/28/2017 23:00	8/31/2017 20:00	1.51	2	Y
6	9/1/2017 22:00	9/5/2017 5:00	4.39	2	Y
7	9/5/2017 9:00	9/10/2017 9:00	3.28	2 and 3	Y
Control Period	9/20/2017 0:00	9/25/2017 0:00	0.15	3	
8	10/8/2017 3:00	10/11/2017 12:00	3.94	4	
9	10/11/2017 12:00	10/14/2017 21:00	6.22	4	
10	10/28/2017 22:00	11/1/2017 23:00	4.33	4	
11	11/3/2017 16:00	11/7/2017 8:00	1.34	4	
12	11/7/2017 8:00	11/11/2017 11:00	8.51	4	
13	11/17/2017 12:00	11/23/2017 17:00	0.72	5	
2018 Period	7/22/2018 14:00	8/17/2018 14:00	55.69	6	Y

Table 3: Flood periods used in the study, with seismometer deployment number.

Channel Morphology Measurements

Morphological measurements of the study reach included surveying ten channel cross-sections spaced 10 meters apart to a common arbitrary elevation datum. A survey level and rod were used to establish vertical control, while a leveled survey tape aligned perpendicularly to the channel established horizontal control. From this surveying effort on 7-12-2017, an elevation model was created for the study reach by interpolating between elevation points. A single elevation model is used in the following analysis, with the assumption that minimal channel bed rearrangement occurred over the one-year study period.

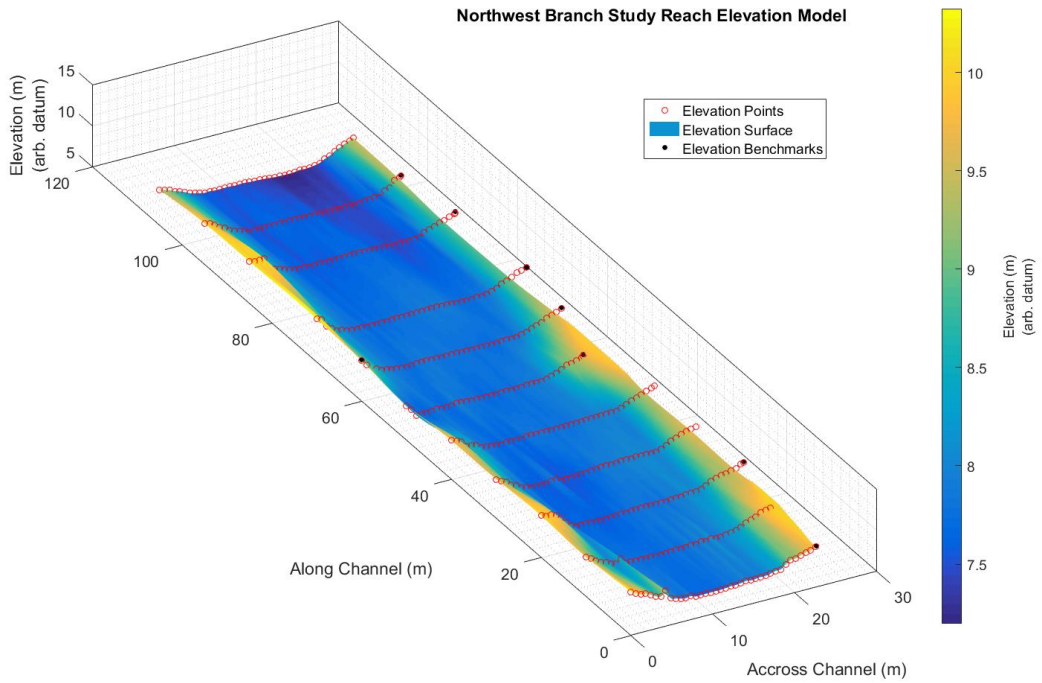

Figure 23: The elevation model created from the survey data for the river reach.

Grain Size Characterization

The grain size distribution at the field site was characterized by Wolman (1954) random-walk pebble counts. Pebble counts were conducted for more than 100 clasts at nine channel cross-sections spaced approximately 10 meters apart. The 84th percentile grain sizes (D_{84}), which are used as a measure of the grain roughness height, are shown in Figure 25. The complete grain size analysis results are shown in Appendix C. D_{84} values in the study reach ranged from 116 to 178 mm, which is cobble-sized. Boulders (> 256 mm) and bedrock outcrops are found along the banks, which contributes to the confinement of the channel.

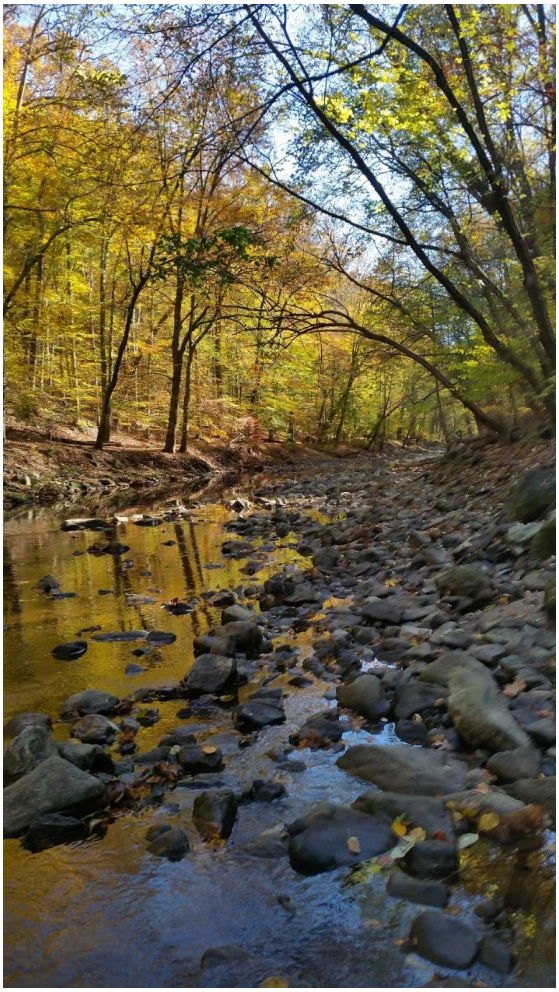

Figure 24: Image of the study reach taken at the most upstream portion of the study reach, looking downstream. Image taken October 2017.

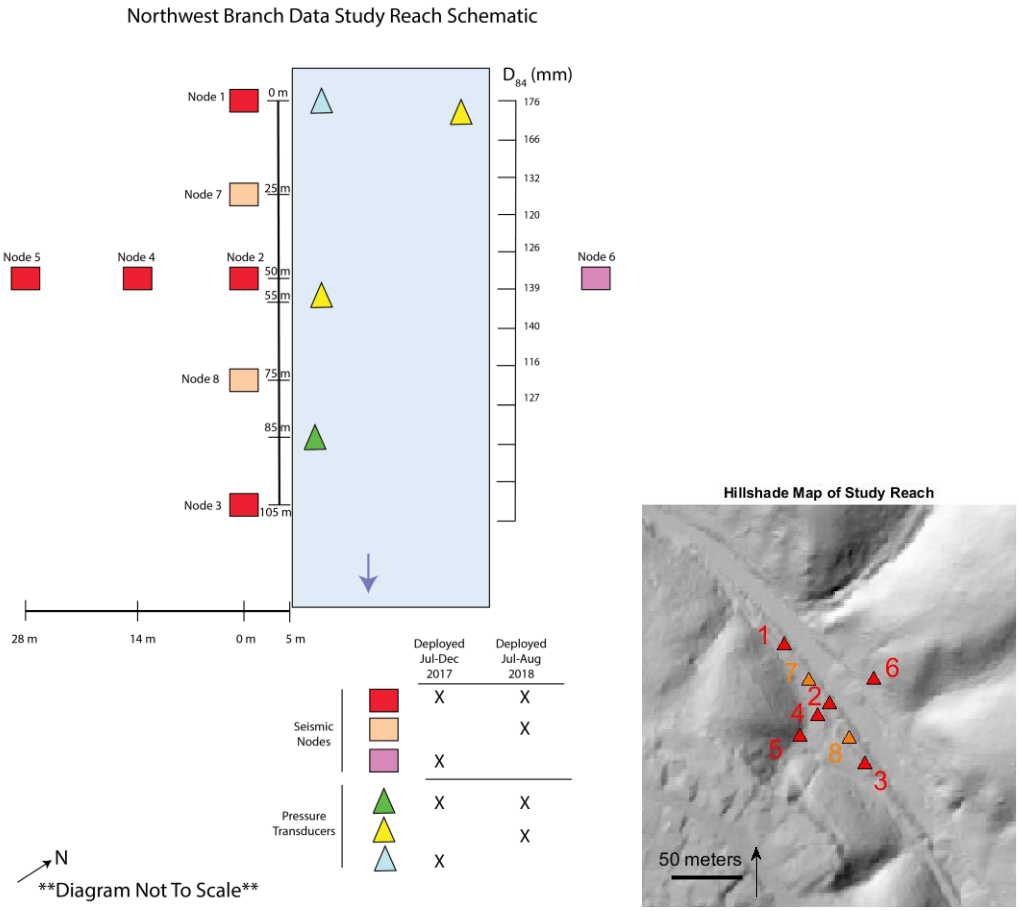

Figure 25: Diagram illustrating the data collected at the Northwest Branch research site in June through December, 2017. LiDAR data from Maryland's IMAP program was used to create a shaded relief map of the study reach, with the true location of the nodes used in the study.

Seismic and Hydraulic Instrumentation

Collecting simultaneous seismic, hydraulic, and atmospheric data is required to interpret the likely source of the seismic vibrations in this study. The data presented in this study was collected during two separate intervals with differing configurations. The first configuration consisted of six seismic nodes and two pressure transducers and took place from June 28th, 2017 to December 21st, 2017. After analyzing this dataset, it became apparent that an additional large-magnitude flood was needed to confirm the

fluvial and seismic results at high discharge. So additional data was collected from July 7th to August 18th, 2018. To examine variability in energy gradient and seismic observations in greater detail, three pressure transducers and seven seismic nodes were deployed.

Seismic data was collected from Fairfield Zland three-component seismic nodes, recording at 250 Hz sampling frequency. The nodes consist of three orthogonal geophones. The seismic nodes are deployed within 6" deep holes dug by a garden spade, leveling the node with a bubble level, and orienting them to true north. The nodes were placed in the T-shaped array shown in Figure 25, which is designed to characterize the along-channel and across-channel variability of seismic energy note that the configuration of these nodes was altered slightly between the 2017 and 2018 deployment of the nodes. The nodes are able to record data for approximately 30 days before replacement. In 2017, five separate deployments were conducted as shown in Table 3. In 2018, a single additional deployment was undertaken.

Calculating Metrics of Fluvial Energy Dissipation

Hydraulic variables were computed from this time series of discharge, the water surface elevations provided by the pressure transducers, and the survey data. Table 4 shows the hydraulic variables computed from this data. Each of the eleven cross sections will have a time series of shear stress, U/U*, and stream power.

Table 4: Metrics of Fluvial Energy Dissipation

Variable	Formula	Units
Water Surface Slope	$S = \frac{(E_a - E_b)}{d}$, where E_a and E_b are the elevations of the water surface at the upstream and downstream gauges, respectively, and d is the distance between them.	Unitless

Velocity Head	$V = U^2/2g$, where U is the cross-sectional mean velocity and g is the acceleration due to gravity	m
Energy Gradient	$S_e = \frac{(E_a+\overline{V_a})-(E_b+\overline{V_b})}{d}$, where E_a and E_b are the elevation of the water surface at the upstream and downstream gauges, respectively, and $\overline{V_a}$ and $\overline{V_b}$is mean velocity head at the two cross sections closest to the upstream and downstream gauges respectively and d is the distance between them.	Unitless
Cross Sectional Area of Flow	$A = \sum_{i=1}^{N} \frac{Water\ Elevation_i - Bed\ Elevation_i}{Channel\ Width_i}$ for all channel segments *i* where $Water\ Elevation > Bed\ Elevation$	m^2
Wetted Perimeter of Flow	$P = \sum_{i=1}^{N} Channel\ Width_i$, for all channel segments *i* where $Water\ Elevation > Bed\ Elevation$	m
Hydraulic Radius	R = A/P	m
Shear Velocity	$U^* = \sqrt{gRS_e}$, where g is the acceleration due to gravity and the energy slope S_e is used as an approximation of $\sin(\theta)$.	m/s
Mean Velocity	$U = Q/A$, where Q is the discharge.	m/s
Unit Stream Power	$\omega = \frac{\rho g Q S_e}{b}$, where ρ is the density of water and b is the channel width and the energy slope S_e is used as an approximation of $\sin(\theta)$.	Watts/m^2
Mean Boundary Shear Stress	$\bar{\tau} = \rho g R S_e$ and the energy slope S_e is used as an approximation of $\sin(\theta)$.	Pascals
Froude Number	$Fr = \frac{U}{\sqrt{gR}}$	Unitless
Reynolds Number	$Re = \frac{UR}{\upsilon}$, where U is the mean velocity, R is the hydraulic Radius, and υ is the kinematic viscosity for water, 10^{-6} m^2/s	Unitless

Potential for Bedload Transport

In cobble-bed streams in which the bed material is a mixture of grain sizes, significant movement of bed material requires movement of larger particles so that the smaller ones are able to move. The basal shear stress required to move the D_{84} grain size is commonly used to identify if significant movement of the bed material via bed breakup is occurring. Bedload transport may occur at lower shear stresses, particularly in zones with smaller surface bed particles; this movement will not significantly reform the channel or generate sustained bedload movement. Initiation of motion is defined

using the critical dimensionless shear stress criterion, t_{crit}* which is the ratio of the basal shear stress to grain resisting forces (Shields, 1938). Heterogeneous beds break up at lower dimensionless (e.g. Parker and Klingeman, 1982). Using the D_{84} as the reference grain size, the equation is

$$\tau_{84}^{*} = \frac{\tau}{(\rho_s - \rho_f) g D_{84}} \quad (23)$$

Where τ is the basal shear stress, ρ_s is the sediment density assumed to be quartz (2650 kg/m^3), ρ_f is the fluid density (water; 1000 kg/m^3), g is the acceleration due to gravity and D_{84} is the 84th percentile grain size. For a cobble bed stream in, the dimensionless shear stress required to move grains is experimentally determined to be 0.045 (Komar, 1987; Petit et al., 2015). Inserting the constant values and rearranging to solve for the critical shear stress, we find that

$$728.4 * D_{84} = \tau_{crit} \quad (24)$$

Using the range of D_{84} values determined at the cross section positions shown on Figure 23, which range from 0.120 to 0.176 m, the critical shear stresses to enable bed breakup is estimated to range from 87.4 to 128 Pascals.

Potential Non-Fluvial Sources of Ambient Seismic Energy

Because atmospheric phenomena (primarily precipitation and wind) can create high-frequency seismic signals (i.e. Roth et al., 2016), the closest, highest resolution atmospheric data possible was collected to assist in signal interpretations. Data from a personal weather station (PWS) KMDSILVE44, which provides rainfall intensity and wind gust speeds at five minute intervals and is located approximately 1 mile from the study reach (Weather Underground, 2018).

As the study location is within an urbanized area, the noise from traffic is a potential source of high-frequency seismic interference. During the 2017 and 2018 time period, hourly counts of the total number of cars on the nearest major interstate, I-495, were retrieved from permanent monitoring station P0041 located .82 miles West of Maryland State Route 650 on Interstate I-495. The source of the data is the Maryland State Highways Administration (2018), as reported on the Internet Traffic Monitoring System (I-TMS). The total of both eastbound and westbound traffic was used.

Results

Reach Hydraulics

At-A-Station Hydraulic Geometry

At-a-station hydraulic geometry is the relation between a river's discharge (Q) and its width (w), mean depth ($\bar{d}$), and mean velocity ($\overline{U}$)at a particular cross section. The width, mean velocity, and mean depth are constrained to discharge by continuity. The power relationships between width, mean velocity, and mean depth with discharge are formulated as power relationships, and the scaling exponents and coefficients are useful empirical measures of channel shape and roughness (Leopold and Maddock, 1953). Using the channel elevation model presented in Figure 23 and the hydraulic variables described in Table 4, simulated hydraulic geometry relationships at each of the eleven cross sections in the study reach are created. Each relationship is constrained so that:

$$Q = \overline{U} * \bar{d} * w \tag{25}$$

and adjusted so that the exponents sum to 1 and the coefficients multiply to 1, as described by Leopold and Maddock (1953). The coloring on the figure indicates the

downstream position of each cross section. In this analysis, the channel is assumed to remain constant throughout the study period and the discharge is calculated from the simulated rating curve shown in Figure 21. Only discharge data from the six-month 2017 dataset is used in the below analysis. The coefficients and exponents for each cross-section are listed in Appendix D.

In the simulated at-a-station hydraulic geometry, in many of the cross section locations, there are three breaks in slope representing three distinct channel shapes. Figure 26 shows the at-a-station hydraulic geometry relationships for the three cross sections closest to the three along-channel nodes. Node 1 is upstream and Node 3 is downstream. The two upstream cross sections display a fairly continuous scaling with discharge above 0.8 m^3/s. The most downstream cross section, is wider, deeper, and slower at low discharges. Above a discharge of 15 m^3/sec, there is a break in slope at this downstream cross section. The increase in discharge becomes increasingly accommodated by increases in width, rather than increases in discharge and velocity.

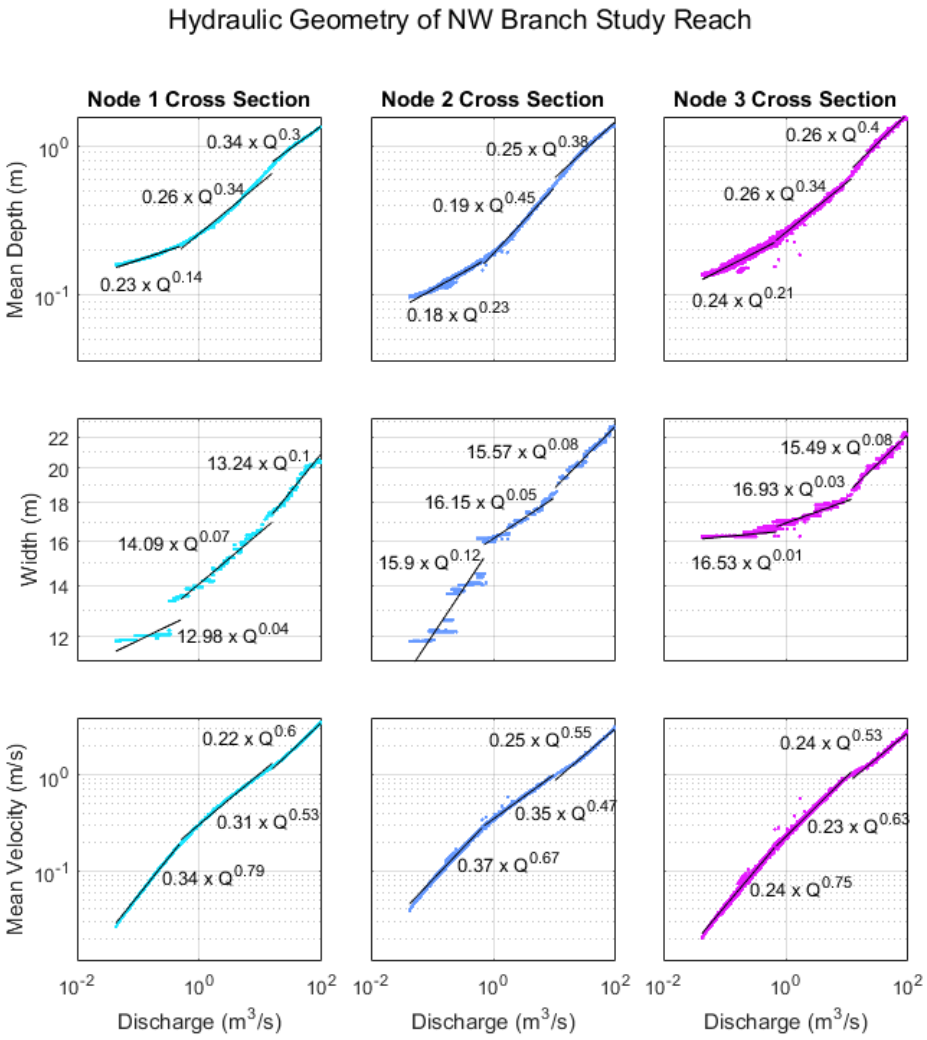

Figure 26: Hydraulic Geometry Relations for three cross sections adjacent to nodes 1-3. There are two breaks in slope in the hydraulic geometry relations. The cross section at Node 3 is wider and slower at low discharge and has a decreasing velocity exponent at the highest discharge.

Because the greatest seismic energy is observed at high discharge, the hydraulic geometry during the highest discharge is of most interest for this fluvial-seismic study. According to Leopold and Maddock (1953), if the velocity scaling exponent is greater than the depth exponent, the reach can be classified as a pool. In a riffle sequence, the depth exponent exceeds the velocity exponent. Figure 27 shows the depth exponent divided by the velocity exponent as a function of downstream distance for the 11 cross sections measured in this study. The relationship between these two exponents is fairly

uniform and the velocity exponent does not exceed the depth exponent except for in a single cross section 60 meters downstream. The ratio of the depth exponent to the width exponent describes the shape of the channel, with higher values leading to steeper sides (approaching a rectangular shape at infinity). Again, the channel shape is relatively uniform throughout the reach, though the steepest banks appears at 60 meters downstream. At this cross section, the stream is particularly shallow and wide, with steep banks.

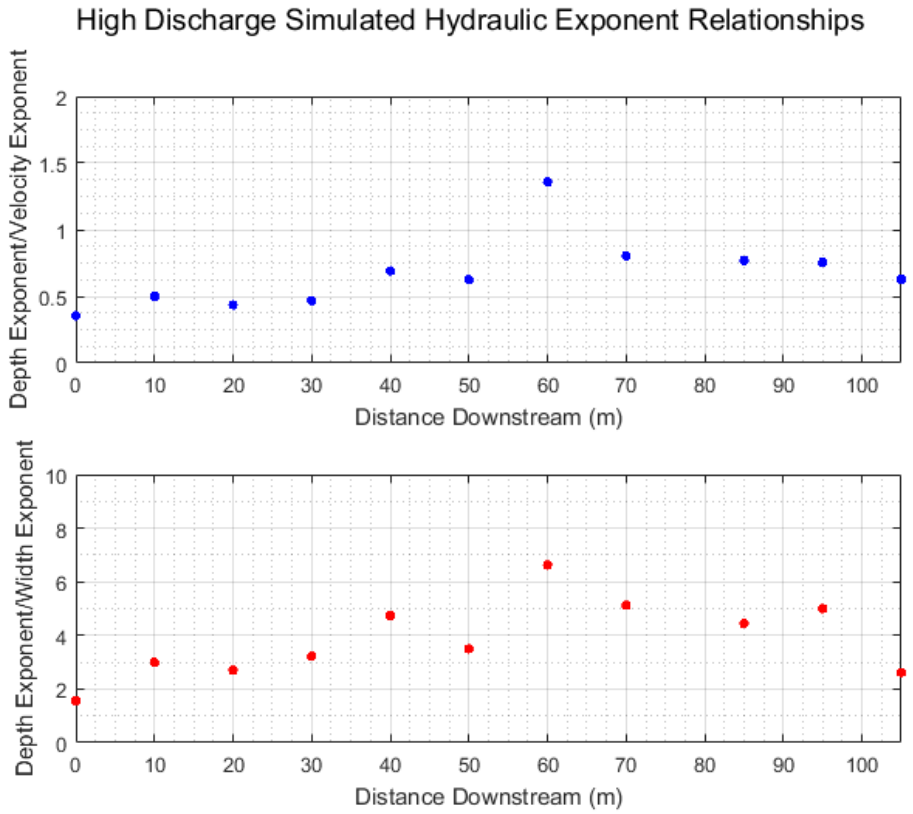

Figure 27: The top panel indicates that the velocity exponent is generally greater than the depth component, which is typically seen in pools. The bottom panel displays that the depth/width exponent ratio, which reveals the steepness of the channel banks. The hydraulic geometry relationships for the highest discharge indicate a wider and shallower section is present at 60 meters downstream.

Water Surface Slope and Energy Gradient Dynamics

The energy gradient consists of the sum of pressure energy, kinetic energy, and potential energy. For uniform and steady flow, the energy gradient of the river is equal to the water surface slope should equal the slope of the bed. In many fluvial studies, the approximation of uniform and steady flows is made. In the study reach during floods, however, there are variations in channel geometry that leads to downstream variability in the mean velocity, due to the conservation of mass in the reach section. In this case, the energy gradient is not equal to either the water surface slope or the bed slope. Calculating the true energy gradient would require observations of flow velocity, hydrostatic pressure, and flow divergence or convergence at two points along a streamline. In the following analysis, the variations in water surface slope are first assessed, then the effect of velocity variations in the reach is accounted for. The energy gradient is approximated using the average of the mean flow velocities the two cross sections closest to the pressure transducer locations.

The relationship between water surface slope and discharge in the study reach suggests that the upstream and downstream river sections behave differently during floods. Figure 28 shows the water surface slopes observed in this study for the 2017 and 2018 study periods. In the upstream section (from 0 meters downstream to 55 meters downstream) the water surface slope steepens with increases in discharge, approaching a maximum slope of 0.005 at high discharge. In the downstream section (from 55 meters to 85 meters downstream), the slope slightly increases with discharge up until approximately 10 m^3/s, then begins to decrease in slope, also approaching a slope of 0.005. Observations of flow behavior at 3.6 m^3/s (on July 22nd, 2018) and 1 m^3/s (on July 30th, 2017) were collected on video. In both cases the upstream section

had deeper, slower moving flow than the steeper downstream section, consistent with the slope observations.

The decreases in slope at high discharge are interpreted to result from the bed elevation profile, as depicted in the conceptual diagram in Figure 29. As the river approaches bankfull stage, the water surface forms a single linear slope, which submerges the variations in bed slope. This linear slope decreases at higher discharge, as the river's velocity is slowed by additional roughness and vegetation on the banks. The effect of this flattening out is far more pronounced in the downstream section that the upstream section. As a result, applying the overall slope between 0 and 85 meters downstream would be inappropriate for calculating basal shear stress at the locations of nodes 1 and 2.

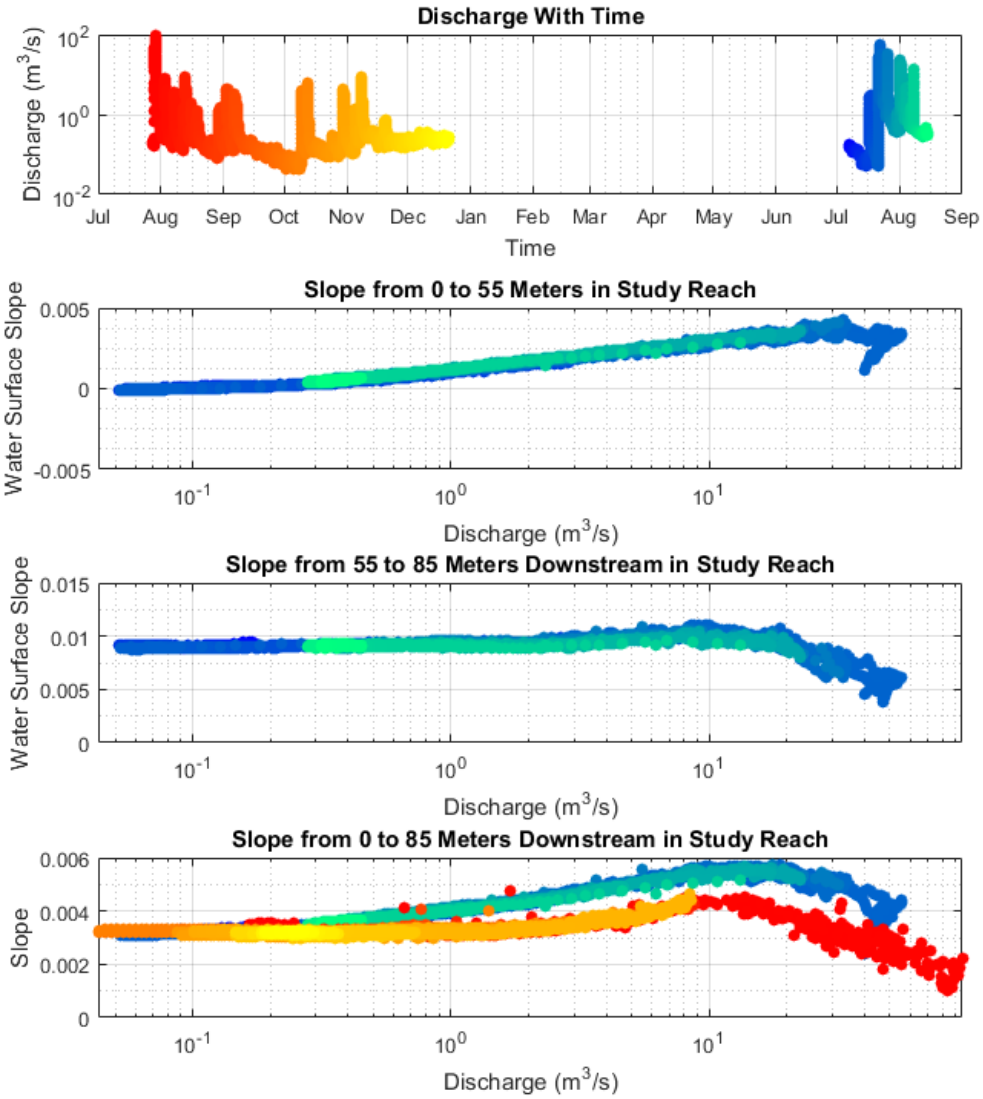

Figure 28: Panel A shows the discharge collected for the 2017 time interval in red and the 2018 time interval in blue. Panel B shows the upstream and C shows the downstream gradient in water surface elevation as reported by pressure transducers, whose location is shown in Figure 25. Panel D shows the slope for the entire river segment, which was recorded in both time intervals and shows similar dynamics with discharge in both years. The upstream reach gets steeper with increasing discharge while the upstream reach becomes less steep above 10 m^3/s.

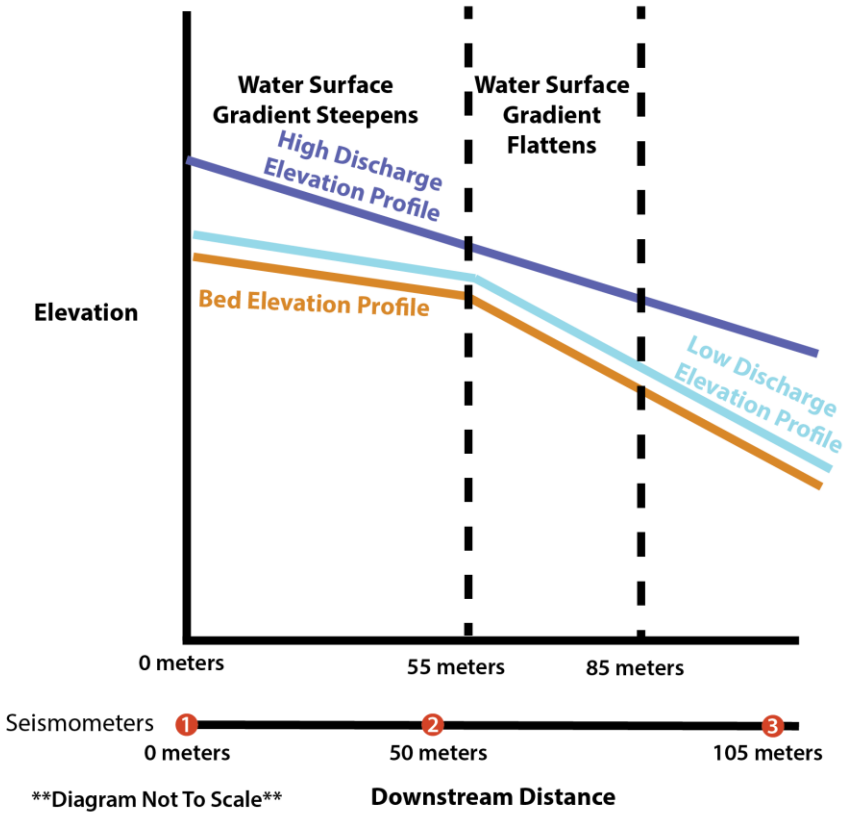

Figure 29: Conceptual diagram describing the water surface slope dynamics observed in the study reach.

In the study reach, the cross sectional area at high discharge is smallest at the most upstream gauge, increases at the gauge 55 meters downstream, then decreases again at the gauge 85 meters downstream. As a consequence of this, including the velocity heads leads to a steeper energy gradient than water surface slope in the upstream section, as water decelerates in this portion of the reach (Figure 30). In the downstream section, water slightly accelerates, leading to a less steep energy gradient than water surface slope. Including the velocity head suggests that at ~50m^3/s, there is a reversal in gradient such that the upstream portion approaches a gradient of 0.006 while in the downstream portion the slope approaches 0.003. The apparent sharp break in slope at 55 meters downstream reflects that the energy gradients in these two sections are the average gradient and a sharp break in slope is not necessarily

expected at the middle pressure transducer.

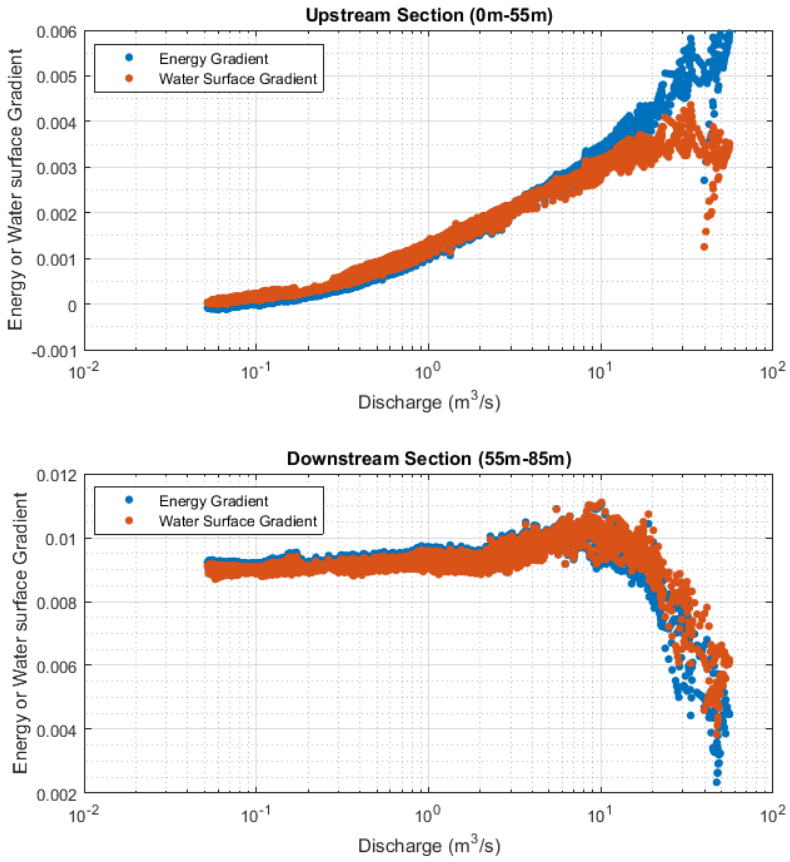

Figure 30: Energy gradient and water surface slope in the study reach during the 2018 study period.

The water surface elevation at 55 meters downstream was not collected during the 2017 flow period when the greatest discharge was observed. In order to reconstruct the energy gradient in this section of the study reach, the relationship between discharge and energy gradient from 2018 was fit with a piecewise power function. This fitting method was determined due to a break in slope in the relationship at approximately 1 m^3/s. The fitted relationship is shown in Figure 31 below. Abnormally low slope values at high discharge were excluded from the analysis. These could be related to the

channel-lateral inflow of the tributary just upstream of the study reach. The range of the discharge in the 2018 dataset is not as great as the 2017 dataset, so extrapolation along the red fit line in Figure 31 is required. In the 55 to 85 meter river segment, the complex behavior was fit with a polynomial function. As consistent with the conceptual diagram above, the slope was extrapolated to a gradient of 0.002 using a linear function to reach the highest discharge observed in 2017.

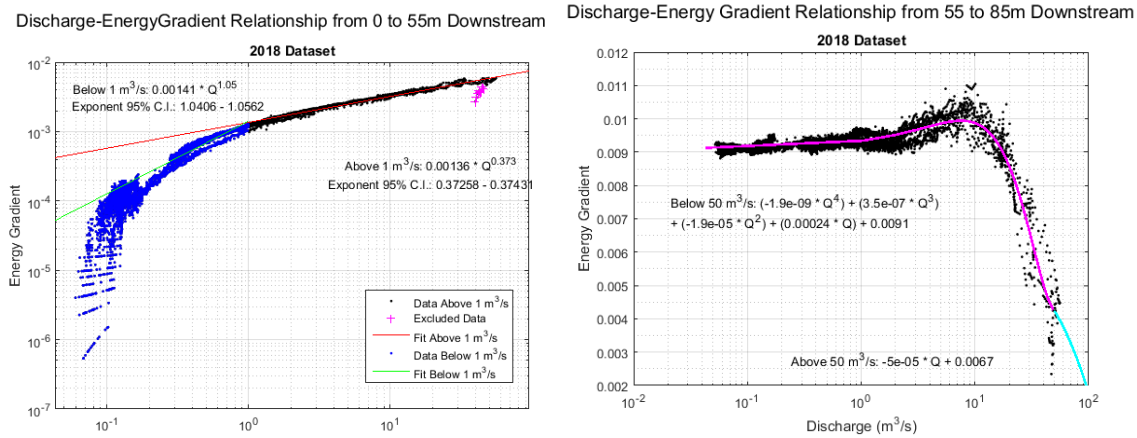

Figure 31: The left panel shows the relationship between energy gradient and discharge, fit by two piecewise power functions. The energy gradient-discharge relationship is extrapolated at the maximum discharge observed in 2017. The left panel is the relationship between energy gradient and discharge, fit by a polynomial relationship and also extrapolated to a value of 0.002.

Using these energy gradient-discharge relationships, observations of water surface elevation, bed elevation, and grain size, the hydraulic variables are computed for the entire range of discharge values during the study period. While 11 channel cross section elevations were surveyed (to a distance of 105 meters downstream), there are only energy gradient observations to the downstream pressure transducer at 85 meters downstream. The hydraulic variables are only calculated to 80 meters downstream as a result. The results for the nine cross sections are shown in Figure 32, with blue and

pink colors representing the upstream segment and brown and black colors representing the downstream segment.

In Figure 32a and 32b, the hydraulic radius and maximum depth increase with discharge in a way that reflects the channel shape. Figure 32a is equivalent to the average depth scaling presented in the hydraulic geometry relationships above, while in 32b the increases in maximum depth reflect the stage increases. An estimated power fit is shown in Figure 32b for use in a later section- the fit slightly overestimates at high discharge but is a reasonable estimate. Figure 32c shows the cross-section average shear stress, which is much lower than the cross-section maximum shear stress shown in Figure 32d due to the low depth sections at the channel margin. In both shear stress figures, the influence of the water surface dynamics is evident: at low discharge, the steeper downstream river section has a higher shear stress. Above 30 m^3/s, the shear stress in the downstream section decreases due to decreasing energy gradient. At high discharge, a shear stress reversal is observed. The shear stress required to initiate motion for bedload with a D_{84} of 120 mm is shown in Figure 32d. While in the deepest portion of the channel (Figure 32d), bedload transport is expected to occur, bed breakup is not expected as the mean shear stress (Figure 32c) does not approach the shear stresses required to initiate motion.

The calculated mean velocity, shown in Figure 32e, increases nearly linearly above 10 m^3/s to 4 m^3/s, which is very rapid. With increasing discharge, the channel becomes increasingly hydraulically smooth, as indicated by the higher U/U* ratio in Figure 32f. The unit stream power, which includes water surface gradient has different behavior in the upstream and downstream river segments and increases to nearly 400

watts/m^2 in the upstream portion of the reach 100 watts/m^2 in the downstream portion (Figure 32g). The Reynolds number (Figure 32h) increases nearly linearly, indicating that highly turbulent flow is present. Submergence, or the ratio of the depth to the particle roughness as represented by the D_{84}, increases similarly to Figure 32a, though there is additional variability due to the differing grain sizes observed at each river cross section. The Froude number, calculated with mean velocity, increases to near one at the highest discharge. As the local velocity within the channel will often exceed the mean velocity, there is a reasonable expectation that supercritical flows are observed during high discharge.

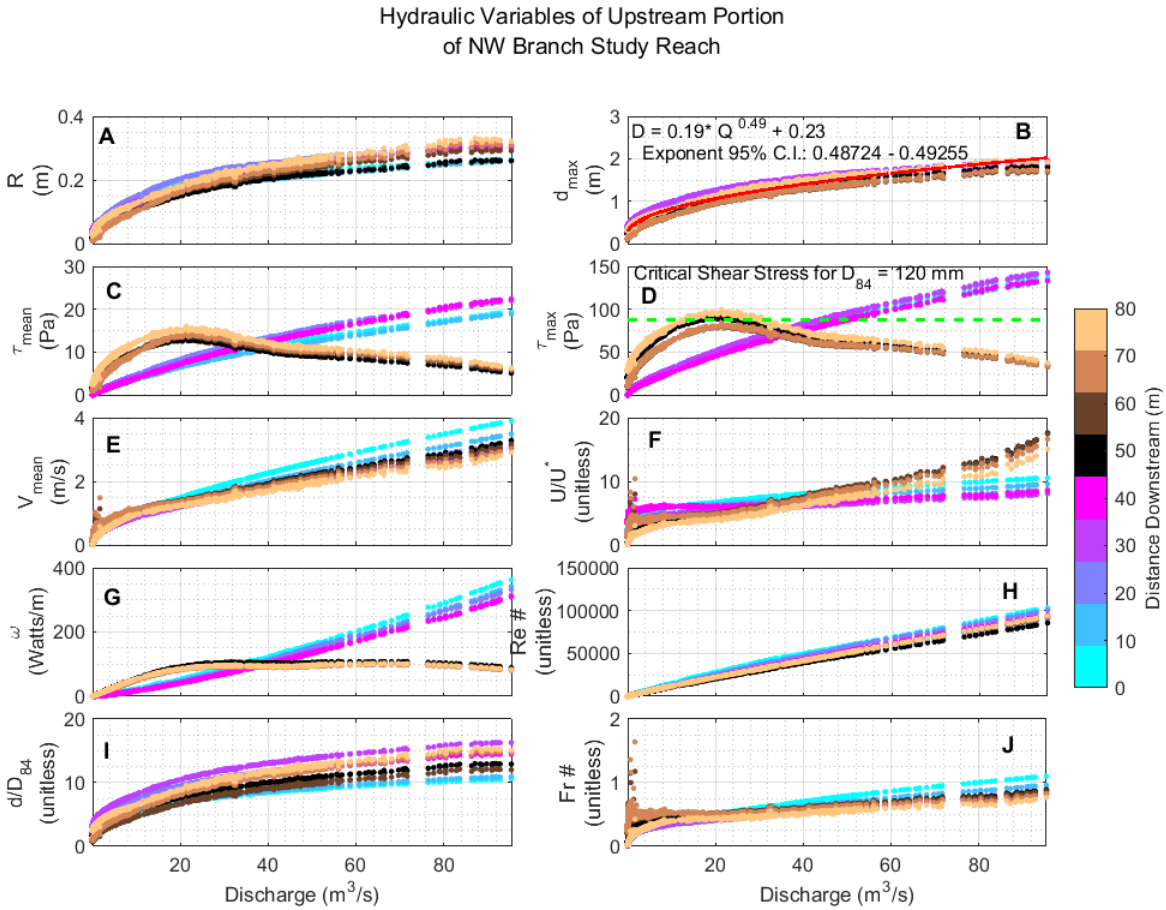

Figure 32: Relationships between hydraulic variables and discharge for nine cross sections for which energy gradient is available. Blue and pink colors represent the upstream reach and the upstream slope is used to calculate shear stress, shear velocity, and stream power in panels C,D,F and G. Brown and black colors represent the downstream river section.

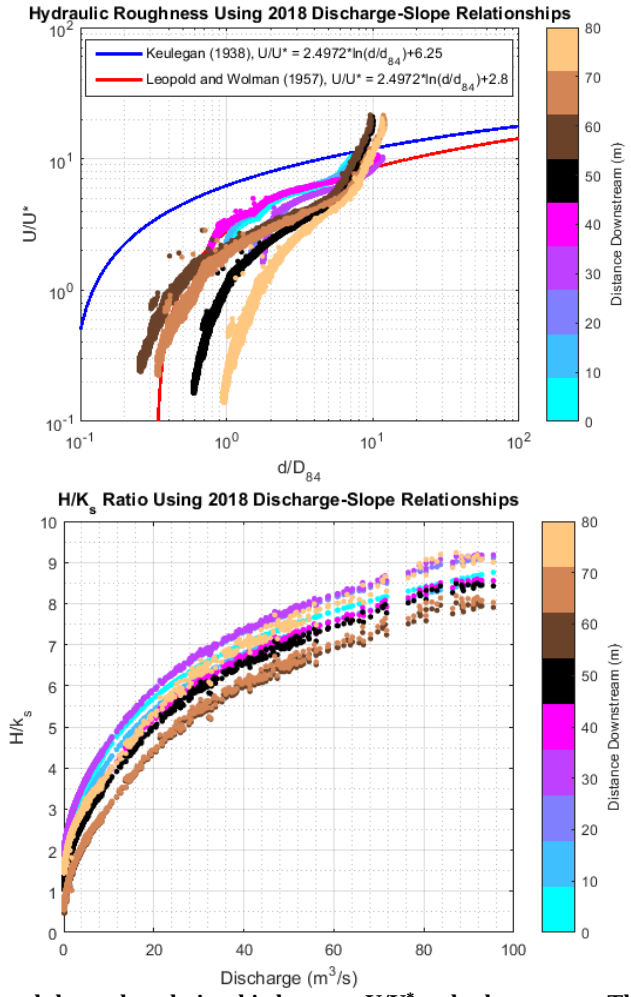

Figure 33: The top panel shows the relationship between U/U* and submergence. The steeper downstream river segment is hydraulically rougher than the upstream segment. The bottom panel shows the river depth to the roughness height, k_s. As defined in Gimbert et al. (2014), K_s is three times the D_{50}.

The top panel of Figure 33 shows the submergence and U/U* relationship, a dimensionless way to represent the resistance to flow in the channel. The downstream river segment is shown to be hydraulically rougher at low relative submergence. The values indicate the channel is rougher than the relationship established by Leopold and Wolman (1957) for gravel at low discharge, though at the highest discharge the channel becomes as hydraulically smooth as the relationship established for a flume (Keulegan (1938). An explanation for the high observed U/U* values is that the incised and channel contains the flow, allowing for greater water depths and greater hydraulic

smoothness than an un-incised channel. The bottom panel shows the maximum river depth to roughness height (three times the D_{50}) as defined in Gimbert et al. (2014).

Observed Seismic Power

The three-component seismic signal recorded by the nodes was processed identically to the methods in Chapter 2 for the Oroville Dam dataset, though in five-minute time windows rather than hour-long time windows. First, instrument response was removed using response information provided by Ringler et al. (2018). The corrected signal is divided into 19 even-length subwindows, each of which are tapered with a hamming window and overlap by 50%. The Fast Fourier Transform of each window is calculated and the signal power at each frequency averaged across the 19 subwindows. The result of this processing is a timeseries of the average five-minute power spectral density in 3751 frequency bins from 0.033 Hz to 125 Hz. A timeseries for the power in each component as well analysis is used to characterize the stream dynamics. The time averaging employed limits the influence of transient events in order to isolate the ambient seismic signal.

Anthropogenic Diurnal Variation in Seismic Noise

Although the study location within Burnt Mills East Special park was selected due to its distance from roadways, a diurnal variation in the ambient noise shows that the seismic observations are influenced by anthropogenic noise, likely including traffic. This anthropogenic signal appears across a broad range of frequencies. Figure 34 shows the daily variability during a week in September 2017 when no precipitation occurred and the Northwest Branch remained at low baseflow conditions (discharge is less than 0.15 m^3/s), so the source of the variability is not fluvial. This daily signal is observed

in all three components, at all frequency ranges above 1 Hz and has an amplitude of approximately 15 decibels. In Figure 35, this daily signal is highly correlated with the number of vehicles per hour (both eastbound and westbound) on I-495. The top left panel shows that the normalized, scaled signals of traffic and seismic power oscillate daily. The other three panels show a semi log relationship between seismic power (in logarithmic decibel units) and the number of cars per hour. However, the source of the anthropogenic data is likely all area roads and human activity, so the number of vehicles per hour should be considered a proxy for human activity. In the 20-30 Hz band, the ambient noise environment ranges from -120 to -115 dB in the horizontal components and -125 to -115 dB in the vertical component. The discrepancy between components will be discussed in a later section.

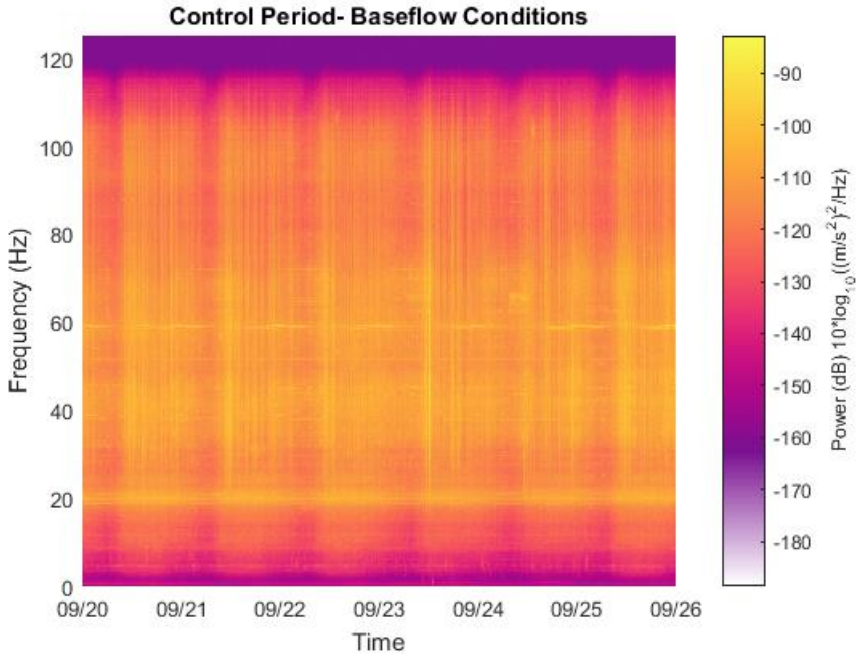

Figure 34: Spectrogram showing the five-minute average power at each frequency bin for a period of low baseflow conditions in September, 2017. A daily increase in power is evident, across a broad range of frequencies. The figure shows the North-South

While it may seem possible to remove this daily noise signal, efforts to do so resulted in the removal of all observed fluvial signals. In the urbanized and flashy stream, the duration of storm hydrographs is often approximately one day, so filtering a daily oscillation removes the desired response to storm hydrographs. Therefore, in the following analysis, the daily signal remains and sets the threshold above which the fluvial signal is distinguishable from the background noise environment. Figure 36 shows how there is little relationship between river discharge and seismic power below 5 m^3/s for Node 1 during the 2017 study period. The figures for all nodes are shown in Appendix E. This discharge is therefore defined as the threshold for which the river is observable in the noise environment and with the instrumentation.

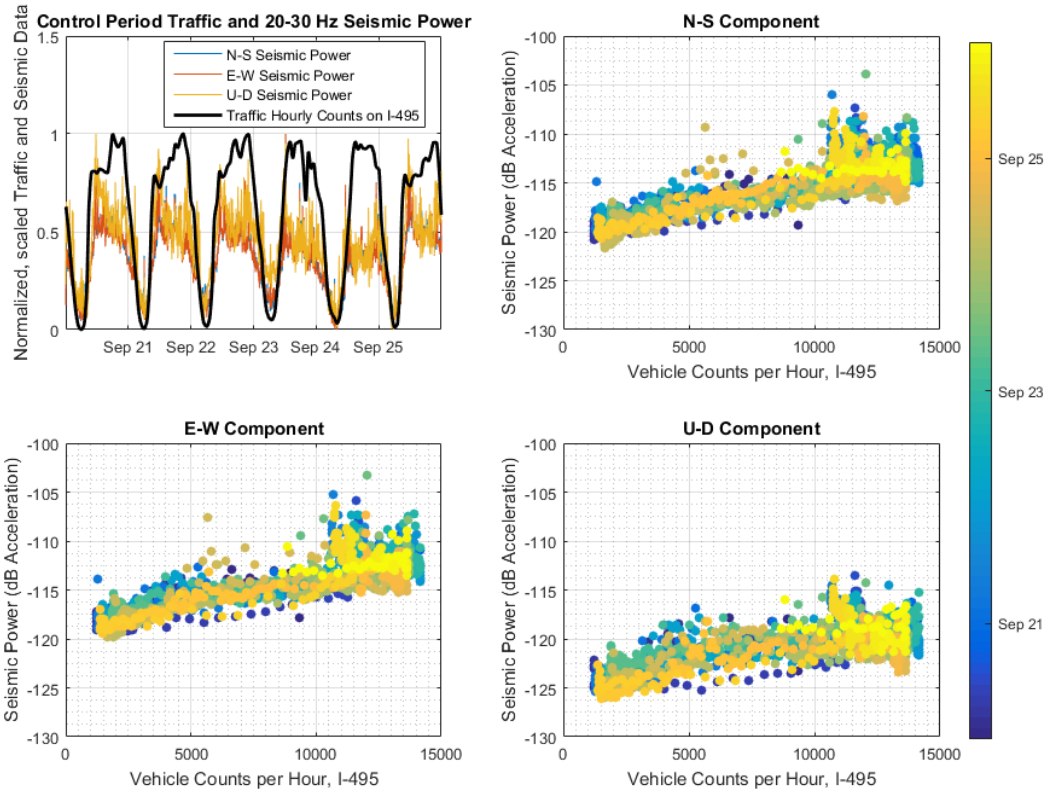

Figure 35: Relationship between daily power variation in the 20-30 Hz band for Node 2 and traffic counts per hour on I-495. Figure 35a shows the scaled traffic and power time series. Traffic typically peaks in the afternoon while seimic power peaks in the morning. At night, both traffic and power are low. Figures 35b-d show the relationship between seismic power and vehicle counts, colored by time. An increasing trend is observed, though there is significant scatter at high vehicle counts.

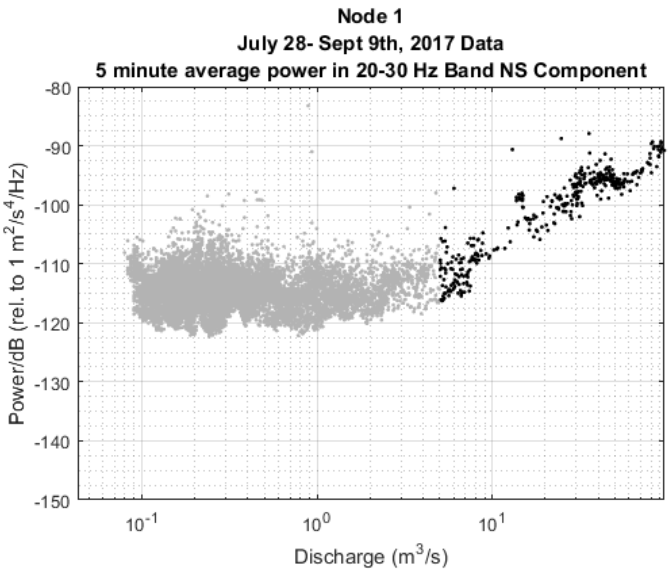

Figure 36: Relationship between river discharge and five-minute mean power in the 20-30 Hz band. Above 5 m^3/s, there is a relationship between seismic power and discharge. Below this threshold, ambient noise is too great to observe the river.

Spectrograms of Five-Minute Average Power

The dynamics of seismic power observed by near-stream nodes are summarized using seismograms of the five-minute mean power in each component. Figure 37 shows the spectrograms for the first and largest flood event. The power in the north-south component is shown, though all three components show similar patterns. Appendix F shows the spectrograms for the first week of data collected in the 2018 interval. The discharge is shown as a black line on the spectrogram figures. The spectrograms for all flood events show several common features.

First, at low discharge in the Northwest Branch, the diurnal variability present during the "Control" period spectrogram is readily apparent. Second, power on all six nodes increases in the 40-120 Hz band during precipitation events, slightly preceding river discharge increases. The sharp increases in power are highly related to precipitation rate, shown in green on the spectrogram figures. This is most apparent in

Node 5, which is furthest from the river. The 20-30 Hz band examined in greater detail in a later section has limited influence from precipitation. In nodes 1 through 3, which are closest to the river, increases in power during high discharge are maintained across a broad frequency range. In nodes 4 and 5, the power increases at high discharge are not sustained for a long time.

Node 3 exhibits behavior unique among the nodes. Figure 38 shows a closer look at the Node 3 North-South component spectrogram from 0 to 50 Hz. At a river discharge above approximately 0.5 m^3/s increases in seismic power occurs at discrete frequencies, which appear in the spectrograms as a series of equally spaced horizontal lines. With changing discharge, the frequency of these high power bands changes. At higher discharge, the frequencies become lower. On the falling limb of the hydrograph, these horizontal bands plateau and then abruptly change at a discharge of approximately 0.5 m^3/s.

We attribute these characteristics to two downed trees extending into the river near Node 3, shown at baseflow and at the falling limb of a hydrograph in Figure 38. The trees are likely vibrating with the turbulence of the river flow. These vibrations appear as harmonics in the spectrogram, which vary with discharge as the length of the un-submerged section (and therefore the resonant frequency) changes with river stage. The equation describing the resonant frequency at various integer modes N is

$$f = \frac{Nv}{2d} \tag{26}$$

where f is the frequency, N is the mode number, v is the velocity of the wave, and d is the length of the oscillator. For a tree laying on the bank, the velocity of the wave within the tree trunk is assumed to be constant. The frequency will therefore depend inversely

on *d*. As the length of tree extending submerged in the river is the oscillating component, the frequency of oscillation should decrease with increasing discharge as observed. Since local effects of the submerged trees appear to be significant contributions to the seismic signal throughout a broad range of frequencies, the seismic data from Node 3 is considered compromised by the tree interference. Node 8, deployed during the 2018 time period, also shows the effects of tree resonance, as it is the next closest node. Spectrograms for Nodes 3 and 8 are shown in Appendix G.

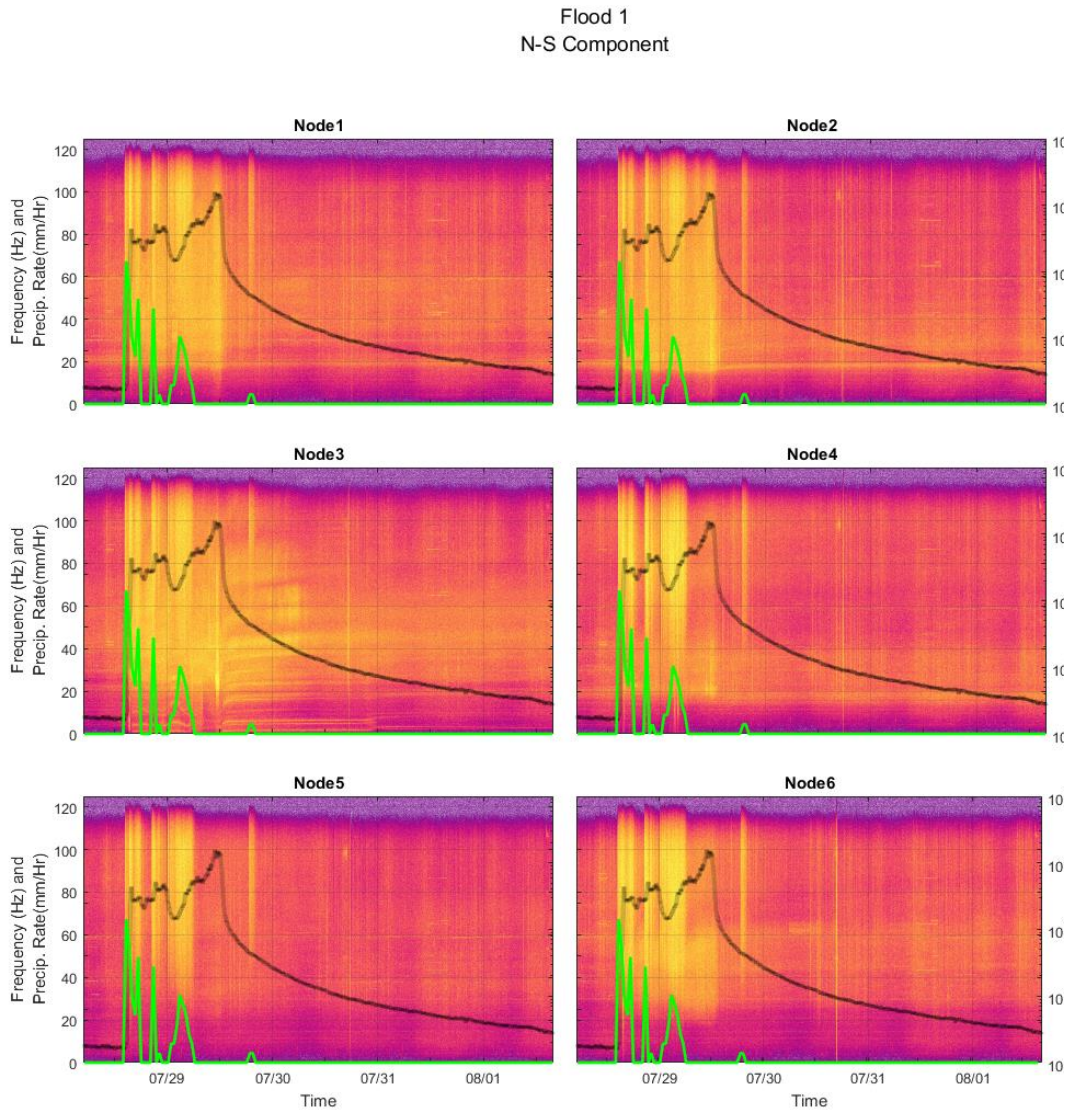

Figure 37: Spectrograms of five-minute mean power at each frequency bin in the north-south component. The data for the first and largest flood (recorded in 2017) is shown using the six nodes deployed at the time. The black line indicates the discharge while the green line indicates the precipitation rate recorded by a nearby weather station.

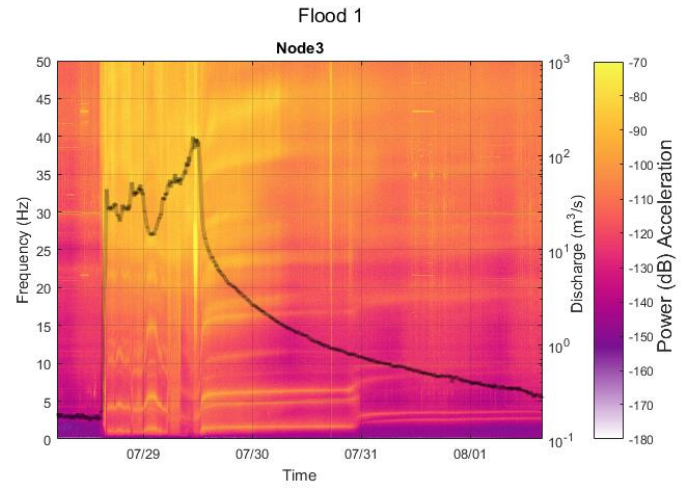

Photo Taken: 12/21/2017 at 8:51 AM EDT
Discharge: 0.24 m³/s (8.6 ft³/s)

Photo Taken: 7/22/2018 at 9:24 AM EDT
Discharge: 4.1m³/s (145 ft³/s)

Figure 38: Top panel: Spectrogram for Node 3 during first flood event up to 50 Hz. Middle Panel: The location of node 3 with the river at baseflow, with minimal contact between the river and the trees. Lower Panel: The river at elevated discharge, showing tree contact with the river.

Five-Minute Average Power and Hydraulic Variable Scaling

To investigate the along-stream variability of fluvial energy dissipation and the most appropriate metric to characterize fluvial energy dissipation, the scaling relationships between the discharge, maximum shear stress, U/U*, and the 5-minute mean power is examined. The 20-30 Hz frequency band is selected due to the lesser influence by precipitation events.

Discharge

In Chapter 2, a power function relationship between discharge and seismic power is identified and is used to infer information about the turbulence within the Oroville dam flood control spillway. At the river reach scale, the scaling exponent between seismic power has been examined by previous authors to infer variations in turbulence and bedload transport (Roth et al., 2016; Gimbert et al., 2016). Figure 39 shows the relationship between mean seismic power in the 20-30 Hz Frequency band for all eight nodes. Data collected from July 28th – September 9th, 2017 is displayed using black markers and fit with a red power function. Data collected from July 22nd – August 17th, 2018 is displayed using blue markers and fit with a green power function. Not all nodes were collecting data during both time periods, as shown in Figure 25.

The scaling relationships between seismic power and discharge have some consistent trends among the different observation locations. For all nodes except Node 5, which is furthest away from the river, the horizontal components have a greater scaling exponent than the vertical component. This is consistent with observations reported by Anthony et al. (2018), Barrière et al. (2015), and Schmandt et al. (2013), all of whom reported greater responsiveness to discharge in the horizontal components of near-stream geophones. There is greater variability in the 2018 seismic dataset

compared to the 2017 dataset, which is represented as lower R^2 values in the power relationship fits. The reason behind this difference in the variability of the seismic observations is not clear, though the presence of nearby construction activities, initially assumed not to take place while the river is flooding, may be a contributor to the variability in seismic power.

For several of the nodes, there appears to be two parallel lines with the same slope though different coefficients in the power relationship, particularly below 8.5 m^3/s. To examine if this may be due to the daily anthropogenic noise observed at the site, the seismic power and discharge results were colored by the hourly rate of cars/hour on I-495 during that interval. These results are presented in Appendix H. These lower power intervals do occur at low traffic volumes, indicating a potential for the scaling results to be biased by the daily oscillation of anthropogenic activity. As a first-order evaluation on the influence of human activity on the discharge-power scaling exponents, the scaling analysis between discharge and seismic power was performed for only time intervals where the traffic volume on I-495 was below 5000 cars/ hour. The results presented in Appendix H show that the scaling exponents are only slightly affected by limiting the analysis to these periods, while the R^2 values are decreased. The highest discharge happened to occur during periods of high traffic volume, so excluding all high traffic volume time periods limits the range of discharge observations. Therefore in the following analysis, we use all available data to evaluate scaling relationships.

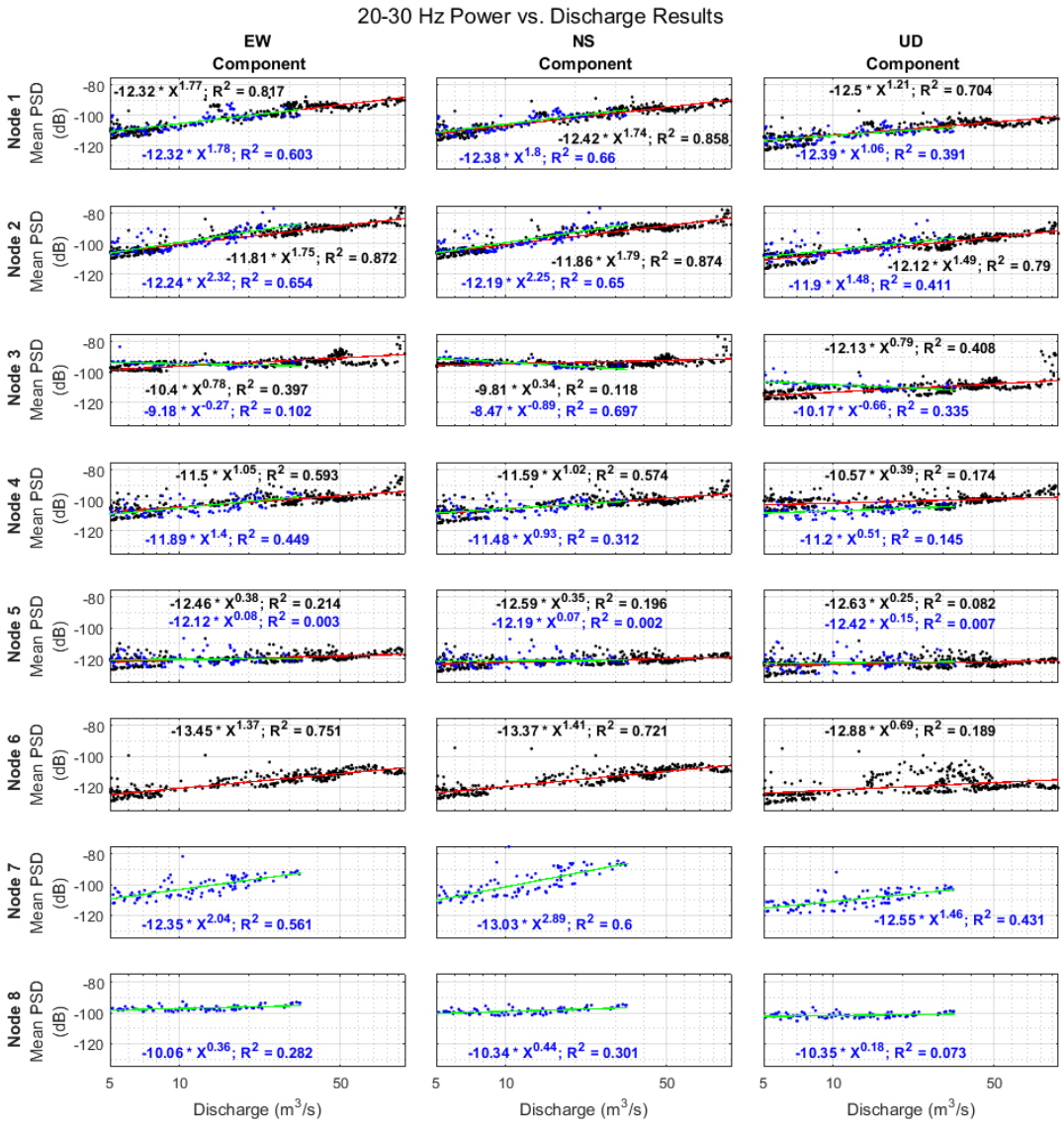

Figure 39: Discharge and power scaling relationships for all eight node positions in this study. Black markers and red curves indicate 2017 data and power relationships, while blue markers and green curves indicate 2018 data and power relationships.

While the observations at Nodes 1 and 2 show a consistent power relationship between discharge and seismic power, Node 3 shows a more complex relationship. At high discharge, the seismic power levels off or even slightly decreases, creating a relationship not fit well by the power relationship. This behavior is most noticeable in the horizontal components. The scaling exponents and R^2 values for Node 3 are lower

than Nodes 1 and 2. The decrease in seismic power at high discharge observed in Node 3 is likely a result of the vibrations of the two downed trees adjacent to the node, as discussed previously. The seismic vibrations produced by the trees appear to move to lower frequencies at high discharge, which could pass out of the 20-30 Hz frequency band.

While the 20-30 Hz frequency band qualitatively provides the best relationship for all nodes, the varying river-to-seismometer distances across the array may lead the peak frequency of the fluvial noise to be at a different frequency band. Figure 40 shows the scaling exponents obtained from the power relationship between mean seismic power and discharge above 5 m^3/s in 10 Hz frequency bands. The figure shows relationships established using the July 28th – September 9^{th,} 2017 for the six nodes deployed in 2017.

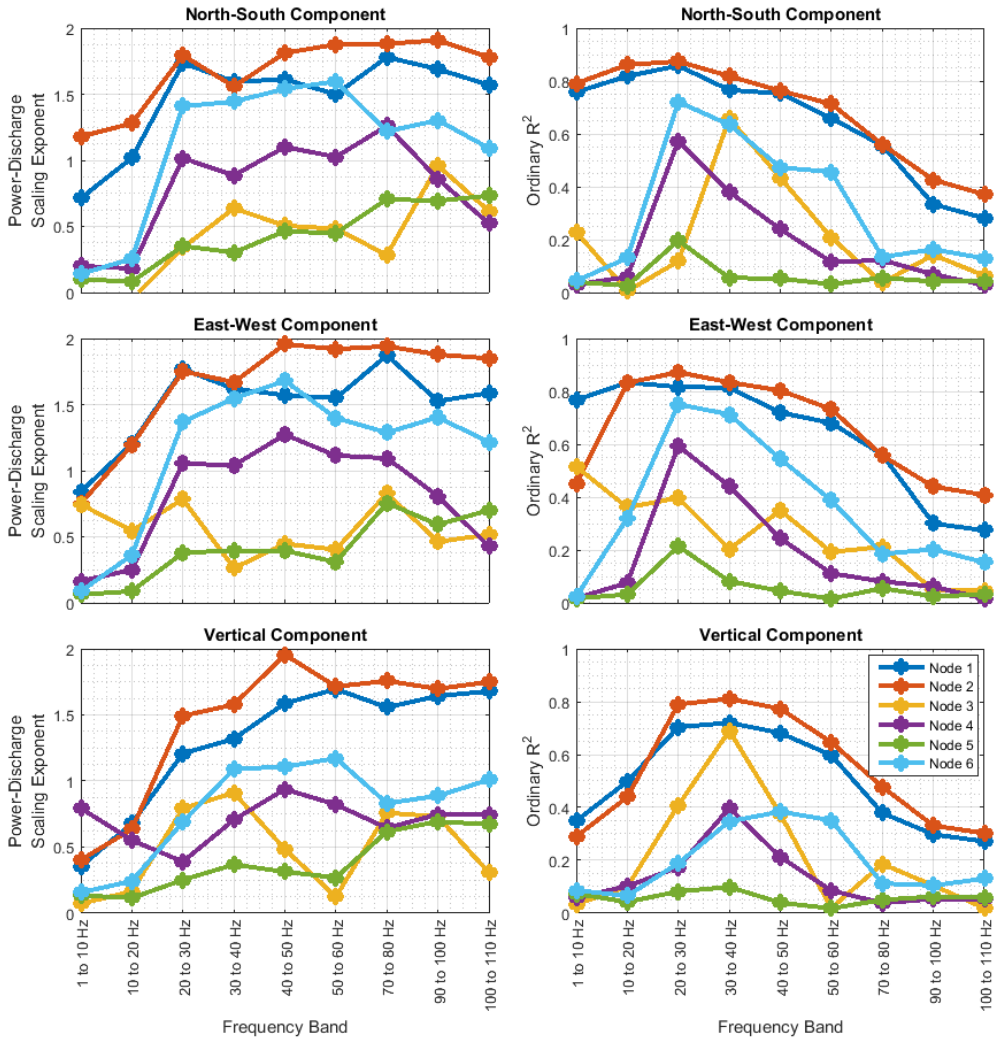

Figure 40: Left column of figures indicates the power-discharge scaling exponent in 10 Hz bins for each node. The right column shows the R^2 value. R^2 and scaling exponents are greatest generally between 20 and 50 Hz. The greatest exponents and R^2 values are observed in Nodes 1 and 2, closest to the river, while Node 5, furthest from the river, has lower values of both.

In general, the three nodes closest to the river (Nodes 1 and 2) are most responsive to variations in discharge, though Node 3 has a lower scaling relationship and its power is less well correlated with discharge than Nodes 1 and 2. The Node furthest from the river (Node 5) generally has the lowest power scaling exponent. The greatest linear fit between power and discharge for all nodes occurs in frequency bins

between 20 and 50 Hz, supporting the use of the 20-30 Hz frequency band in following sections because of the consistent high R^2 value across components. Figure 40 shows that the scaling relationship is greater for the two horizontal components than the vertical component. Greater R^2 values are also observed in the horizontal components.

If the scaling exponent is to characterize the turbulent energy dissipation in a stream, as proposed by many authors, this scaling should be stable and reproducible between field sites. One largely unexplored issue in the fluvial-seismic literature is how far away a seismic observation should be from the river. With the array geometry of this study, we can observe how the power scaling exponent and R^2 co-vary with distance from the river. Figure 41 shows the relationships presented in the previous figure for all three components. There is a strong relationship between the exponent and R^2, with Node 3 serving as an outlier with a lower exponent than expected for its R^2 value. The nodes furthest from the river (4, and 5) typically have the lowest of both values and the nodes closest to the river have the highest of both values.

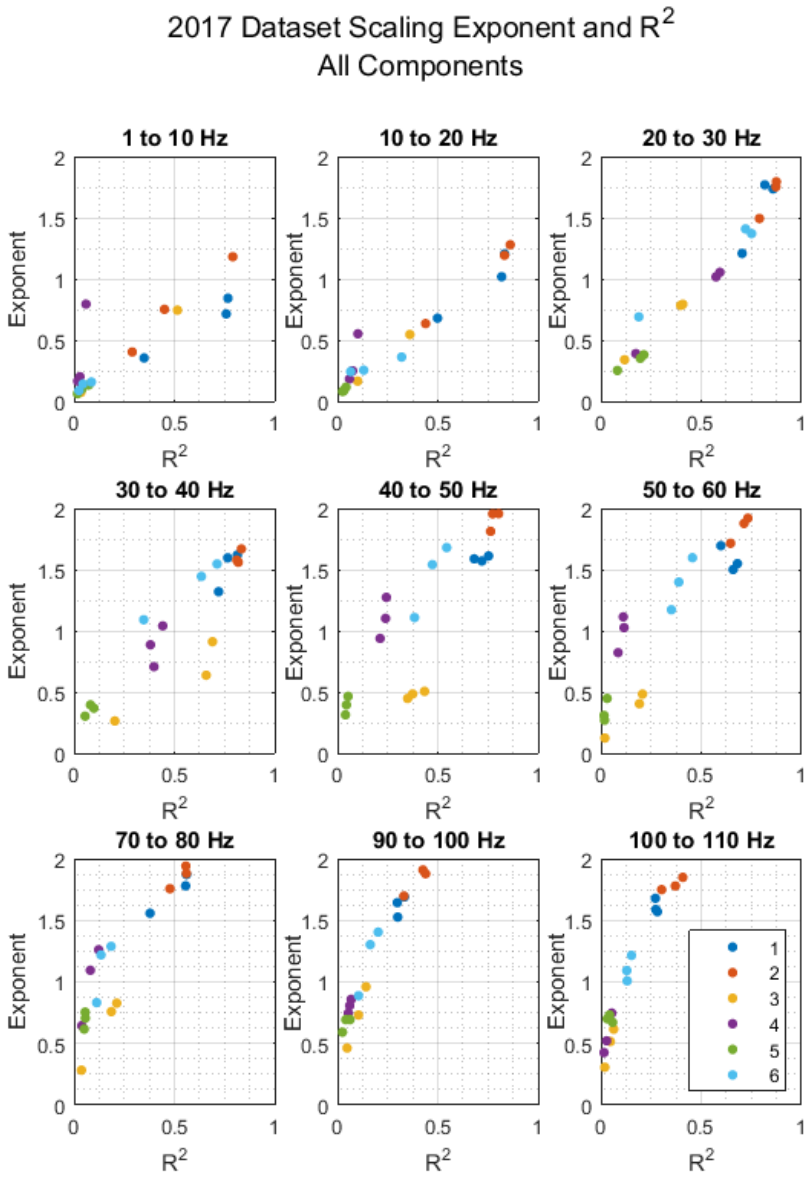

Figure 41: There is a correlation between R^2 value and scaling exponent in the frequency bins examined. Node 3 is an outlier due to the previously discussed tree interference.

The relationship between R^2 and scaling exponent is likely caused by the background noise environment. Ambient background noise will have a greater relative influence on the seismic power observed at low discharge than at high discharge. Therefore, increasing the ambient background noise will decrease the exponent of the

scaling relationship and increase the variability in the power and decrease the fit of the line. A simple synthetic example of this is presented below.

First, the raw seismic data from the N-S component for Node 1 during the first flood was selected as the sample dataset. Two separate frequency bands are considered- the 20-30 Hz band and the 90-100 Hz band. Second, noise was added to the raw data. The noise is drawn from a random-normal distribution. Seven different noise scenarios were considered, each with a logarithmically increasing standard deviation. Third, the data were processed to retrieve the five-minute mean power time series. Figure 42 shows that increasing amounts of noise progressively decreased the scaling exponent and R^2 value. The 20-30 Hz band has a high R^2 value, while the influence of precipitation in the 90-100 Hz band leads to a high degree of scatter in the relationship. Figure 41 shows the relationship between the exponent and R^2 value for the two frequency bands. For the 20-30 Hz band, the relationship is loosely logarithmic, mirroring the shape of the 20-30 Hz band shown in Figure 43. The 90-100 Hz band is linear and occurs at lower R^2 values, also mirroring the relationship shown in Figure 41.

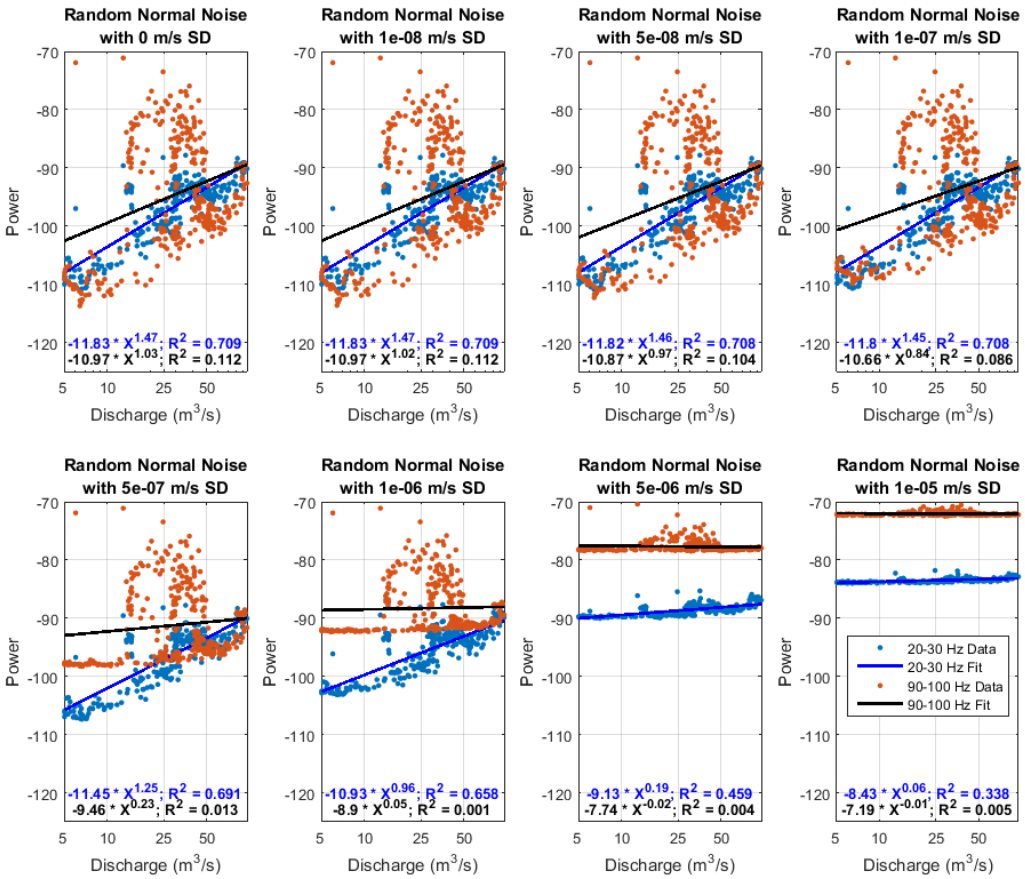

Figure 42: The raw seismic data has noise from a random normal distribution added incrementally, with a logarithmically increasing standard deviation. The five-minute mean power in the 20-30 Hz frequency band (blue markers) and 90-100 Hz band (orange markers) is shown for the 8 noise scenarios. With increasing added noise, the R^2 and slope decrease.

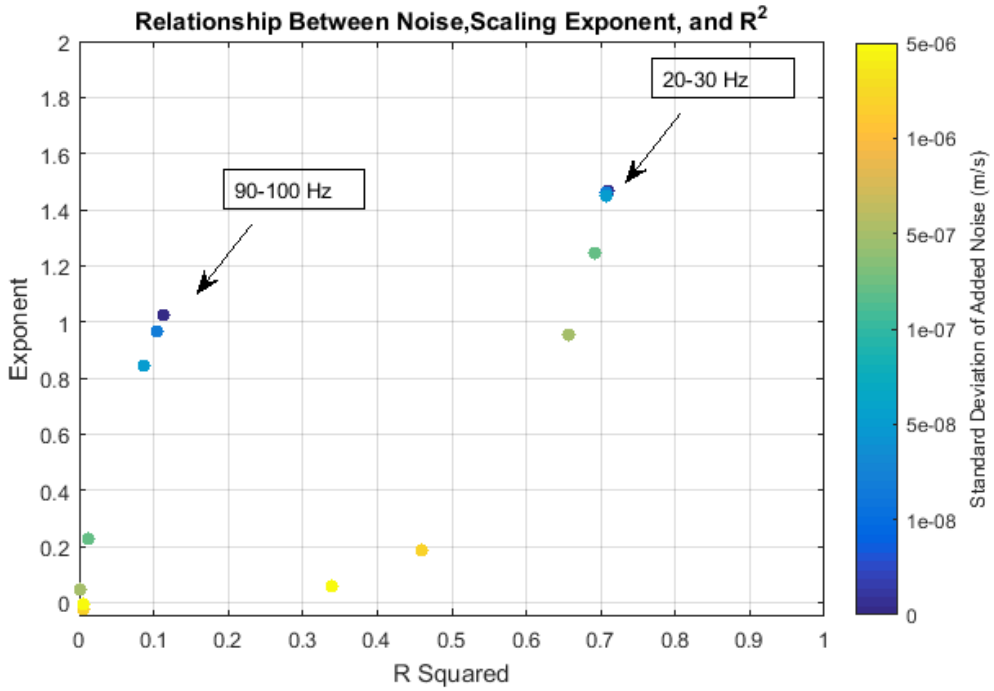

Figure 43: As the standard deviation of the added noise increases, the R^2 and Exponent

The above synthetic example demonstrates how background noise from anthropogenic or other noise sources affects the scaling relationship between discharge and seismic power. The results suggest that comparisons of this scaling exponent among different study sites must consider noise sources in their interpretation. Stations further from the river will have a lower fluvial signal to noise ratio, which decreases the exponent and R^2 value.

Basal Shear Stress

Basal shear stress in a river is often used as a measure of the stream's ability to transport material. As discussed earlier, shear stress (and shear velocity) is also related to the turbulence-driven fluctuations in the three-component velocity stream timeseries at the river bed. Basal shear stress will take into account the variations in energy gradient and river depth at a given discharge, making it a better unit of comparison

between river systems than the discharge alone. The calculation of maximum basal shear stress is dependent on the slope of the energy gradient. However, during most fluvial-seismic studies to date, a single value of river slope is used (e.g. Gimbert et al., 2014). As detailed in an earlier section, in the urbanized and rapidly-varying Northwest Branch, the river slope varies with stage.

For fluvial-seismic evaluation, it is assumed that a near-stream seismometer observes the flow dynamics within the river section closest to it. It is also assumed that the maximum basal shear stress will contribute most to the seismic signal. Therefore, the maximum basal shear stress in a cross section is used for comparison to the seismic signal. The appropriateness of this assumption will be explored in the discussion section.

In Figure 44, the seismic power is plotted against maximum basal shear stress using three different slope values. The first slope is using the entire reach slope (0 to 85 m) from 2018, which decreases at high discharge. The second slope uses a single value of 0.005, which is the high-discharge slope and a slope that is observed from an elevation profiles of LiDAR data at the study reach. The third slope is using the upstream (0 to 55 m) or downstream (55 to 85m) energy gradient using the discharge-energy gradient relationship presented in an earlier section. The maximum depth at each cross section during each five minute interval and the energy gradient during each five-minute interval is used to calculate basal shear stress. The North-South component of all five nodes along the river are displayed in the figure in order of their arrangement along the stream. Nodes 1, 2, and 7 are in the upstream section, while nodes 3 and 8 are in the downstream section.

The results show that seismic power corresponds least well with the total slope for Nodes 1 and 2, confirming that the slope decreases at high discharge do not influence the basal shear stress at the upstream node sites. There is a high degree of variability in the Node 7 data, the reason for which is not clear. As shown previously, the data for Node 3 is affected by the resonant vibrations of in-stream trees, which may explain the apparent decrease in seismic power at high shear stress.

In the upstream study segment, the scaling relationship between the shear stress and seismic power is much greater using a single value for slope, since in this scenario shear stress is only a function of river stage. Because of the high constant slope used, the shear stresses for low discharge using this method are an overestimation. Using the river slope that varies with stage (third column in Fig. 42), the scaling exponent is much lower for the upper segment, since basal shear stress increases more rapidly with increasing seismic power.

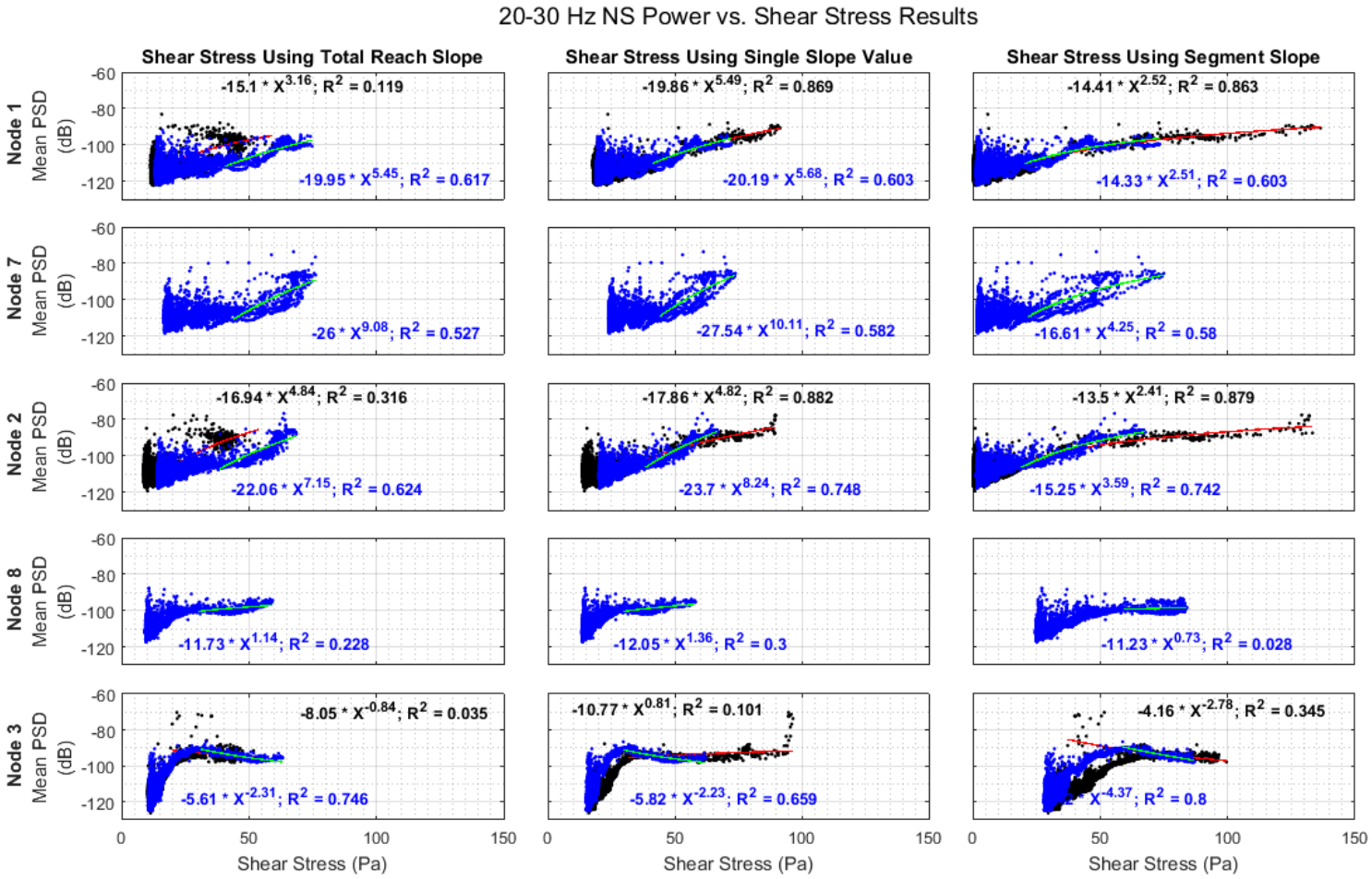

Figure 44: The relationship between maximum basal shear stress in the closest stream cross section and seismic power for the five along-stream nodes. The nodes are shown in order of placement from upstream to downstream. Blue symbols indicate data collected during the 2018 study period; black symbols indicate the 2017 study period. The first column uses the water surface slope from 0 to 85 meters downstream, the second uses a single value of slope, and the third uses the water surface slope for the closest river segment.

Relationship of U/U*

In fluvial hydraulics, the ratio of the average channel velocity to the shear velocity U/U*, is a measure of the flow resistance or hydraulic smoothness of the flow. In the study reach, cross section values of U/U* increase nearly linearly with discharge and U/U* is generally lower in the rougher and steeper downstream stream segment (nodes 3 and 8) than in the upper stream segment (nodes 1, 2, and 7). In the upstream river segment, the scaling exponents increase if the local energy gradient is used rather than a single reach slope value, since the effect of an increasing slope will be to reduce the U/U* ratio, particularly at high discharge. Figure 45 shows the relationship between North-South component seismic power and U/U*, arranged in order from upstream to downstream. The R^2 values are relatively insensitive to the slope value used to calculate U/U*.

Stream Power

Stream power is a measure of the rate at which a stream's potential energy is lost to dissipated forms. The relationship between north-south component stream power and seismic power is shown in Figure 46. In Nodes 1 and 2, taking into account the increases in energy gradient with discharge, there is slightly greater seismic power excited at high stream power than predicted by a linear relationship ($P \; \alpha \; \omega^{1.39-2.25}$).

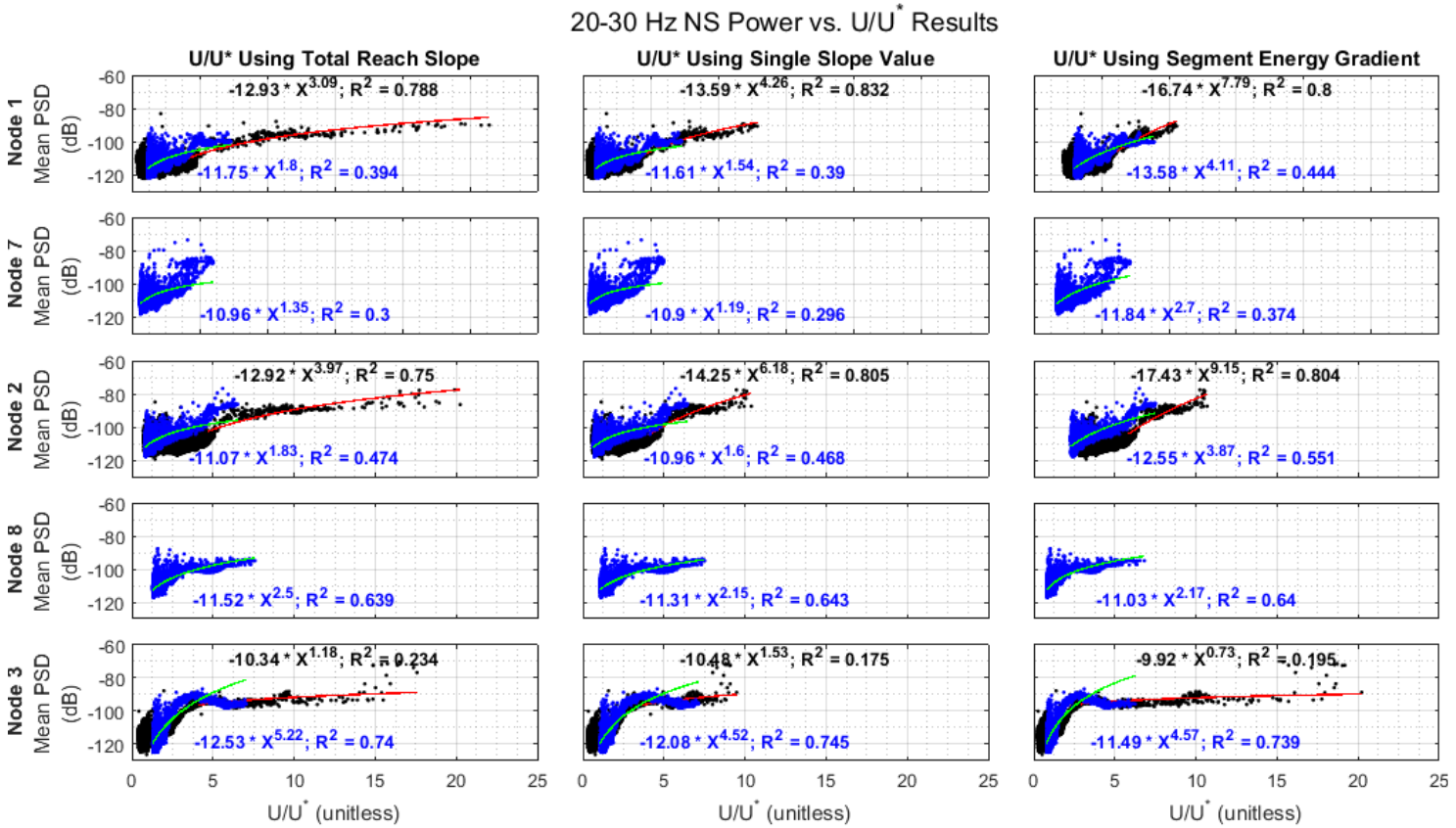

Figure 45: The relationship between U/U* in the closest stream cross section and seismic power for the five along-stream nodes. The nodes are shown in order of placement from upstream to downstream. Blue symbols indicate data collected during the 2018 study period; black symbols indicate the 2017 study period. The first column uses the water surface slope from 0 to 85 meters downstream, the second uses a single value of slope, and the third uses the water surface slope for the closest river segment.

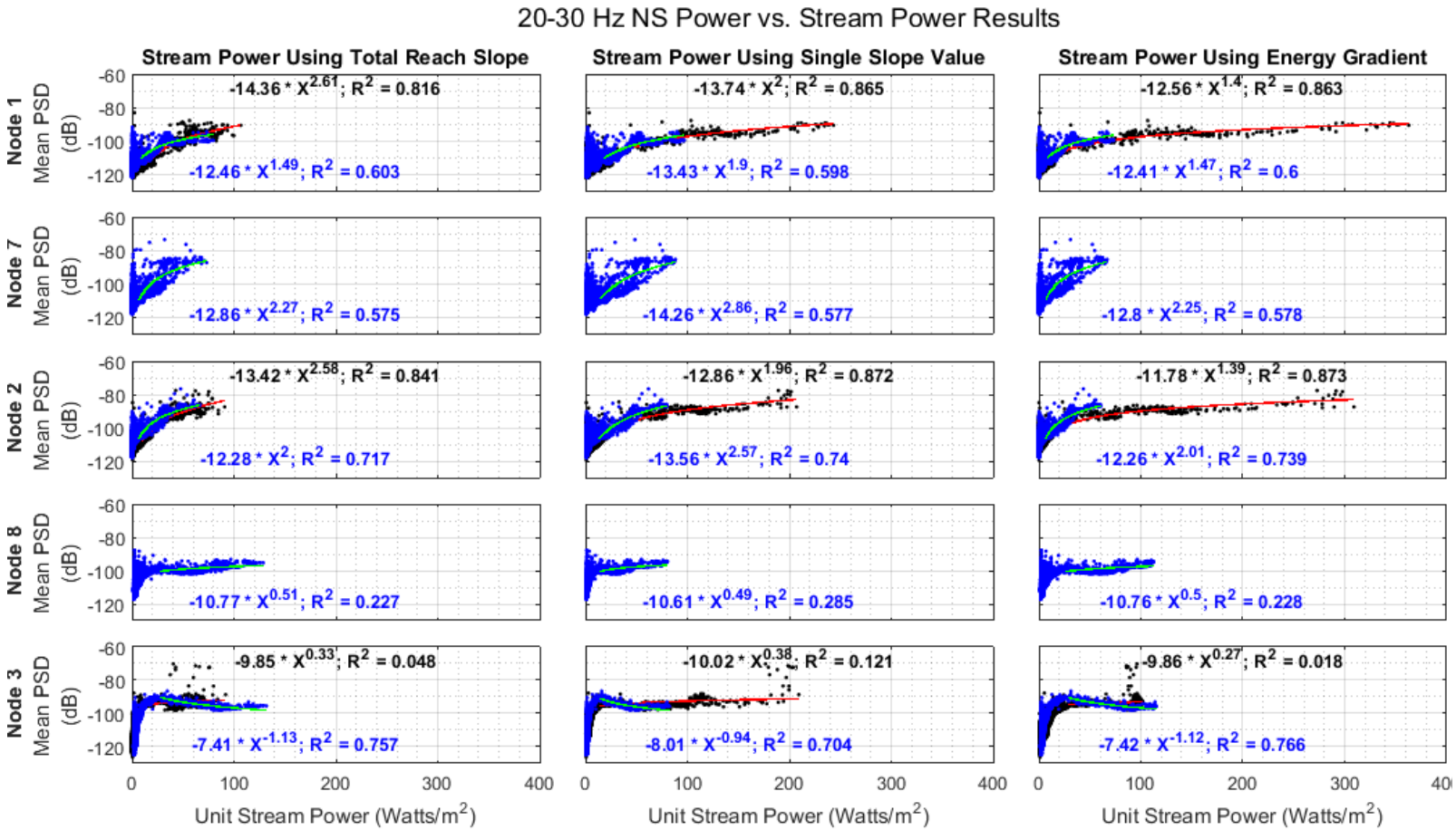

Figure 46: The relationship between unit stream power in the closest stream cross section and seismic power for the five along-stream nodes. The nodes are shown in order of placement from upstream to downstream. Blue symbols indicate data collected during the 2018 study period; black symbols indicate the 2017 study period. The first column uses the water surface slope from 0 to 85 meters downstream, the second uses a single value of slope, and the third uses the water surface slope for the closest river segment.

Applying FDPA to Node Data

To identify whether the polarization metrics used on the Oroville Dam dataset are suitable for characterizing fluvial energy at the river reach scale, FDPA was applied to the three-component nodal data as described in Chapter 2. To limit the influence of wind and rain signals within the data, FDPA was used to examine the signal polarization during the falling limb of flood hydrographs, when significant rainfall has ceased but river flow is elevated. The distribution of FDPA polarization metrics are used to characterize the signal. The FDPA results are calculated in five-minute intervals, then all the five-minute results are accumulated into a four hour period to create the histograms presented in this section. The first flood hydrograph presented in Figure 48, as it provides the largest discharge observations of the entire study. Additional histograms of FDPA results during the baseflow control period and other floods are shown in Appendix I. The analysis is limited to the 1 Hz to 50 Hz frequency band.

One difference between the application of FDPA presented in Chapter 2 and at the Northwest Branch study reach is that 5 minute intervals are used instead of hour-long windows. Because the method divides each interval into 19 subwindows, a 1 Hz oscillation will have approximately 15 cycles in each subwindow. Uncertainty over whether or not this was sufficient to characterize the signal polarization prompted a repeat analysis of the same 4 hour time period on the falling limb of the largest flood hydrograph using time windows of 5, 15, and 30 minutes. The results, presented in Appendix J are nearly identical, suggesting that a five minute time window is sufficient.

FDPA Results

The FDPA directional analysis shown in Figure 47 reveals that at most frequencies the observed degree of polarization is not high enough ($\beta^2 \ngeq 0.5$) for interpretation, even when river discharge is elevated. Below, all instances of repeated interpretable values of β^2 are discussed by node. As noted in Chapter 2, the azimuth (Θ_H) is only interpretable if ϕ_{vh} is 20° away from ± 90°, since the azimuth of horizontal circular motion is not defined.

Nodes 1 and 2 have similar FDPA results. Both contains a single peak in β^2 at 18 Hz-20Hz during the flood events, however this peak is also present during the control period (Appendix I). The characteristics of this peak are consistent across all examined time periods. The ϕ_{hh} is 0°, the ϕ_{vh} is broadly distributed, Θ_V is 90° from the vertical. The azimuth is interpretable and occurs 50° or 230° from north for Node 1 and 30° or 210° from north for Node 2.

Node 3 has a much higher and more narrowly-distributed β^2 at discrete frequency bands below 5 Hz, at 15 Hz, 22 Hz, and 30 Hz. Above 30 Hz, the β^2 is also greater than 0.5, although is broadly distributed. The focused high β^2 intervals below 30 Hz are not present in the control period, while the broadly distributed distribution above 30 Hz is present in the control period. The highly focused and polarized bands below 30 Hz have a ϕ_{hh} near 0°, broadly distributed ϕ_{vh}, and Θ_V near 90°. Below 5 Hz, the azimuth is 10°/190° from north, while between 15-30 Hz the azimuth is 50°/230° from north. These results are consistent with the discrete bands observed in spectrograms at this node and the interference of the in-stream fallen trees that have an influence during high river stage.

Node 4 has an increased β^2 from 25 to 35 Hz, which is only present during the first node deployment and is consistent during both flood and non-flood time periods. A further investigation of the results from the instrument deployed during the first time interval reveal that the vertical component was likely malfunctioning throughout the first deployment, with impacts on the FDPA results and H/V results discussed later. This same instrument (Serial Number 2527) was also deployed as Node 3 during the third deployment. This behavior is documented in Appendix K. For flood 12, the largest 2017 flood outside of the 1st deployment, the β^2only approaches 0.5 near 18 Hz. At this frequency, the ϕ_{hh} is near 0°, $\phi_{vh}$is broadly distributes, Θ_V is near 90°, and the Θ_H is 90° or 270°.

Node 5 has increased β^2 above 0.5 at 25 Hz in Floods 1 and 2, but not during the control period or other floods examined. For these floods, ϕ_{hh} is slightly more concentrated near -180°, is broadly distributed in ϕ_{vh} and Θ_V, and has an azimuth of 315°/135°.

Node 6 consistently has two peaks which approach a β^2 of 0.5 occuring at 35 Hz and 45 Hz. The peak at 35 Hz is also present during the control period. The 35 Hz peak has linear horizontal motion (ϕ_{hh} is -180°, ϕ_{vh} is broadly distributed, Θ_V is 90° from the vertical, and the azimuth is tightly focused at 305°/135° from north.

The FDPA results described above are very unlike the Oroville Dam FDPA results presented in Chapter 2. The broadly distributed ϕ_{vh} for all nodes except node 3 suggests that the close river-to-station distance and distributed seismic source precludes coherent Rayleigh-like wave motion reaching the stations, even farther away from the river in nodes 4 and 5. A consistent signal containing Θ_V 90° from the vertical and a

ϕ_{hh} of 0° at distinct frequency peaks around 20 Hz even when the river is not flowing suggests a high amount of seismic power in the horizontal component. Node 3 contains the most focused and consistent FDPA results, though these results are likely the influence of the vibrating in-stream trees causing horizontally-polarized signal.

H/V Spectral Ratio

A possible control on the observed persistent FDPA characteristics is resonance of trapped surface waves between the surface and shallow bedrock. If there is a significant impedance contrast between the floodplain material and underlying bedrock, then waves will become trapped, with a resonant frequency related to the depth of the surficial material. The horizontal-to-vertical spectral ratio (H/V) is a well-known indicator of local site resonance and is widely used in geotechnical and engineering applications (e.g. Bonnefoy-Claudet et al., 2006). Recently, Anthony et al. (2018) identified local site resonance in seismic data during a fluvial seismic study. The authors found two frequency bands that formed peaks in H/V spectrograms: 0.33-2 Hz and 12-22 Hz. The upper frequency band was identified as most likely due to local site resonance while the lower frequency band was attributed to macroturbulent eddies generating pressure fluctuations along the banks and affecting the horizontal components in this way.

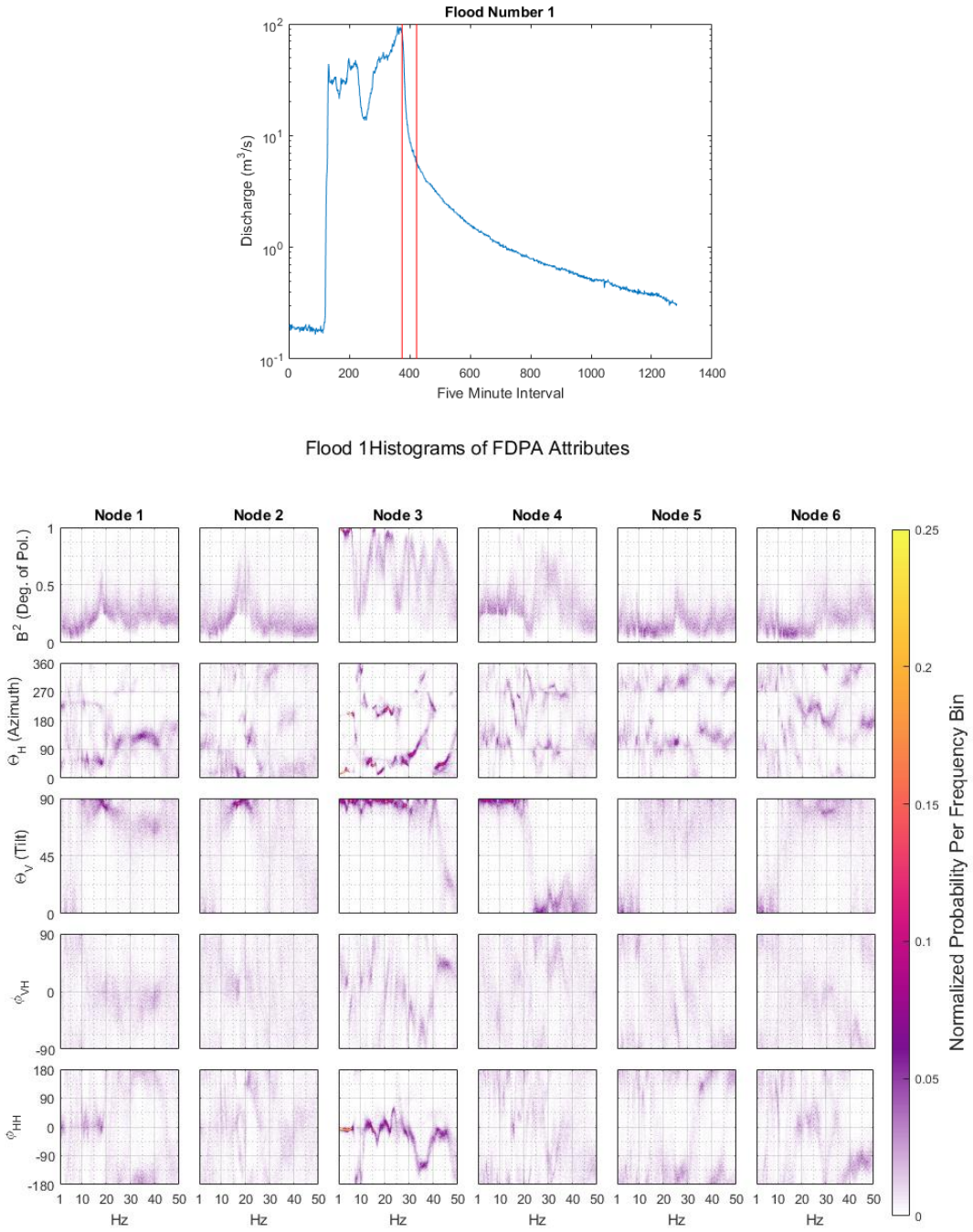

Figure 47: Top panel- Flood hydrograph for Flood 1. The area between the red vertical lines indicates the interval analyzed using FDPA. Bottom panel- FPDA results for all six nodes deployed in 2017. The degree of polarization ($\boldsymbol{\beta^2}$), horizontal azimuth from north ($\boldsymbol{\Theta_H}$), angle from the vertical ($\boldsymbol{\Theta_V}$), vertical-horizontal phase difference ($\boldsymbol{\phi_{vh}}$), and horizontal-horizontal phase difference ($\boldsymbol{\phi_{hh}}$) are presented in normalized histograms so that at each frequency, the probability sums to one.

Following Anthony et al. (2018) we calculate the H/V ratio during the control period and during several flood events to determine if this a control on the FDPA results. The vertical power spectral density is the same presented in earlier sections, in decibel units. The horizontal power spectral density used in this calculation is the sum of the power in the two horizontal components, taking care to transform to linear units and back in order to do the addition. The H/V ratio for all six nodes for the first flood is shown in Figure 48. The H/V ratios for the denser node network in 2018 is shown in Figure 49 for the first week of deployment, which contains two flood periods.

During the first flood, in Nodes 1 and 2, there is a persistent H/V peak centered on 20 Hz. This peak broadens during the highest discharge, though remains centered on the same frequency. In Node 3, bands of high H/V at high discharge are consistent with the vibration of the fallen trees adjacent to the node. The resonant vibrations have a greater effect on the horizontal components, leading to increased H/V ratios. At low discharge, there is no 20 Hz peak in H/V ratio in Node 3. In Node 4, from 20-30 Hz, there are unusually high H/V ratios, except when disrupted by heavy precipitation events. This behavior is observed only during the first deployment, and appears to be caused by instrument malfunction in the vertical component of the node deployed here (see Appendix K for additional discussion of the faulty node). Node 5 does not have any peaks in H/V ratio, even during high discharge. Node 6 has a weak peak at 35 Hz during the falling limb of flood 1. At a discharge above 50 m^3/s, an H/V peak develops between 20 and 30 Hz.

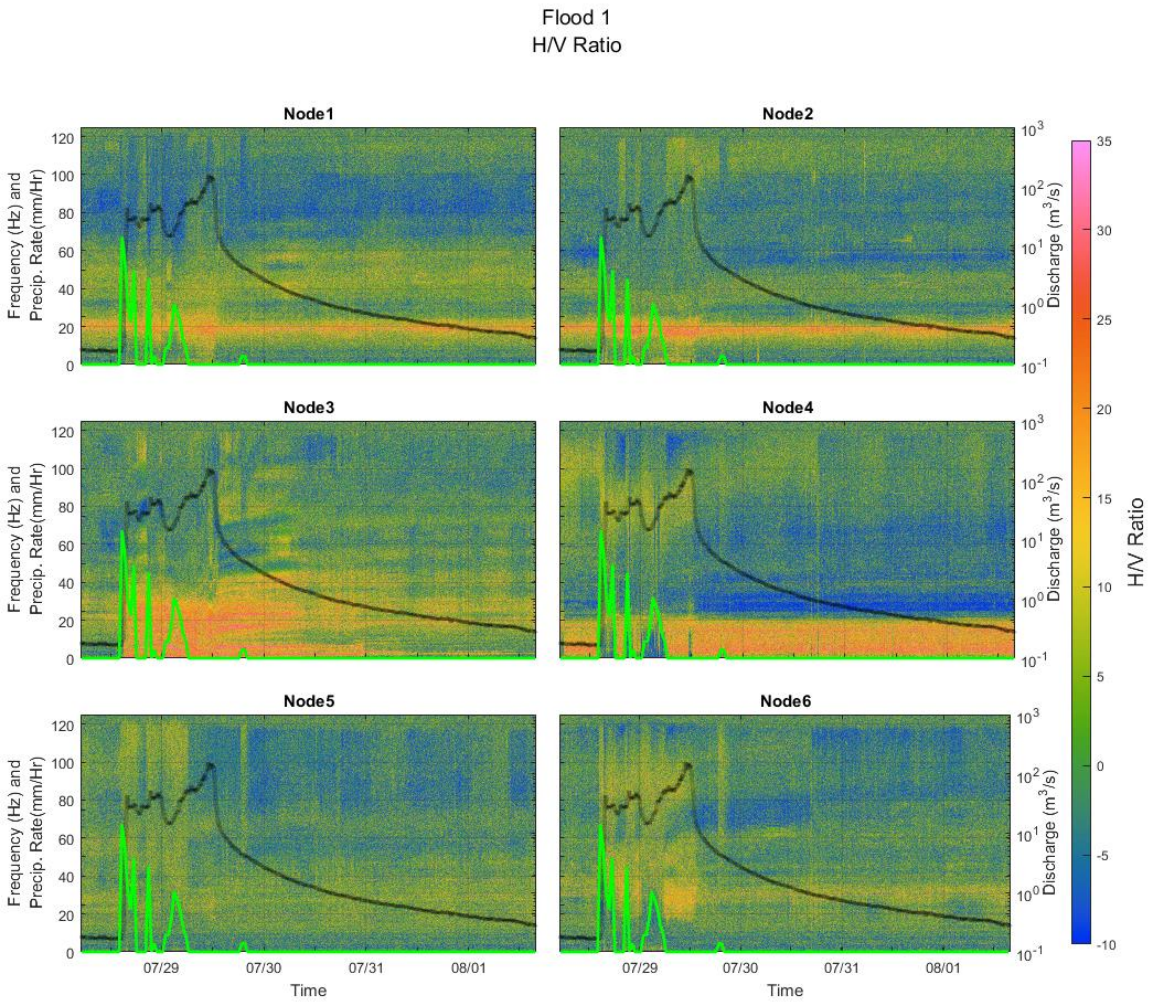

Figure 48: H/V spectral ratios for six nodes deployed during the first flood. The black line displays the river discharge, the green line shows the precipitation rate reported by a nearby weather station. Node 3 is affected by fallen streams protruding into the stream. Node 4 has a faulty vertical component during this interval.

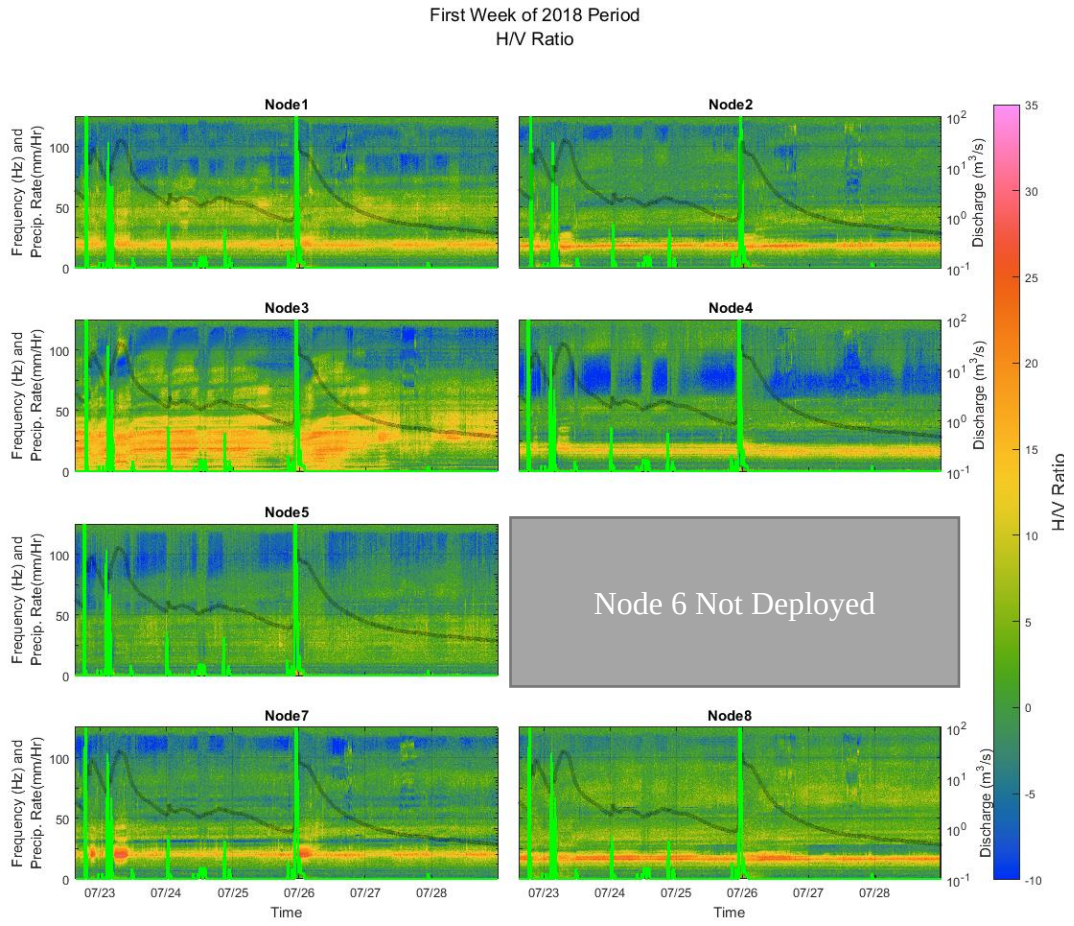

Figure 49: H/V Spectral ratio for the first week of the 2018 study period, which includes the highest discharge recorded in 2018. Consistent H/V peaks are observed around 20 Hz for Nodes 1,2,4,7, and 8. Node 3 is affected by trees vibrating in the stream. The black line indicates the discharge and the green line indicates the precipitation rate.

The observed H/V peaks in nodes 1 and 2 to can be used estimate the depth to the bedrock interface, assuming a simple two-layer system where lower impedance soil lies above higher impedance shallow bedrock. The soil thickness, Z, is given by

$$f = \frac{V_S}{4Z} \tag{27}$$

where f is the resonant frequency, Vs is the soil shear velocity. A shear wave velocity of soil of 137 m/s was used by Anthony et al. (2018) for silty-clay, which is similar to the fine grained floodplain in which the nodes were buried. A calculated sediment

thickness of 1.7 meters for 20 Hz is reasonable considering this is approximately the bank height and the river bed has eroded nearly to the bedrock.

Discussion

In this study, we applied fluvial seismic techniques to an urbanized stream for the first time, with the intent of characterizing changes in fluvial energy dissipation at the river reach scale under rapidly changing and intense flood events. Despite the uniform cobble-run river reach selected for the study, observations of the energy gradient suggest that in the upstream section of the study reach, the energy gradient steepens with discharge while in the steeper downstream portion of the study reach, the energy gradient decreases with increasing discharge. This observation of differential energy gradient behavior is consistent with the "shear stress reversal" hypothesis put forward for alluvial riffle-pool sequences (i.e. Wilkinson et al., 2004). In this hypothesis, channel riffle pool morphology is maintained by the maximum shear stresses in steeper riffle sequences occurring at lower discharge, while maximum shear stresses occur in flatter pool sequences occur at higher discharge. For the highest observed flows at the Northwest branch study reach, a shear stress, stream power, and U/U* reversal is expected.

Seismometers were placed along the upstream and downstream portions of the study reach. The upstream seismometers (Nodes 1, 2, and 7) showed a greater responsiveness in horizontal component to the discharge than two downstream seismometers (Node 3 and 8). However, the downstream nodes are influenced by resonant vibrations from a tree lying in the stream, limiting the ability of this dataset to

conclusively test whether or not seismic data is able to monitor differential dynamics in the upstream and downstream reaches.

Uncertainty in the hydrologic data used in the study is present from several sources. The discharge values are derived by simulating a rating curve with USGS gauges upstream and downstream of the reach. Due to changes in the pressure transducer position between the 2017 and 2018 study intervals and the potential for changes in channel morphology upstream of the study reach due to construction activities, two different simulated rating curves were constructed for the time intervals. The reliance on a single channel bed elevation model from survey data results in the assumption that the channel form is unchanged throughout the study. Repeated site visits show that the eastern floodplain of the Northwest branch was affected by construction during the 2018 interval, though the channel itself was unaffected.

In this study, the approximation is made that the pressure transducers accurately represent the flow depth through measurement of the hydrostatic pressure. At high flow velocities, the hydrostatic pressure and result in an underestimation of flow depth. However, since the pressure transducers were deployed near the bed and towards the edge of the channel, this effect is not likely to be significant.

In this study, no clear hysteresis in the discharge-seismic power is observed in flood events during the selected time intervals. Estimates of the basal shear stress and grains size distributions in the study reach suggest that in the downstream portion of the reach, the maximum shear stresses slightly exceed that needed to move the D_{84} grain size, such that bed breakup conditions could occur in the downstream portion of the reach. From the water surface slope observed in the study reach, there is not a

hysteresis between discharge and shear stress in the study reach, though a hysteresis in bedload transport could occur. Particle clustering or imbrication of clasts sometimes leads to a higher critical shear stress for transport on the rising limb of the hydrograph than a critical shear stress for deposition on the falling limb of the hydrograph. Many studies have inferred the presence of bedload transport signals on the basis of hysteresis in the discharge-seismic power relationship by this mechanism. This hysteresis is observed in varied setting such as the Trisuli River in Nepal (Burtain et al., 2008), Cho-Shui River in Taiwan (Hsu, Finnegan, and Brodsky, 2011) and Erlenbach in Germany (Roth et al., 2014, Roth et al., 2016, Roth et al., 2017), and upper Koulbic river in Luxemburg (Barriere et al., 2015). Many of these study rivers are steeper than the Northwest Branch or are snowmelt streams. Hysteresis is not observed in some other studies, including the steeper and smaller South Fork of the Cache la Poudre River (Anthony et al., 2018). Roth et al. (2017) introduced an alternative mechanism to explain hysteresis in the discharge-power relationship besides only sediment transport, whereby localized changes in boulder arrangement change the distribution of fluvial energy dissipation.

A major aim of this study was to evaluate the scaling of seismic power and metrics of energy dissipation, as described in hypothesis 2. While related to discharge, the basal shear stress, U/U* and stream power were selected because of their physical basis in turbulent energy dissipation. Each of these metrics accounts for variation in the water surface slope. For the along-stream seismometers shown in Figure 44, 45 and 46, there is equivalently high correlations in the scaling relationships between power and

discharge, basal shear stress, U/U*, and stream power. However, the scaling exponents vary for the metrics of energy dissipation depending on the slope value selected.

To place the observed scaling exponents within context, the values may be compared to that predicted by the Gimbert et al. (2014) model. Within the model, power is predicted to scale with river depth and slope to the 7/3rd power. Within the model there is also an additional scaling function at low discharge to account for a decrease in turbulent intensity when the depth approaches the roughness height of the bed layer (Gimbert et al., 2016). This function is varied at low river depths but becomes a constant as the grain roughness becomes less important and has been mostly ignored by authors interpreting fluvial-seismic results in relation to the model. Within the model, the roughness height (K_s) is defined as three times the median grain size (D_{50}) and the function becomes constant at H/ K_s ratios of approximately 20. Using the minimum cross-section D_{50} of 71 mm, H/K_s ratios of up to 9 are achieved, indicating that the simple power scaling relationships applied to the data may neglect this effect within the model (see Figure 50). Equation 33 in Gimbert et al. (2014) is reproduced below:

$$\zeta\left(\frac{H}{k_s}\right) = \left[c_{\overline{u}}(k_s)^{\frac{1}{3}} c_{\overline{u}}(X_l^r)^{\frac{4}{3}} c_\sigma^{\frac{2}{3}}\right]^2, \tag{29}$$

where $c_{\overline{u}}$ and c_σ are semiempirical formulas to account for the decreased streamwise velocity below the roughness height of the water from Lamb et al. (2008), such that

$$c_{\overline{u}}(X) = \frac{X}{0.12k_s}\left(1 - \left(\frac{X}{2k_s}\frac{k_s}{H}\right)\right) \tag{30}$$

Which describes the mean velocity as a function of depth within the roughness layer and

$$c_\sigma = 0.2\left[5.62\log_{10}\left(\frac{H}{k_s}\right) + 4\right] \quad (31)$$

which describes the peak turbulent intensity within the roughness layer, which decreases with increasing relative roughness. The behavior of this function across all submergence values is not a power function, but over the range H/K_s values from 0.5 to 9 observed during the observation period, the relationship can be approximated by a power function. As high observed H/K_s values are most important to the scaling relationships and are best fit with the power scaling, this approximation is considered a reasonable estimate. The discharge threshold of 5 m^3/s applied corresponds to an H/K_s ratio of between 2.2 and 3.7, depending on the channel cross section examined.

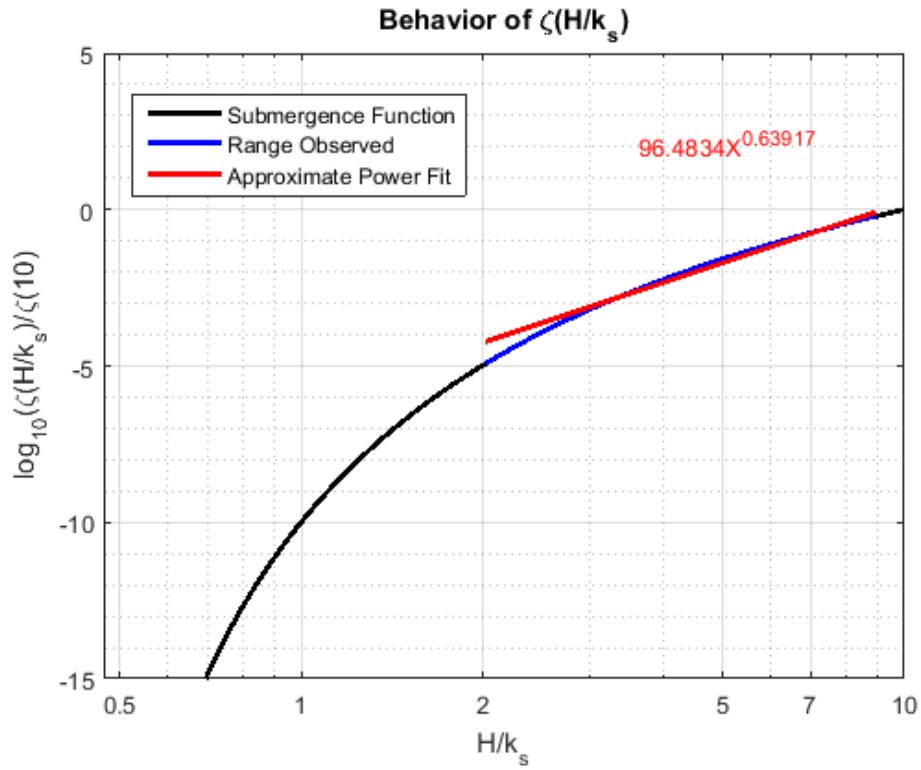

Figure 50: Approximate power scaling of a function described in Gimbert et al. (2014) that accounts for decreased turbulence intensities as the river depth (H) approaches the roughness height (K_s). The power scaling is approximated in the H/K_s range of 2-9, which represents the river discharge examined in the power scaling relationships in this study. In the best fit equation, X is H/K_s.

To summarize, in equation 43 of Gimbert et al. (2014), the total PSD of vertical component power scales as:

$$P \; \alpha \; \zeta \left(\frac{H}{K_s}\right) H^{\frac{7}{3}} \sin(\theta)^{\frac{7}{3}} \tag{32}$$

Substituting in the approximate scaling for the relative submergence function, we achieve:

$$P \; \alpha \; H^{0.639} H^{\frac{7}{3}} \sin(\theta)^{\frac{7}{3}} \tag{33}$$

The observed approximate scaling between cross-section max discharge H and discharge (Q) is H α $Q^{1/2}$ (shown in figure 32). The relationship between the energy gradient and discharge in the upper river segment is $S \; \alpha \; Q^{0.373}$ (Figure 31). Inserting these relationships is done to place this work in context with previous studies, which reported scaling with discharge.

$$P \; \alpha \; (Q^{\frac{1}{2}})^{0.639} (Q^{\frac{1}{2}})^{\frac{7}{3}} (Q^{0.373})^{\frac{7}{3}} \tag{34}$$

The result is $P \; \alpha \; Q^{1.48}$ (without considering slope) or $P \; \alpha \; Q^{2.36}$ (considering slope), which is greater than the $P \; \alpha \; Q^{7/6}$ predicted if the submergence function and slope were not taken into account.

In this study, in the upstream portion of the study reach for which the slope behavior can be represented by a power function, the scaling of power with discharge was up to $Q^{1.79}$ in the horizontal components and up to $Q^{1.49}$ in the vertical component. These exponents are similar to one study with similar river-to-distance spacing: Roth et al. (2017) who found $P \; \alpha \; Q^{1.49-1.9}$ in the 35-55 Hz band for a channel-parallel component. The exponents are lower than reported by Anthony et al. (2018) who found $P \; \alpha \; Q^{\sim 2.5}$ in the 12-22 Hz band for all components.

The proposed scaling relationships in Gimbert et al., (2014) are appropriate when the station-to-river distance is much greater than a Rayleigh wave

considered in the model. However, with the array of seismometers used in this study, it is observed that the scaling relationships decrease with distance away from the river, and that these decreases are related to decreasing fits to the regression line. This result indicates that in practice, near-field observations are less influenced by the surrounding noise environment. A simple simulation consisting of incrementally added noise demonstrates that simulated anthropogenic noise has the effect of decreasing the scaling relationships. The influence of the noise environment must therefore be considered when evaluating scaling exponents among fluvial-seismic studies.

Consistent with other studies, the greatest responsiveness to variations in river discharge is observed in the horizontal components. While some authors (Barriere et al. 2015; Schmandt et al. 2013) have suggested this indicates Love wave excitation, the H/V analyses and FDPA results in this study indicate that trapped river-excited waves in the soil and floodplain material are a likely source of horizontal component power. This result suggests that the scaling relationships are influenced by local site resonance, particularly since the 20-30 Hz frequency band used in this study partially overlaps with the H/V peak. In many fluvial-seismic studies, excited energy in specific frequency bands is interpreted to reflect a whether the source is water turbulence or bedload transport. This interpretation may be incorrect if local site resonance determines the frequency band excited by fluvial energy.

In Chapter 2 and 3, particle motion analysis was shown to effectively characterize the fluvial-seismic signal for the Oroville Dam spillway. Analysis of signals produced by the Northwest Branch of the Anacostia River indicate that the signal is not sufficiently polarized for interpretation using FDPA. This is may be due

to the short river-to-station distance, which leads to multiple sources of seismic signal and a broad distribution of the polarization attributes. This is also consistent with fluvial energy dissipation that is evenly distributed at bankfull stage. At frequencies where there is sufficient polarization for interpretation, the polarization attributes indicate a horizontally-polarized wave, which is very unlike the motion observed in the first two chapters. The motion is consistent with trapped SH waves, and is linked with the observed H/V spectral ratio peak.

Chapter 5: Synthesis and Conclusions

Synthesis

Previous fluvial-seismic research, including the work presented in Chapters 2 and 4, has focused on variations in seismic power and frequency in time at a single river site. Since the characteristics of river systems (i.e. drainage area, discharge, slope, width, velocity) span many orders of magnitude, in fluvial geomorphology it is also common to compare among fluvial settings to establish scaling relationships. To date, there have been relatively few fluvial-seismic studies with common experimental design, so no systematic examination of these studies is present in the literature. However, with recent additions to the literature and the results presented in Chapters 2 and 4, this meta-analysis may be helpful to determine if there is systematic behavior among fluvial seismic studies.

In order to present the data from disparate studies in a common figure, several decisions must be made to ensure the results are comparable. The first step in the process is to identify the controlling variables determining the observed seismic energy at each river site. These variables were determined to be the river discharge

(Q), river bed slope (S), river width (b), river-to-seismometer distance (R), and frequency range analyzed. The studies who did not provide all of these variables were excluded. The second step is to account for these variables using physics-based approach. The rate at which fluvial potential energy is expended per unit width and length of the channel is the unit stream power. The amount of energy observed by a nearby seismometer is expected to decrease as 1/R for a surface wave. Therefore, the observed seismic energy should be scaled by 1/R for comparisons among studies.

Data collection from previous studies consisted of extracting data points from referenced images that displayed the relationship between river discharge and seismic energy. The details for each study are reported in Table 5. The frequency range analyzed varies study-by-study, and in many cases results are presented for multiple frequency ranges. In this meta-analysis, the frequency range attributed by the authors to the water turbulence (not low-frequency (<1 Hz) standing waves or macroturbulence) is used. The observed seismic energy is reported amplitude, seismic

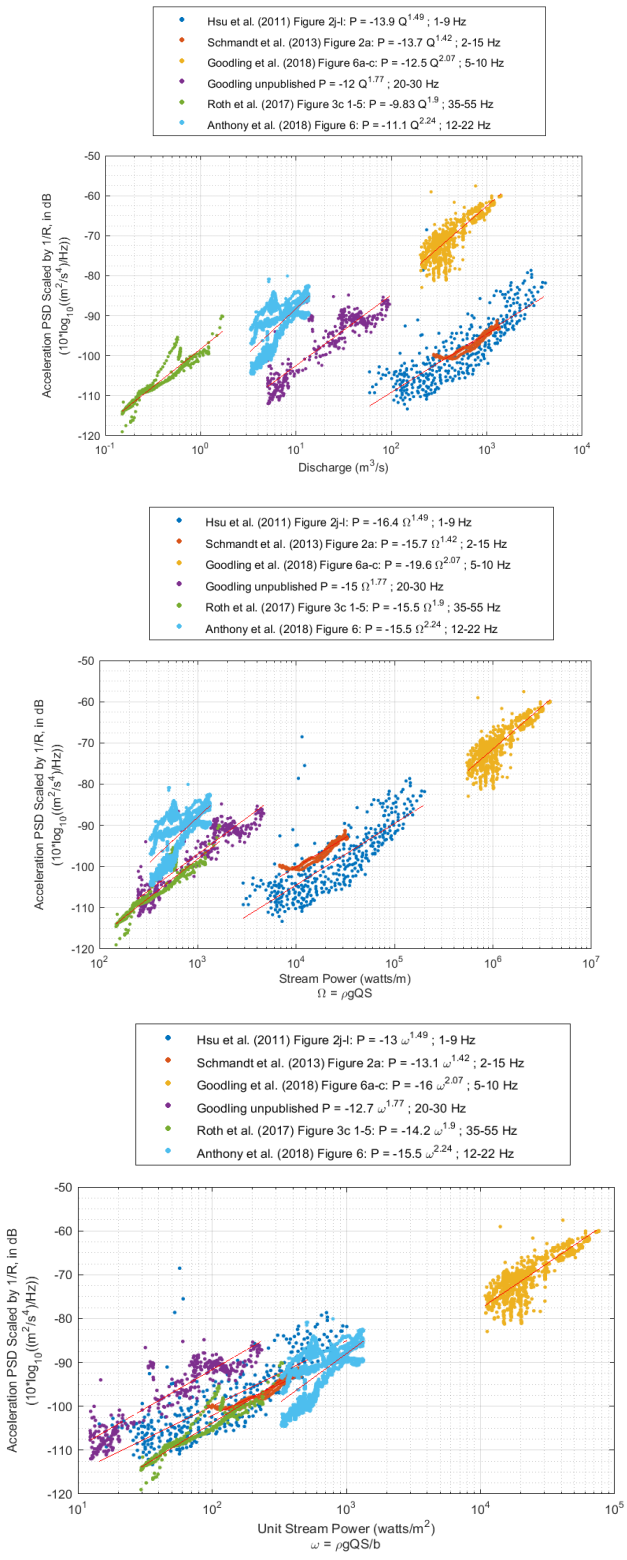

Figure 51: Fluvial-seismic data collected from six studies. The relationship between seismic power and discharge (top panel), total stream power (middle panel), and unit stream power (bottom panel) are shown.

velocity power, seismic acceleration power, and power spectral densities of both power and acceleration. When reported in other units, the seismic energy from other studies was converted to acceleration power spectral density in decibels, using $10*\log_{10}(\text{Power})$ as the definition as the decibel. In order to convert from units of amplitude to power, the amplitude was squared. Values of velocity power were multiplied by the 2*pi* mean frequency to estimate acceleration power.

The results of six fluvial-seismic studies are presented in Figure 51. The variation in observed seismic power is best explained by unit stream power (bottom panel). The six studies span nearly five orders of magnitude in unit stream power, representing large variations in discharge, slope, and width. The data for the Oroville Dam hydraulic channel has much higher unit stream power than observed in natural settings. The distance-scaled seismic power spans nearly 60 decibels, which corresponds to six orders of magnitude. This suggests that, taken all together, the scaling of unit stream power and distance-scaled power is slightly greater that a 1:1 relationship. Within each study, the scaling relationships between unit stream power and seismic power vary from 1.42 to 2.42, also suggesting greater than a 1:1 relationship. The results shown in Figure 51 suggest that despite the varied fluvial settings observed to date, the recorded seismic power from these settings may have a systematic relationship with unit stream power.

Study	Units	Goodling, Lekic, and Prestegaard (2018)	Roth et al. (2017)	Anthony et al. (2018)	Goodling (Chapter 4 this work)	Hsu et al. (2011)	Schmandt et al. (2013)
Figure Used	-	Figure 6 (Pre-Crisis Combined)	Figure 3 (All Storms Combined)	Figure 6 (All 3 Stations Combined)	Figure 39	Figure 2 (Data from 3 storm events combined)	Figure 2
River Environment	-	Hydraulic Spillway Channel	Alluvial step pool/ boulder Stream	Riffle-pool gravel bed stream	Cobble Stream	Gravel-bedded stream within a bedrock canyon	Coarse-grained sand and gravel channel within bedrock canyon
Discharge Range Analyzed	m^3/s	200-3000	0.5-2	1-17	5-95	70-4000	280-1300
River Bed Slope	%	~5% in upper portion, ~%20 in lower portion	10%	1%	0.50%	0.50%	0.25%
River Width	m	50	5	11	20	200	45-100, mean value used
Instrument Used	-	Streckeisen STS-1 Broadband Seismometer	Sercel L28 geophones	Sercel L28 geophones	Fairfield Nodal Zland 3C Geophones	Streckeisen STS-2 Broadband Seismometer	Sercel L-22 short period seismometer
River-to-Seismometer Distance	m	1770	1	1	2	50	38
Frequency Range	Hz	5-10	35 - 55	12-22	20-30	1-9	2-15
Component	-	First Eigenvector (analagous to rotation)	North-South	East-West	North-South	Vertical? (Not Specified)	Vertical
Original Seismic Units Reported	SI Units	Acceleration PSD, in dB	Ground Acceleration PSD	Velocity Power, in dB	Acceleration PSD, in dB	Amplitude	Velocity Power, in dB
Comments	-	Controlled releases; the 0.5 to 1 Hz range is originally reported	Slight Hysteresis	Flood Hydrograph	Only Data from Node 1 for the 2017 time period is used	Hysteresis Present	Controlled Release

Table 5: Summary of six fluvial-seismic studies.

Conclusions

Fluvial seismology has the potential to provide crucial information on where energy is dissipated in turbulent flow. During flood events and in remote locations, continuous data on the distribution of fluvial energy losses would allow geomorphologists to test hypotheses in how channel morphology is built and maintained. This work applied novel techniques to characterizing fluvial-seismic techniques and identified practical limitations on the scale at which fluvial-seismic information is useful. The Oroville Dam spillway provided a large-scale seismic source with steady flow rates for long intervals. The spillway channel is unlike a natural river system and, once damaged, provided an abrupt change in channel morphology that was well-suited to characterize using seismic methods. The Northwest Branch of the Anacostia River, is a far smaller system that is not as easily characterized using seismic methods. Discharge rapidly varies in the channel and the stream excites far less seismic energy, requiring seismic observations close to the stream.

In Chapters 2 and 3, particle motion analyses are shown to be effective ways to characterize the distribution of fluvial-seismic energy. Contrary to Hypothesis 1, FDPA is a superior method to IPA for characterizing the source distribution of seismic energy. This is due to the varying frequencies of the sources, which become averaged in IPA and not in FDPA. The deviation from a pure Rayleigh wave observed in both particle motion analyses is attributable to wave propagation up the hillslope at Oroville Dam. In Chapter 4, the particle motion is insufficiently polarized to be interpretable at a broad range of frequencies. The few frequencies which are polarized show polarization attributes consistent with strong horizontal component motion. The H/V spectral ratio reveals that shallow layer resonance of trapped SH waves is likely contaminating the

FDPA results at these frequencies. These results suggest FDPA is not well suited to stream-adjacent seismic observations.

Chapter 2 identified a large increase in excited seismic energy when the spillway channel is damaged, suggesting the ability of seismic observations to identify areas of greater fluvial energy dissipation. In Chapter 4, a river reach was identified that contained a different behavior during flood events. In the upstream segment, the energy gradient (and driving forces) increased uniformly with increasing stage. In the downstream segment, the energy gradient increased and then decreased with stage. Seismometers were placed along the stream in both the upstream and downstream segments, however, the downstream seismometers were compromised by the resonant vibrations of a fallen tree. This interference suggests the high influence of localized features in reach-scale fluvial-seismic studies.

Chapter 4 also considered the effect of anthropogenic daily noise oscillations- likely related to traffic noise- on the scaling relationships currently used to compare among fluvial-seismic studies. Seismometers placed further away from the stream in a perpendicular array were found to have a lower power-discharge scaling exponent, an effect that was recreated by decreasing the signal-noise ratio. This illustration highlights the need in fluvial-seismology to consider the noise environment when comparing observed scaling relationships to models or other studies.

Far from solving all practical and analytical challenges, this thesis provides motivation for additional work to bring fluvial-seismology towards use in applied geomorphology and hydraulic engineering.

Future Work

Future research should focus on the applicability of particle-motion analyses such as FDPA to fluvial seismology in natural environments. Datasets collected by previous authors (e.g. Burtin et al. (2008), Schmandt et al. (2013), Hsu et al. (2011)) using broadband seismic instruments to monitor large rivers from tens to hundreds of meters away would be an intermediate scale to what is presented in this thesis. These analyses could assess the dominant wave type excited (i.e. Love and Rayleigh) and help identify where seismic energy is excited most in the river. It is an unresolved issue in fluvial seismology that interpretations of flow dynamics assume the river section closest to the seismometer is monitored.

In the future, fluvial seismic observations should be paired with observations of energy gradient to more closely relate basal shear stress to seismic observations. Independent observations of flow turbulence and flow velocity should be included, if possible. One possible technology that could provide this information across a channel during extreme events is particle image velocimetry (for flow observations during the day). Comparing river surface velocities and turbulent intensities with seismic observations would strengthen interpretations of seismic data.

Appendices

Appendix A: Chapter 2 Supplemental Materials

Lidar Acquisition and Processing

LiDAR data were provided by the California Department of Water Resources (CADWR) following an information request on June 30th, 2017. The raw data is provided below with CADWR permission granted 10/19/2017.

November 10th and 11th LiDAR Acquisition: The LiDAR survey was accomplished using an Optech Orion M300 LiDAR system operating from a fixed wing aircraft (Cessna 310 Tail # N7516Q). The mission was completed over two days (November

10 and 11, 2015). A Trimble R8-3 GPS receiver was set up and operating at the Oroville Municipal Airport for the duration of the mission, recording data at 2 Hz.

The March 23rd merged LiDAR dataset provided by the California Department of Water Resources consists of the following datasets. From the metadata associated with the files and information provided by the CADWR, the main spillway damage area surveyed on February 27th and 28th.

- Towill, Inc. 2/24/2017 LiDAR (Additional metadata in file included in .zip file folder)

Oroville_Spillway_02
-24-2017_Project_Me

- CADWR 2/27/2017 Drone Point Cloud (Gated Spillway with no water)
- Towill Inc. 2/28/2017 LiDAR (Additional metadata in file included in .zip file folder)

Oroville_Spillway_02
-28-2017_Project_Me

- CADWR 3/13/2017 Drone Point Cloud (DF1223 upper spillway)
- CADWR 3/19/2017 Drone Point Cloud (DF1300 spoils near Hyatt Powerplant)
- CADWR 3/19/2017 Drone Point Cloud (DF1151 spoils on hillside near auxiliary spillway)

The surveys were conducted with horizontal control in California Coordinate System (CCS) State Plan Zone II (US Feet) and vertical control in North American Vertical Datum (NAVD) 1988 (US Feet).

The raw data is available file included in .zip file folder:

20170323_Oroville_LiDAR.TXT

20151111_Oroville_LiDAR.txt

In this data, the first column is the easting, the second column is the northing, and the third column is vertical elevation (all in US feet). To create a difference map, a triangle irregular network (TIN) was created from each point dataset. Using nearest neighbor interpolation, a 1-meter resolution digital elevation model (DEM) was created. A difference raster dataset was created by subtracting the 2015 DEM from the 2017 DEM, and converting the result to meters. The volume change in the main

spillway damage zone is the sum of each cell's volume (cell area x vertical change). All processing was completed in ArcMap 10.4 (ESRI).

Polarization Attributes

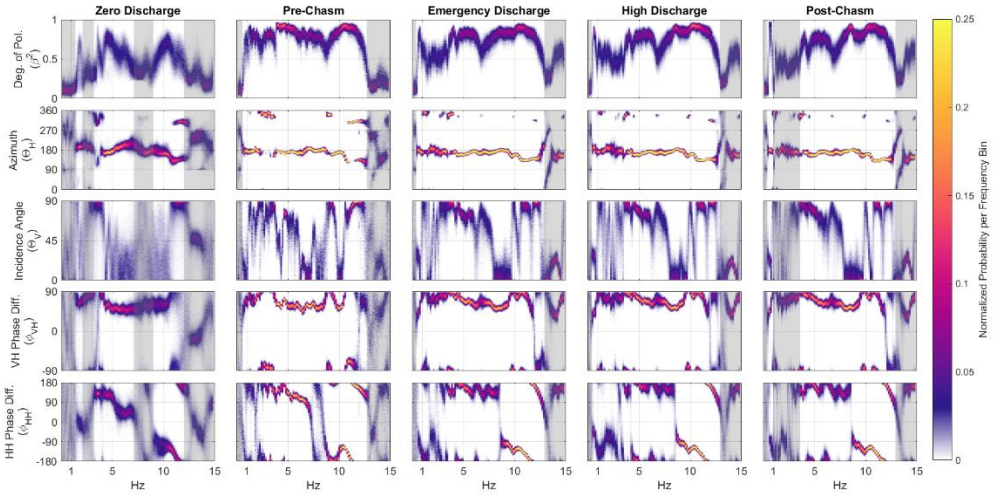

Figure S1- The four polarization attributes and degree of polarization (β^2) for the five time periods of interest. Grey shading indicates frequencies at which the polarization attributes are not interpretable ($\beta^2 < 0.5$). The Azimuth (θ_H) and vertical-horizontal phase difference (ϕ_{vh}) are shown in Figure 7 of the main text.

Scaling of Dominant Eigenvector Power and Discharge

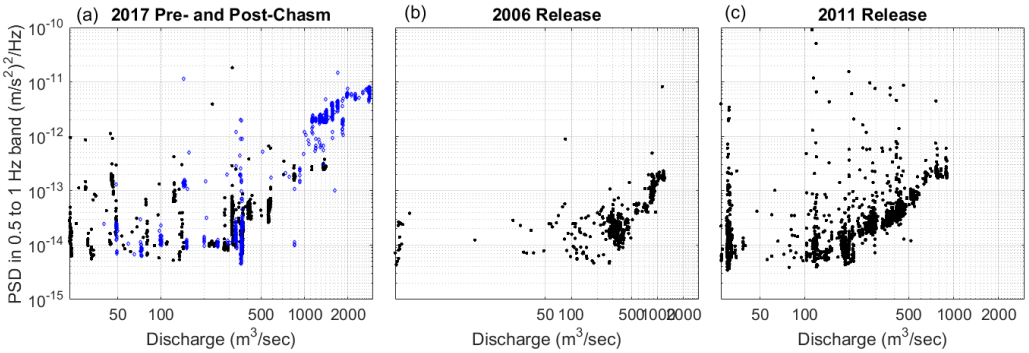

Figure S2- The hourly relationship between dominant eigenvector power and discharge has an apparent break in slope at approximately 200 cubic meters per second of discharge. We interpret this to be the

threshold for which the seismometer is sensitive to flood control spillway discharge, and complete the scaling analysis in the main text only for hours with discharge greater than 200 cubic meters per second.

SPECFEM2D Simulation

Topographic model domain for the SPECFEM2D simulation was created by extracting the elevation profile along a transect extending through the BK ORV seismometer and the center of the Oroville Dam Spillway. To create the model domain, 1000 meters were added to the lowest elevation, so that the model boundary did not interfere with the topography.

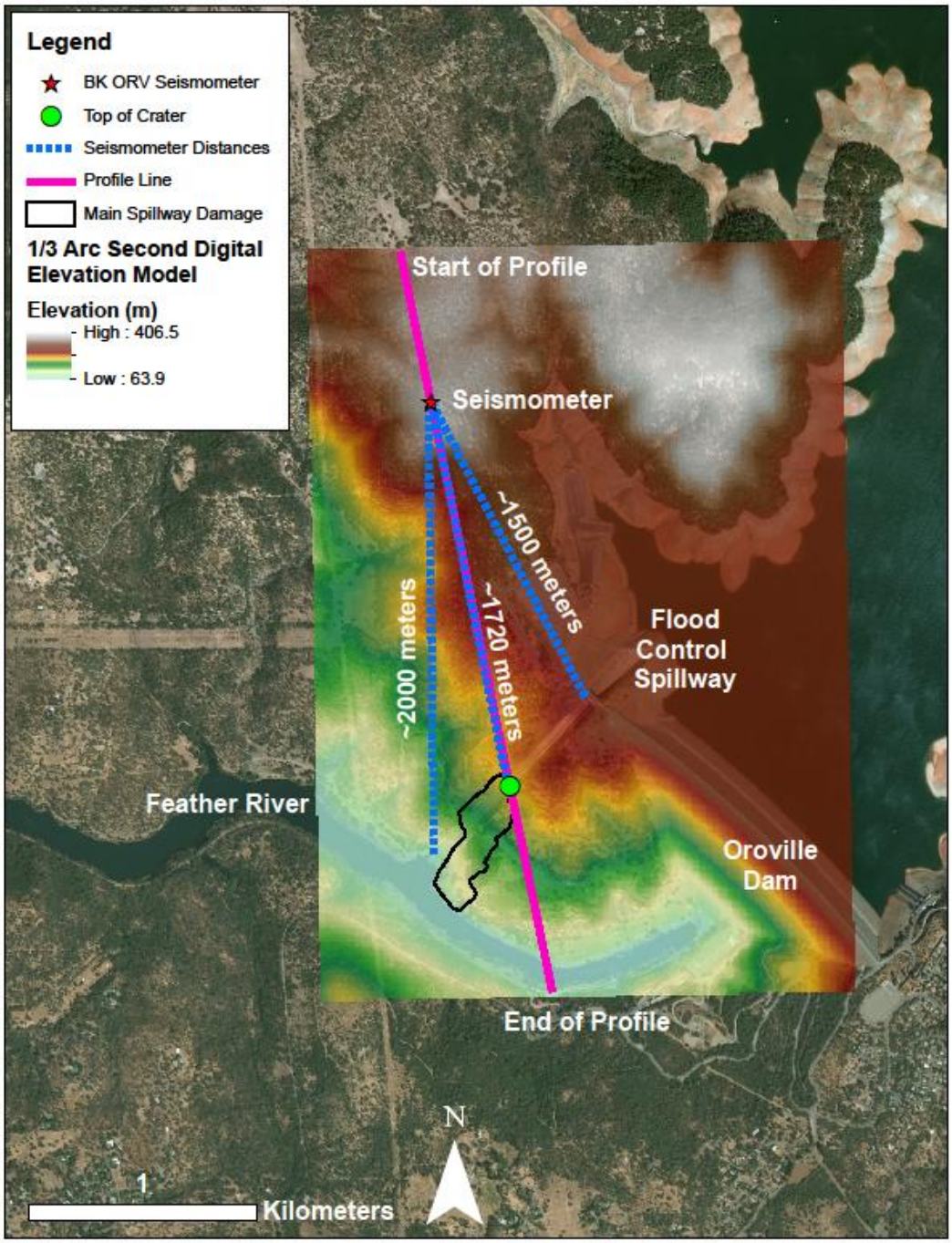

Figure S3- The hillside topography extracted for the SPECFEM2D simulation. If the entire length of the flood control spillway is considered an ambient seismic source, then the seismic waves travel a range of approximately 500 meters to the seismometer. In our simulation, we simplify this by simulating five sources spaced 100 meter apart along a profile line to the middle of the flood control spillway.

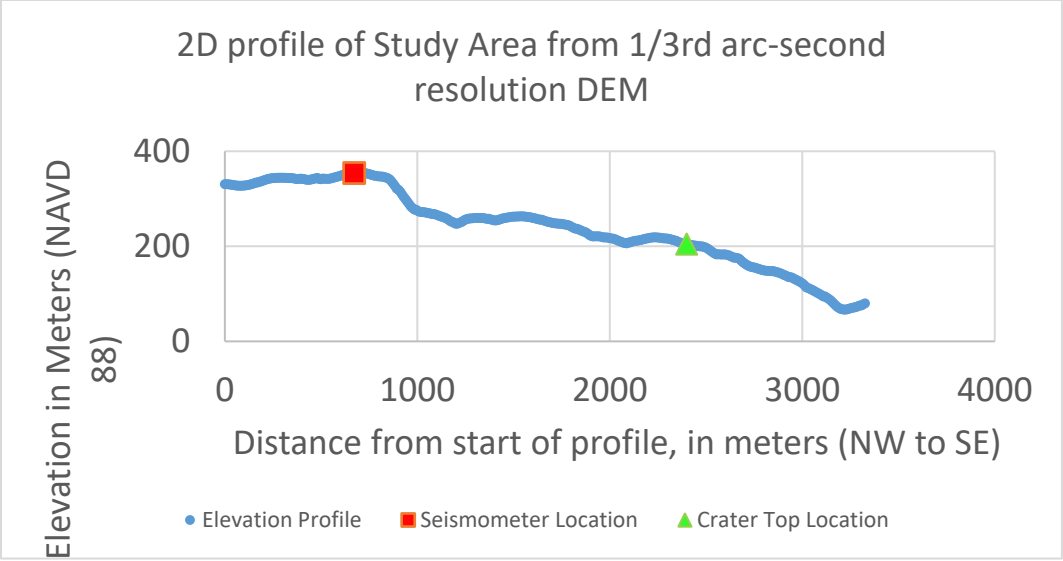

Figure S4- The elevation profile extracted for the SPECFEM2D simulation.

a)


BK ORV Sensor
May 2nd, 2013
Normal Spillway Operation
169.65
degrees
172.51
degrees
Increased turbulence
occurs after slope
change
Energy dissapation
at baffles
Google Earth
2000 ft

b)


Photo Taken: 2/7/2017
Source: CADWR
Initial Damage
Occurs at this
channel distance,
Equal with
bend in road

c)


BK ORV Sensor
February 12th, 2017
Mid-Incident
169.65
degrees
172.51
degrees
Channel headcut
has moved up
channel
Significant Turbulence
from headcut to river
Google Earth
2000 ft

g)


Photo Taken: 2/15/2017
Source: CADWR
Significiant drop in water,
deeply incised channel

h)


May 18th, 2017
After Study Period
Oroville
169.65
degrees
172.51
degrees
Channel headcut
has moved up
channel
Deeply
channelized flow
Google Earth
N
2000 ft

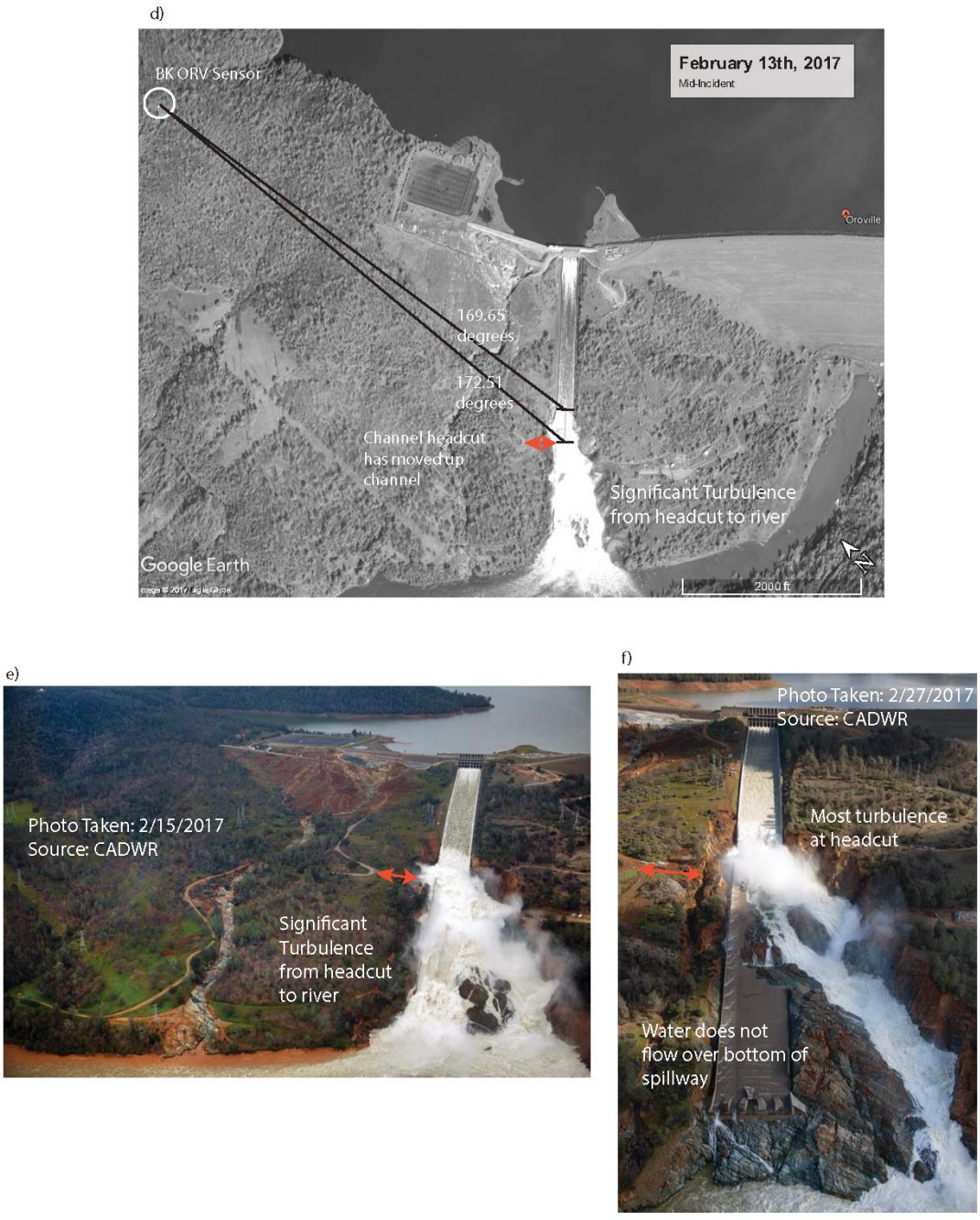

Figure S5 (a-f)- Aerial photographs collected during the time period of interest showing the evolution of the spillway erosion damage.

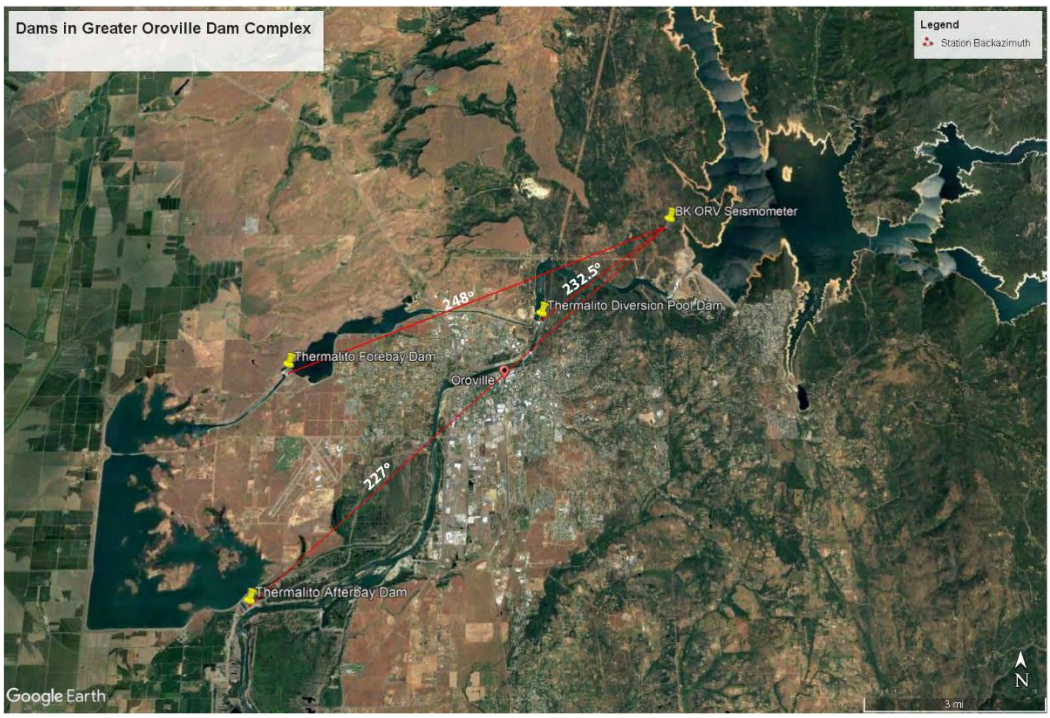

Figure S6- Three other dams- Thermalito Forebay Dam, Thermalito Diversion Pool Dam, and Thermalito Afterbay Dam- are a part of the Oroville Dam Complex and are at backazimuths of 248°, 232.5°, and 227°, respectively. The town of Oroville, California is located between station backazimuths of approximately 248° and 217°.

Appendix B: IPA Results for 2006 and 2011 Periods

2006 IPA Results

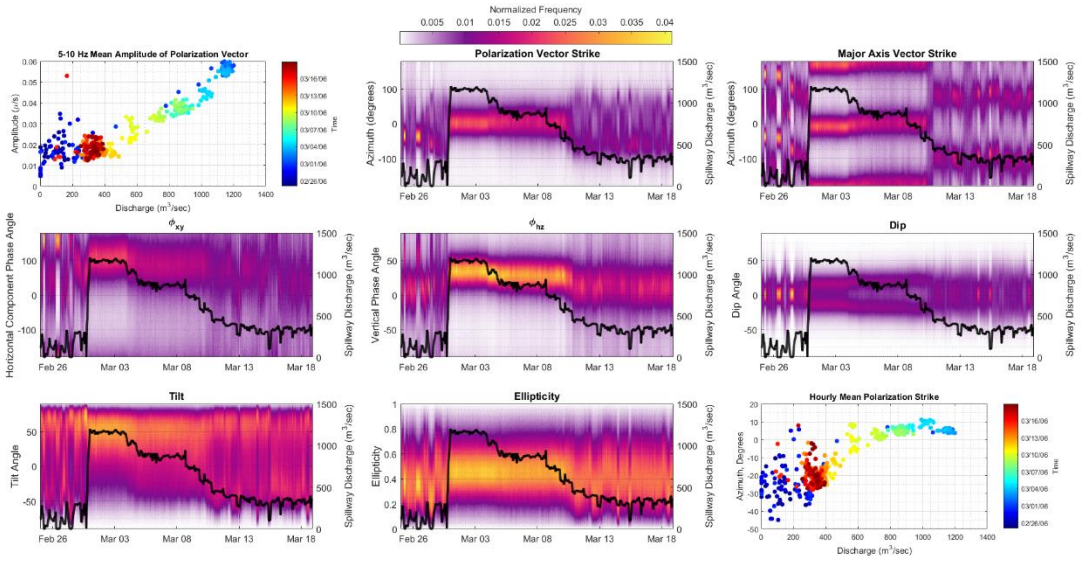

2011 IPA Results

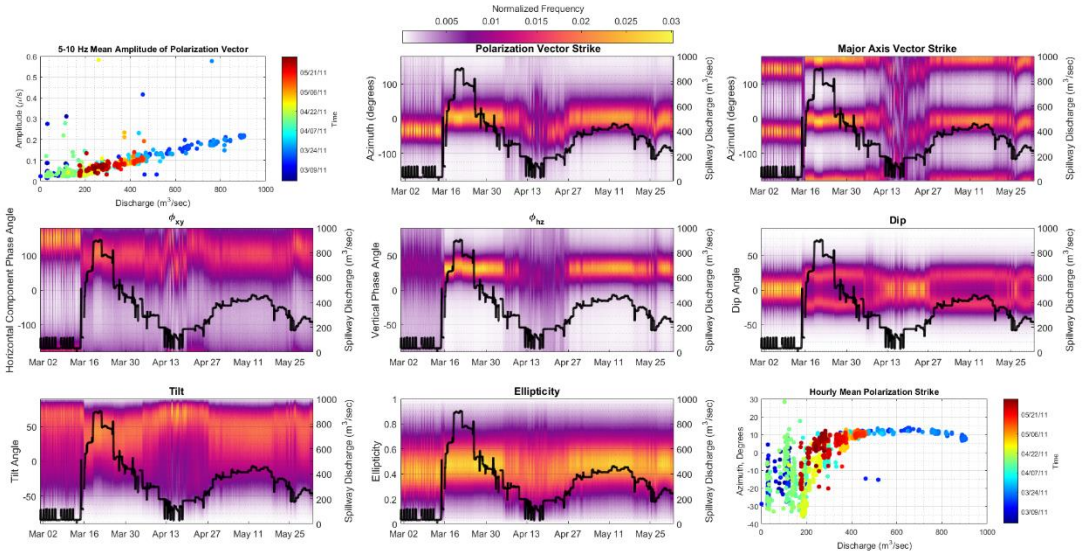

Appendix C: Grain Size Analysis

	Fraction of total								
Size Bin (mm)	**0+00**	**0+10**	**0+20**	**0+30**	**0+40**	**0+50**	**0+60**	**0+70**	**0+80**
2	0.000	0.000	0.000	0.000	0.000	0.000	0.000	0.000	0.000
4	0.000	0.000	0.000	0.000	0.000	0.000	0.000	0.000	0.000
5.6	0.000	0.000	0.000	0.000	0.000	0.000	0.000	0.000	0.000
8	0.000	0.000	0.000	0.000	0.000	0.000	0.000	0.000	0.000
11	0.008	0.000	0.000	0.000	0.000	0.000	0.000	0.000	0.000
16	0.000	0.009	0.000	0.000	0.019	0.000	0.000	0.000	0.016
22	0.040	0.065	0.090	0.054	0.057	0.050	0.048	0.054	0.049
32	0.032	0.037	0.072	0.089	0.114	0.107	0.048	0.071	0.024
45	0.143	0.093	0.144	0.152	0.095	0.107	0.086	0.134	0.146
64	0.087	0.139	0.153	0.152	0.162	0.124	0.143	0.170	0.187
90	0.183	0.111	0.153	0.179	0.210	0.149	0.152	0.223	0.195
128	0.222	0.259	0.216	0.259	0.190	0.256	0.333	0.259	0.228
180	0.143	0.167	0.117	0.089	0.124	0.190	0.114	0.045	0.122
256	0.119	0.102	0.054	0.027	0.029	0.017	0.067	0.045	0.033
360	0.024	0.019	0.000	0.000	0.000	0.000	0.000	0.000	0.000
512	0.000	0.000	0.000	0.000	0.000	0.000	0.010	0.000	0.000
Total Number Collected	126	108	111	112	105	121	105	112	123
D84 (mm)	176	166	132	120	126	139	140	116	127
D50 (mm)	92	96	68	71	69	82	93	71	73
D84/D50 Ratio	1.913043	1.729167	1.941176	1.690141	1.826087	1.695122	1.505376	1.633803	1.739726

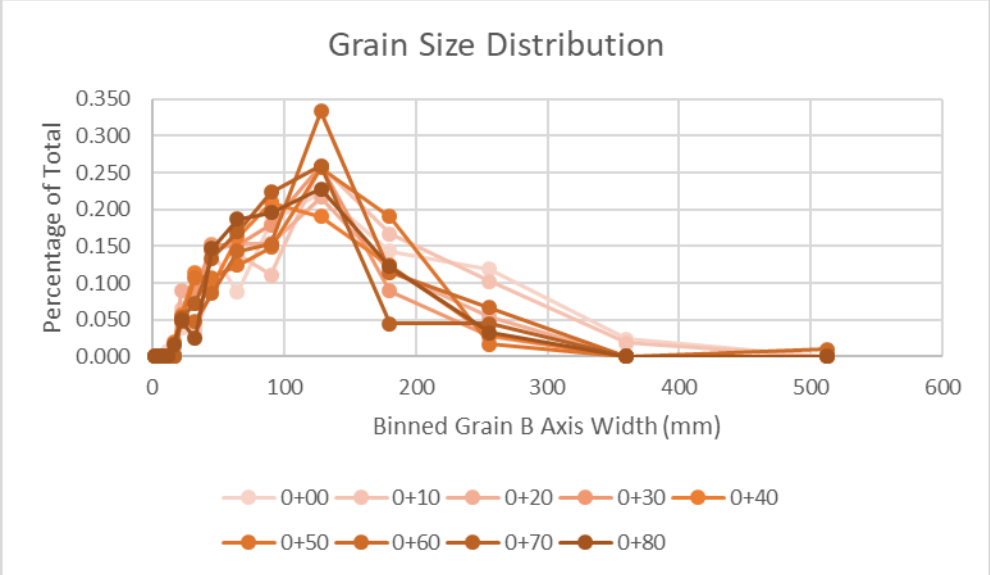

Appendix D: Simulated Hydraulic Geometry Relationships

	Cross Section Number (Upstream to Downstream)	Depth Coefficient	Depth Exponent	Width Coefficient	Width Exponent	Velocity Coefficient	Velocity Exponent	Coefficients Multiplied	Sum of Exponents	Q = 0.1	Q = 1	Q = 10
Low Discharge	1	0.29	0.34	12.22	0.07	0.29	0.57	1.03	0.98	0.11	1.03	9.71
	2	0.26	0.34	14.09	0.07	0.31	0.53	1.14	0.94	0.13	1.11	9.68
	3	0.29	0.34	15.89	0.03	0.24	0.57	1.11	0.94	0.12	1.09	9.56
	4	0.22	0.45	16.46	0.05	0.27	0.5	0.98	1.00	0.10	0.98	9.83
	5	0.19	0.45	16.15	0.05	0.35	0.47	1.07	0.97	0.11	1.05	9.69
	6	0.18	0.49	15.79	0.04	0.34	0.48	0.97	1.01	0.10	0.98	9.88
	7	0.12	0.72	16.08	0.09	0.5	0.16	0.96	0.97	0.11	0.98	9.02
	8	0.11	0.61	17.27	0.05	0.54	0.29	1.03	0.95	0.12	1.07	9.57
	9	0.25	0.35	16.46	0.03	0.25	0.61	1.03	0.99	0.10	1.02	9.90
	10	0.26	0.34	16.93	0.03	0.23	0.63	1.01	1.00	0.10	1.00	9.94
	11	0.38	0.23	15.67	0.04	0.17	0.72	1.01	0.99	0.10	1.01	9.91
Mid Discharge	1	0.29	0.34	12.22	0.07	0.29	0.57	1.03	0.98	0.11	1.03	9.71
	2	0.26	0.34	14.09	0.07	0.31	0.53	1.14	0.94	0.13	1.11	9.68
	3	0.29	0.34	15.89	0.03	0.24	0.57	1.11	0.94	0.12	1.09	9.56
	4	0.22	0.45	16.46	0.05	0.27	0.5	0.98	1.00	0.10	0.98	9.83
	5	0.19	0.45	16.15	0.05	0.35	0.47	1.07	0.97	0.11	1.05	9.69
	6	0.18	0.49	15.79	0.04	0.34	0.48	0.97	1.01	0.10	0.98	9.88
	7	0.12	0.72	16.08	0.09	0.5	0.16	0.96	0.97	0.11	0.98	9.02
	8	0.11	0.61	17.27	0.05	0.54	0.29	1.03	0.95	0.12	1.07	9.57
	9	0.25	0.35	16.46	0.03	0.25	0.61	1.03	0.99	0.10	1.02	9.90
	10	0.26	0.34	16.93	0.03	0.23	0.63	1.01	1.00	0.10	1.00	9.94
	11	0.38	0.23	15.67	0.04	0.17	0.72	1.01	0.99	0.10	1.01	9.91
High Discharge	1	0.48	0.22	10.14	0.14	0.23	0.62	1.12	0.98	0.12	1.12	10.62
	2	0.34	0.3	13.24	0.1	0.22	0.6	0.99	1.00	0.10	0.99	10.00
	3	0.42	0.27	12.87	0.1	0.19	0.62	1.03	0.99	0.10	0.99	10.01
	4	0.38	0.29	14.59	0.09	0.18	0.62	1.00	1.00	0.10	0.98	9.92
	5	0.25	0.38	15.57	0.08	0.25	0.55	0.97	1.01	0.09	0.96	9.86
	6	0.3	0.35	13.63	0.1	0.24	0.56	0.98	1.01	0.10	0.99	9.97
	7	0.14	0.53	15.78	0.08	0.47	0.39	1.04	1.00	0.10	1.01	9.98
	8	0.22	0.41	16.01	0.08	0.28	0.51	0.99	1.00	0.10	0.98	9.92
	9	0.25	0.4	14.91	0.09	0.26	0.52	0.97	1.01	0.10	0.98	9.93
	10	0.26	0.4	15.49	0.08	0.24	0.53	0.97	1.01	0.09	0.97	9.90
	11	0.34	0.34	12.85	0.13	0.23	0.54	1.00	1.01	0.10	0.98	9.97

Appendix F: Ambient Noise Thresholds

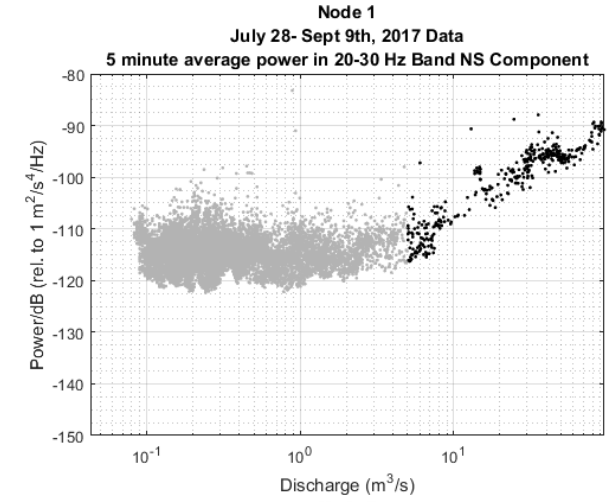

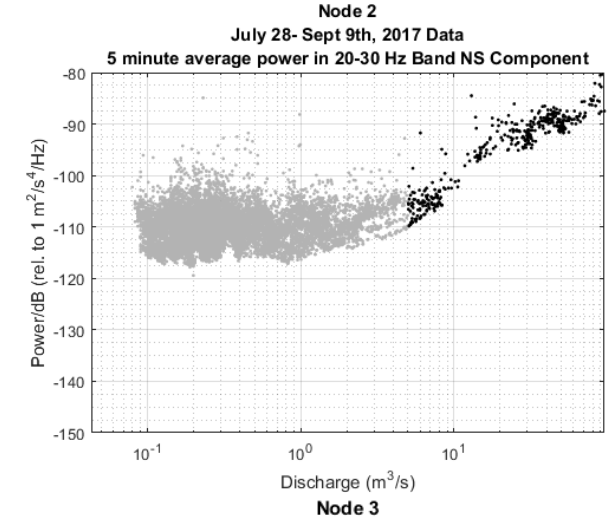

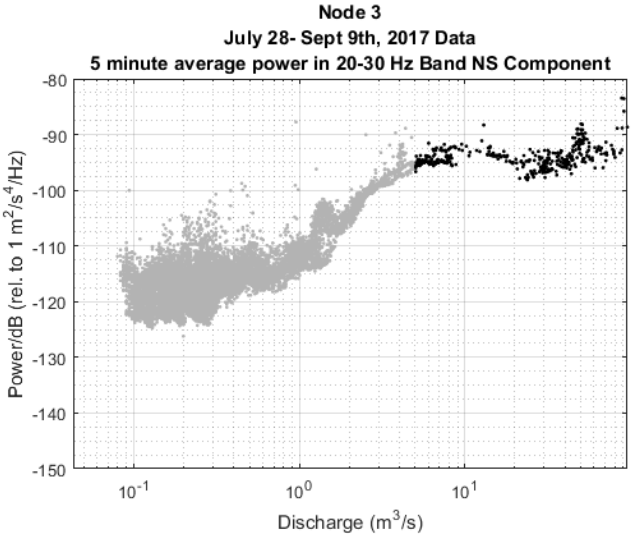

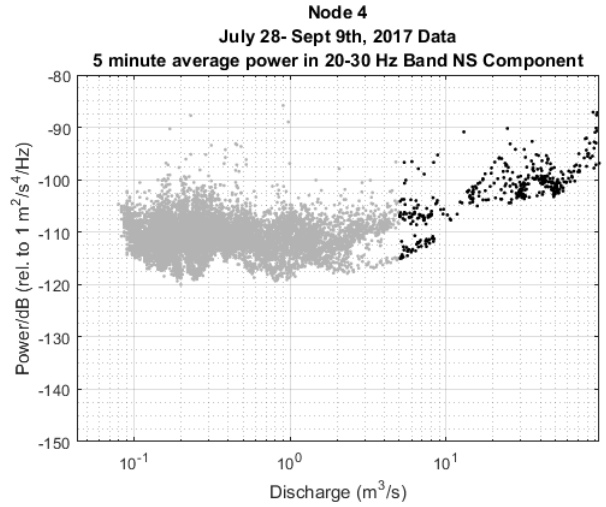
Node 4
July 28- Sept 9th, 2017 Data
5 minute average power in 20-30 Hz Band NS Component
Power/dB (rel. to 1 m²/s⁴/Hz)
Discharge (m³/s)

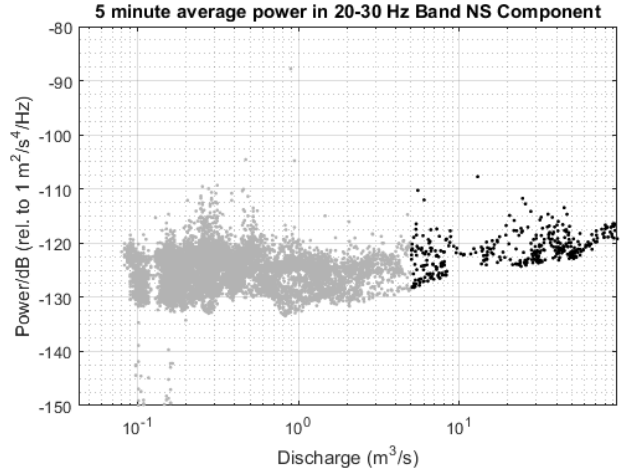
Node 5
July 28- Sept 9th, 2017 Data
5 minute average power in 20-30 Hz Band NS Component
Power/dB (rel. to 1 m²/s⁴/Hz)
Discharge (m³/s)

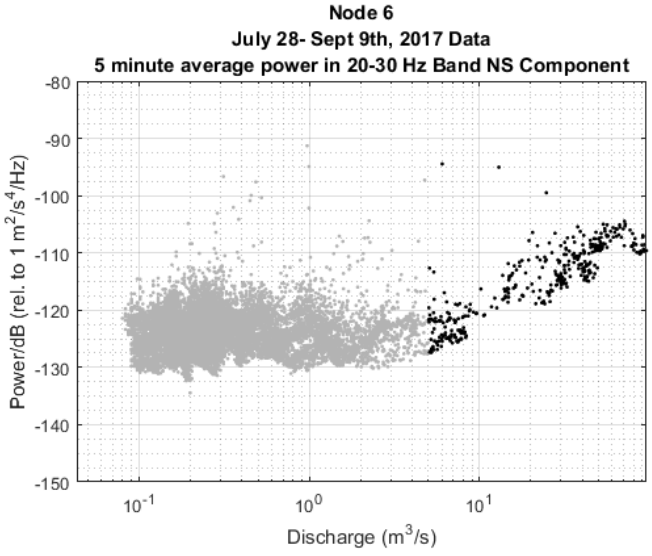
Node 6
July 28- Sept 9th, 2017 Data
5 minute average power in 20-30 Hz Band NS Component
Power/dB (rel. to 1 m²/s⁴/Hz)
Discharge (m³/s)

Appendix G: Additional Spectrograms of 5 minute Mean Power

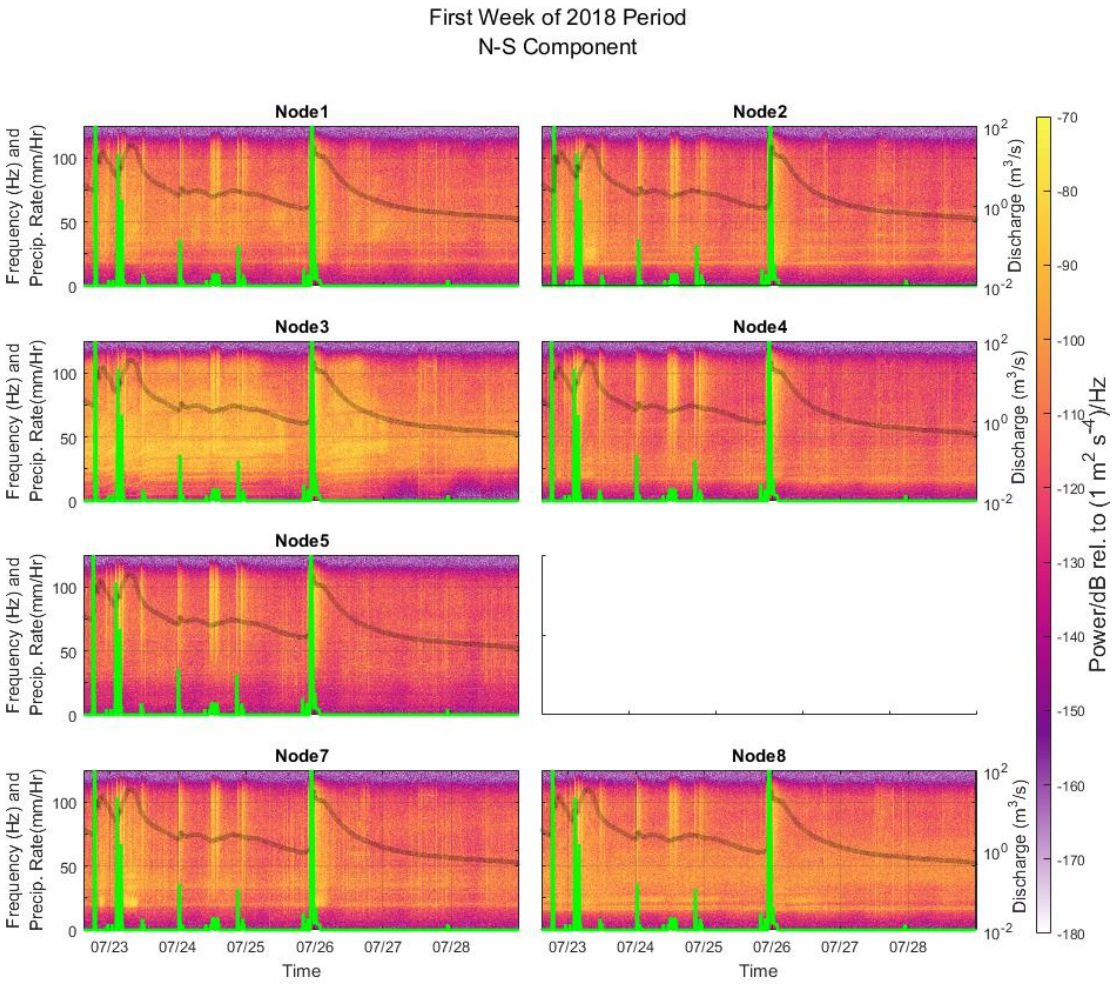

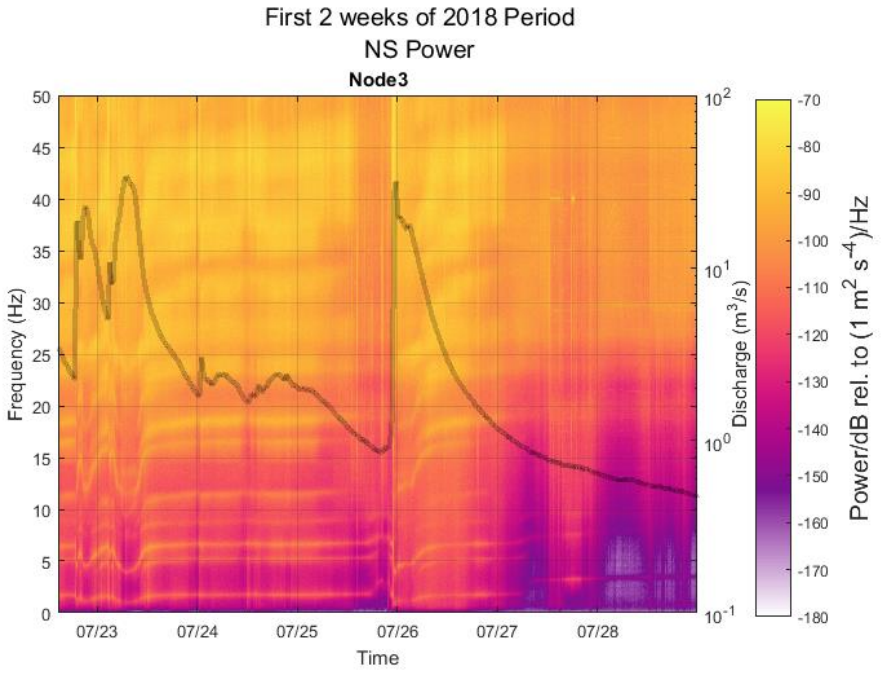
First 2 weeks of 2018 Period
NS Power
Node3
Frequency (Hz)
Discharge (m3/s)
Power/dB rel. to (1 m2 s-4)/Hz
Time
07/23
07/24
07/25
07/26
07/27
07/28

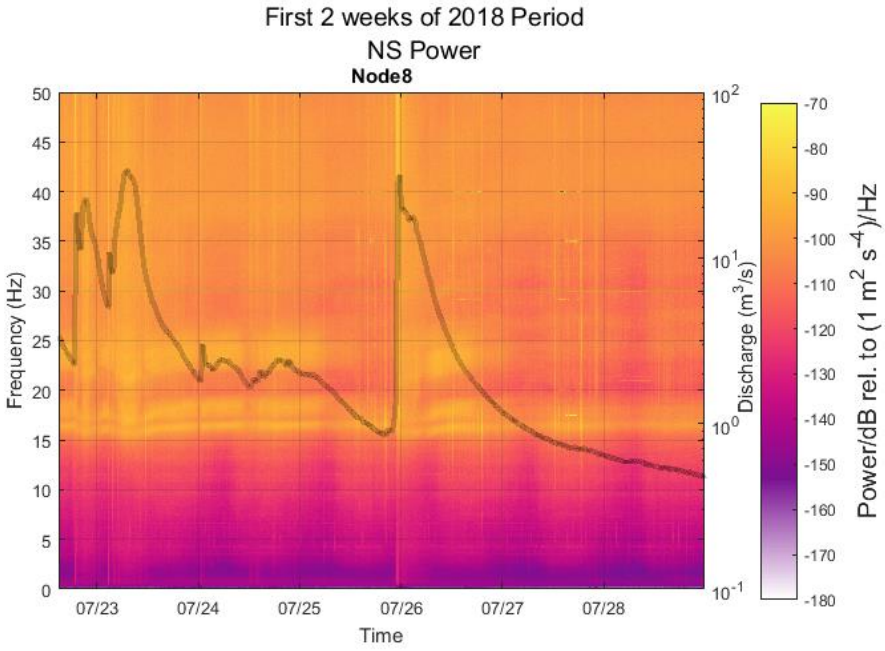
First 2 weeks of 2018 Period
NS Power
Node8
Frequency (Hz)
Discharge (m3/s)
Power/dB rel. to (1 m2 s-4)/Hz
Time
07/23
07/24
07/25
07/26
07/27
07/28

Appendix H: Discharge-Scaling Results Colored by Traffic Counts

All Results Colored by Traffic Volume

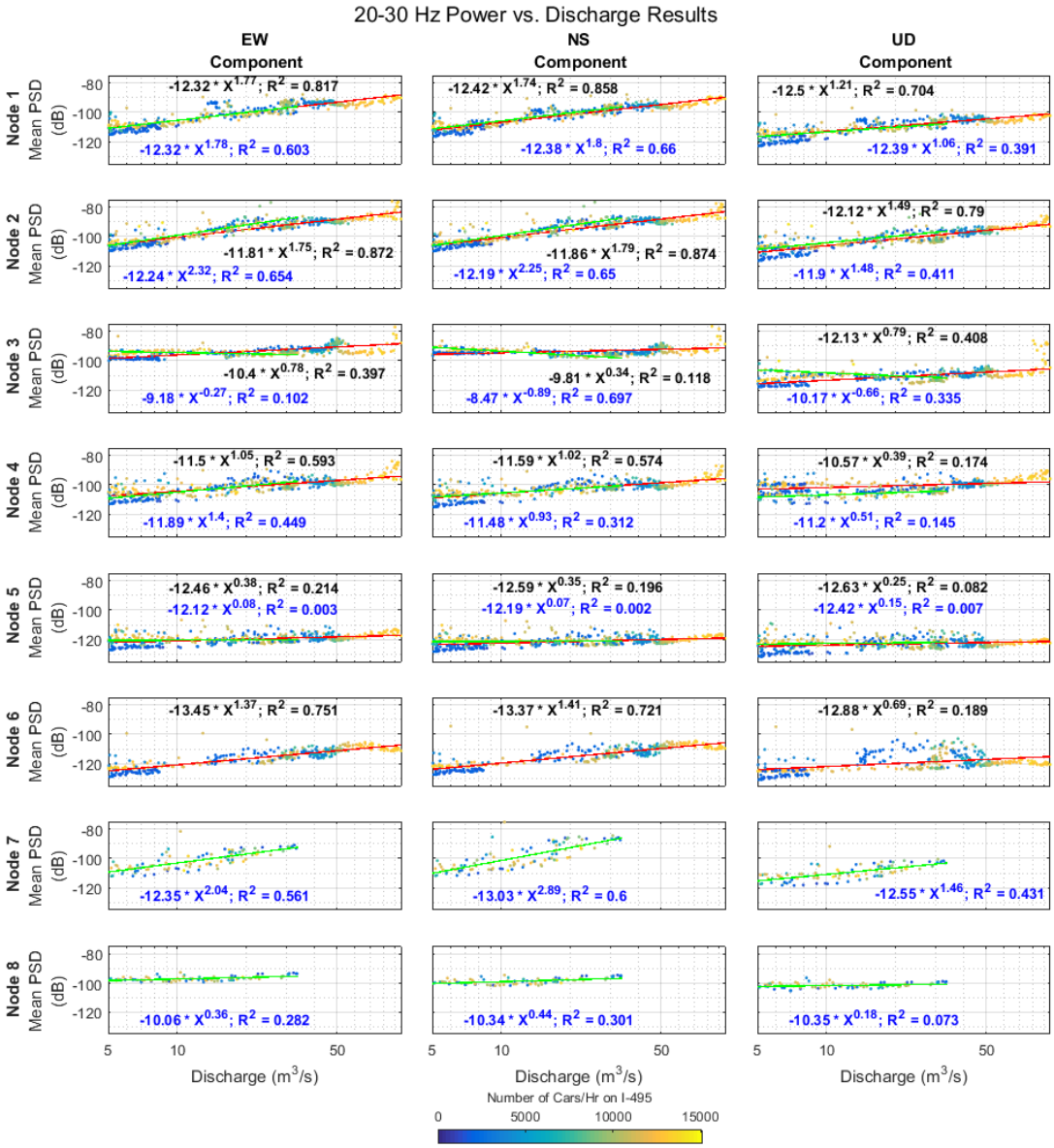

Scaling results for only five minute intervals when fewer than 5000 cars/hour travel on I-495

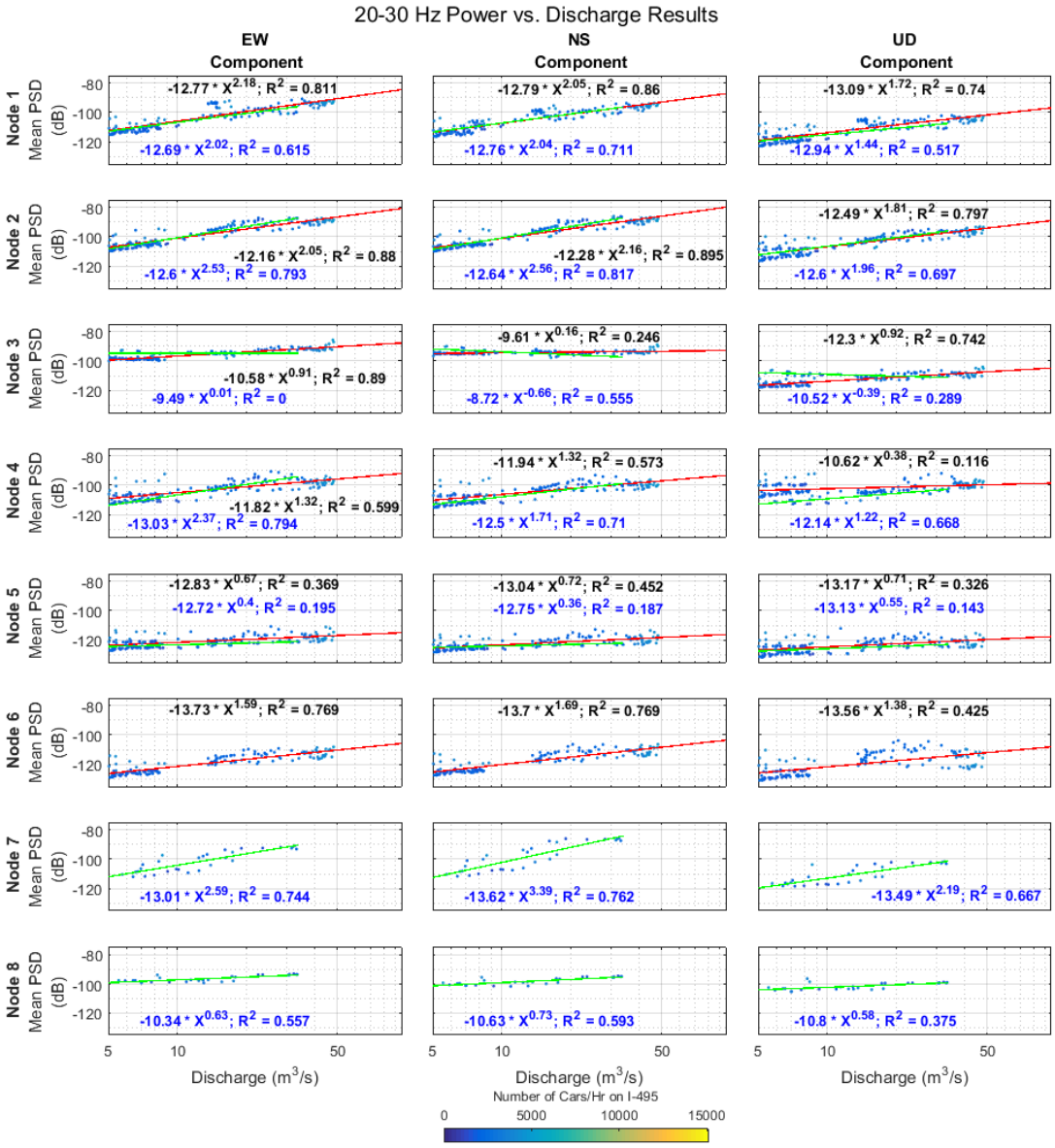
20-30 Hz Power vs. Discharge Results
EW Component
NS Component
UD Component
Node 1
Node 2
Node 3
Node 4
Node 5
Node 6
Node 7
Node 8
Mean PSD (dB)
-80
-100
-120
-12.77 * X^2.18; R^2 = 0.811
-12.69 * X^2.02; R^2 = 0.615
-12.79 * X^2.05; R^2 = 0.86
-12.76 * X^2.04; R^2 = 0.711
-13.09 * X^1.72; R^2 = 0.74
-12.94 * X^1.44; R^2 = 0.517
-12.16 * X^2.05; R^2 = 0.88
-12.6 * X^2.53; R^2 = 0.793
-12.28 * X^2.16; R^2 = 0.895
-12.64 * X^2.56; R^2 = 0.817
-12.49 * X^1.81; R^2 = 0.797
-12.6 * X^1.96; R^2 = 0.697
-10.58 * X^0.91; R^2 = 0.89
-9.49 * X^0.01; R^2 = 0
-9.61 * X^0.16; R^2 = 0.246
-8.72 * X^-0.66; R^2 = 0.555
-12.3 * X^0.92; R^2 = 0.742
-10.52 * X^-0.39; R^2 = 0.289
-11.82 * X^1.32; R^2 = 0.599
-13.03 * X^2.37; R^2 = 0.794
-11.94 * X^1.32; R^2 = 0.573
-12.5 * X^1.71; R^2 = 0.71
-10.62 * X^0.38; R^2 = 0.116
-12.14 * X^1.22; R^2 = 0.668
-12.83 * X^0.67; R^2 = 0.369
-12.72 * X^0.4; R^2 = 0.195
-13.04 * X^0.72; R^2 = 0.452
-12.75 * X^0.36; R^2 = 0.187
-13.17 * X^0.71; R^2 = 0.326
-13.13 * X^0.55; R^2 = 0.143
-13.73 * X^1.59; R^2 = 0.769
-13.7 * X^1.69; R^2 = 0.769
-13.56 * X^1.38; R^2 = 0.425
-13.01 * X^2.59; R^2 = 0.744
-13.62 * X^3.39; R^2 = 0.762
-13.49 * X^2.19; R^2 = 0.667
-10.34 * X^0.63; R^2 = 0.557
-10.63 * X^0.73; R^2 = 0.593
-10.8 * X^0.58; R^2 = 0.375
5
10
50
Discharge (m^3/s)
Number of Cars/Hr on I-495
0
5000
10000
15000

20-30 Hz Scaling with curve fit only to data between 5 and 30 m^3/s

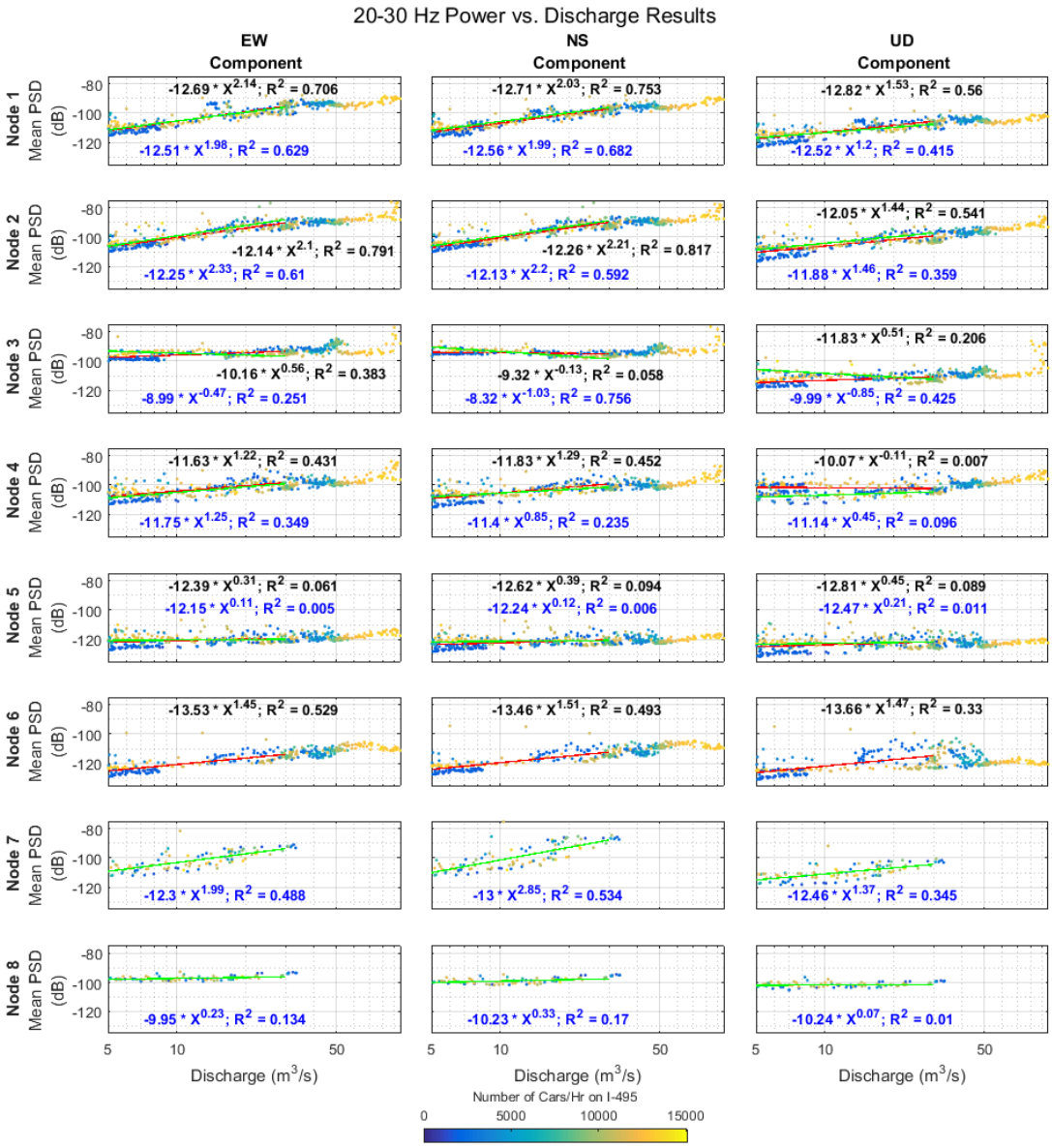

2017 Data; East-West Component Comparison

Node Number	All Data		Data Below 5000 cars/Hr Threshold		All data with a maximum of 30 m^3/s for curve fit	
	Exponent	R^2	Exponent	R^2	Exponent	R^2
Node 1	1.77	0.817	2.18	0.811	2.14	0.706
Node 2	1.75	0.872	2.05	0.88	2.1	0.791
Node 3	0.78	0.397	0.91	0.89	0.56	0.383
Node 4	1.05	0.593	1.32	0.599	1.22	0.431
Node 5	0.38	0.214	0.67	0.369	0.31	0.061
Node 6	1.37	0.751	1.59	0.769	1.45	0.529

Appendix I: FDPA Results for Additional Floods

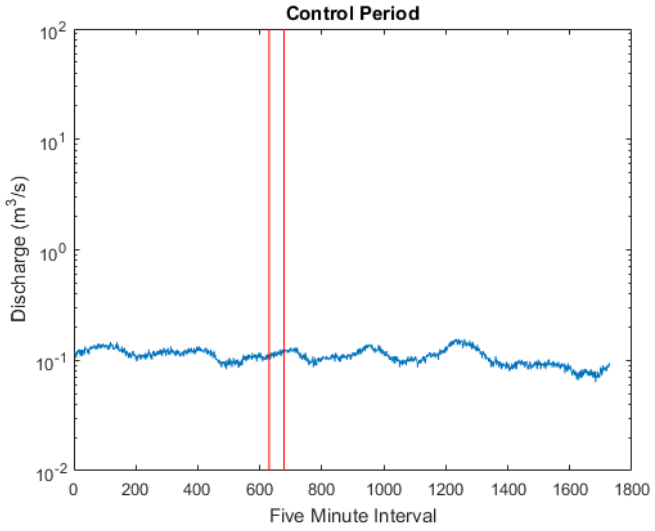

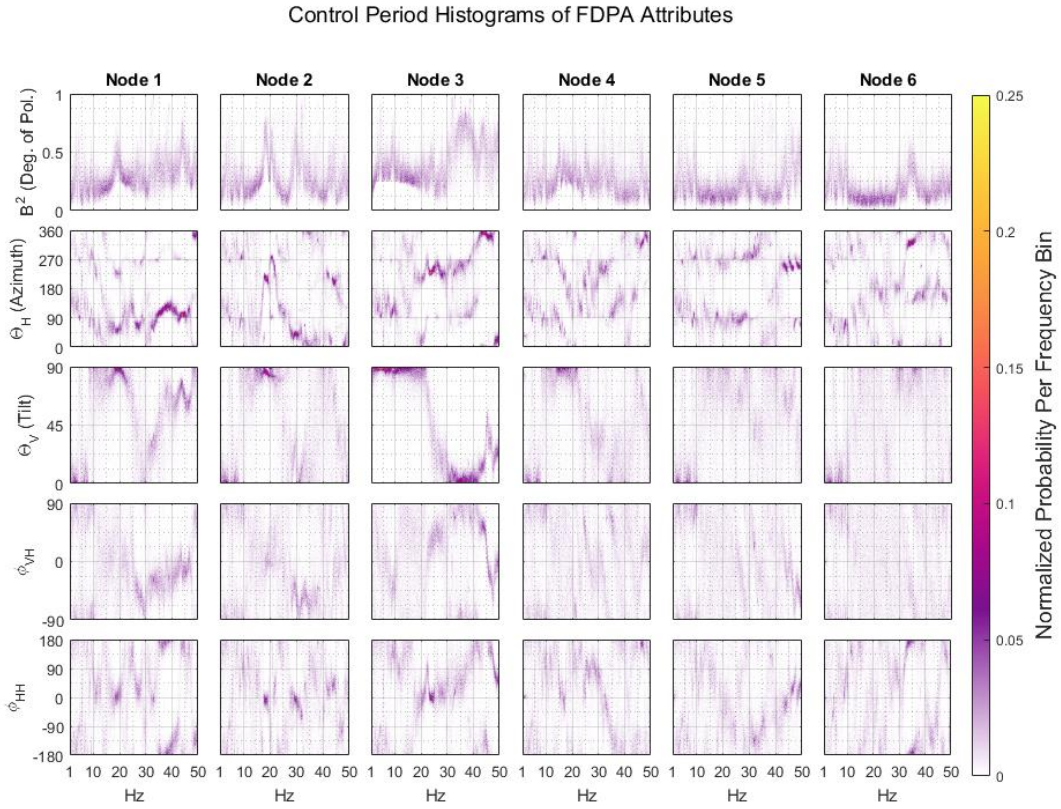

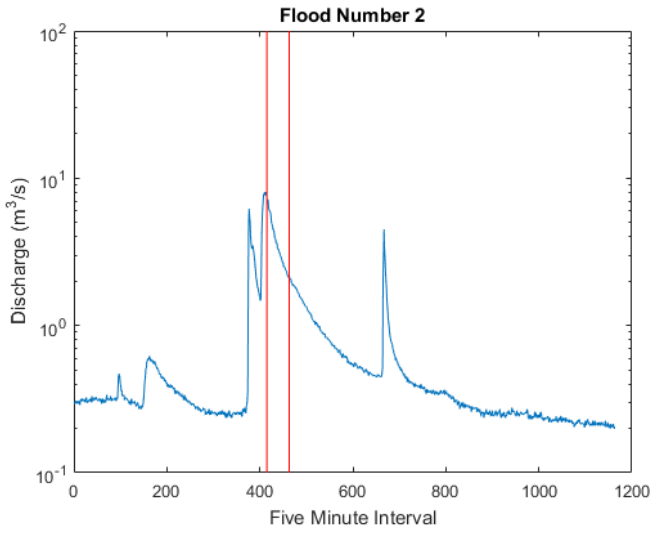

Flood 2Histograms of FDPA Attributes

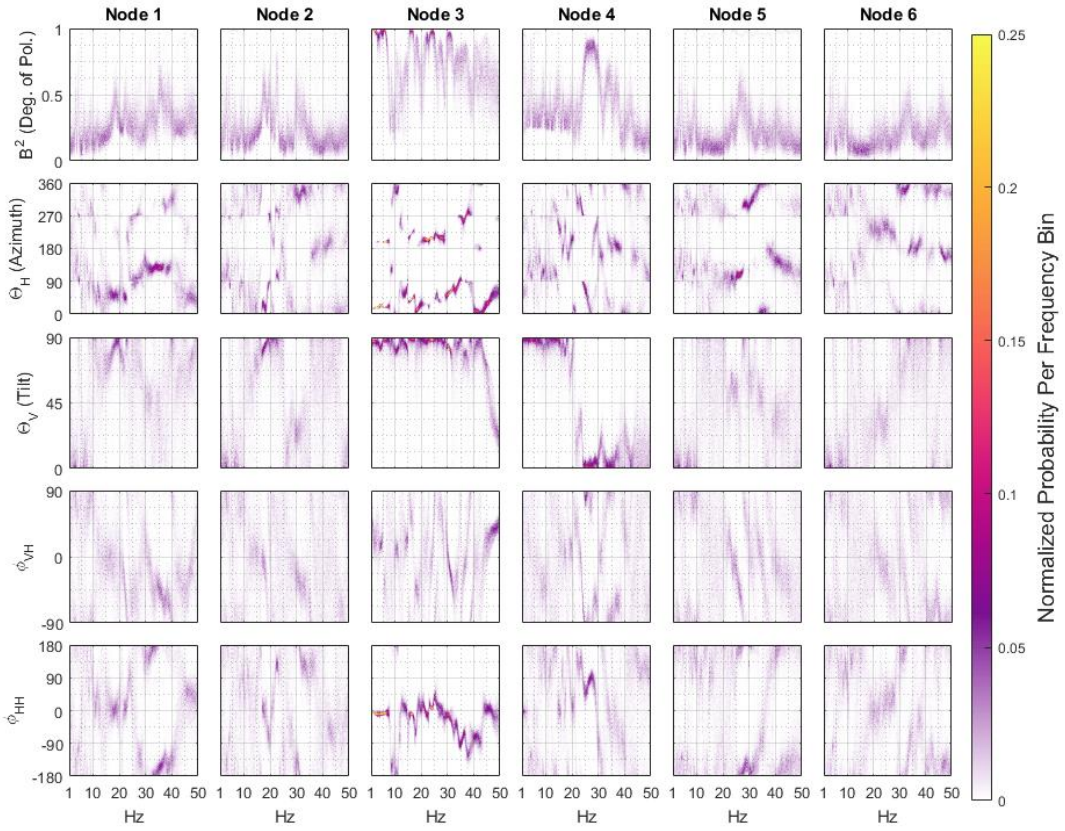

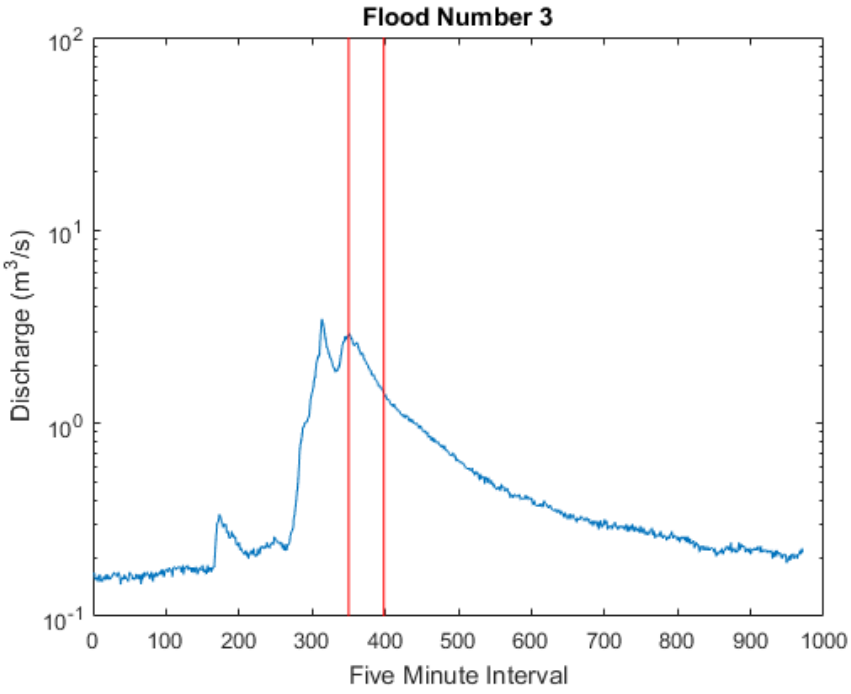

Flood 3Histograms of FDPA Attributes

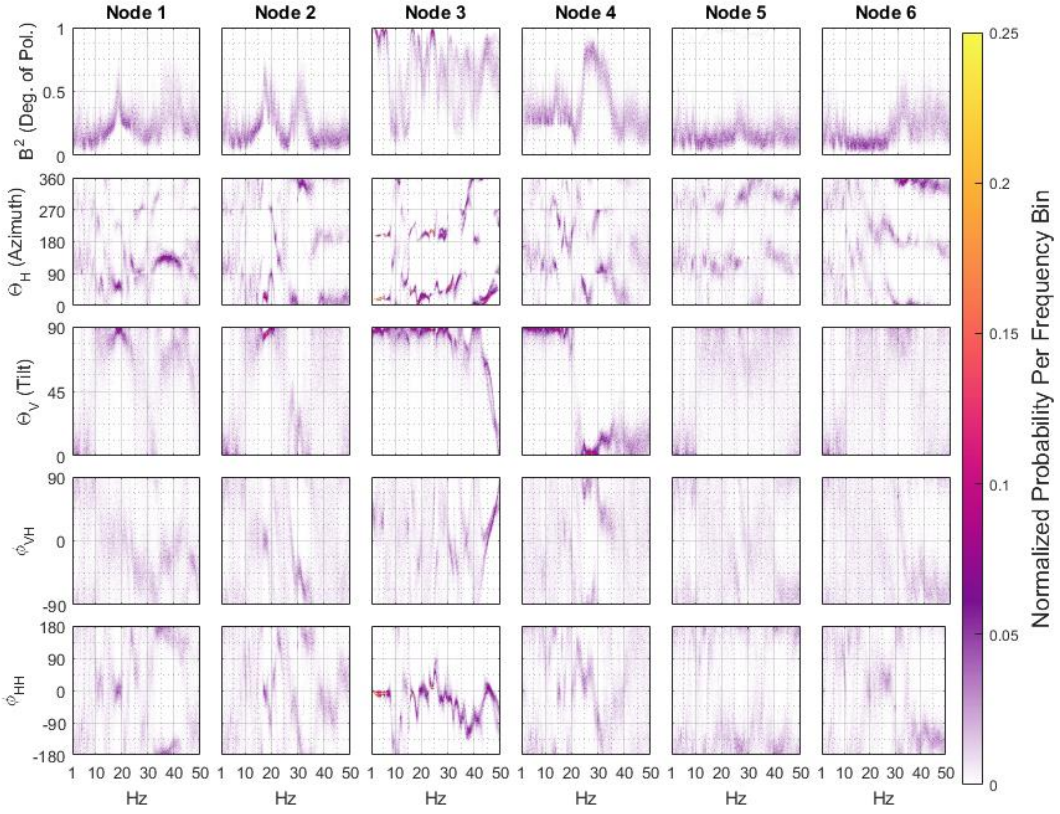

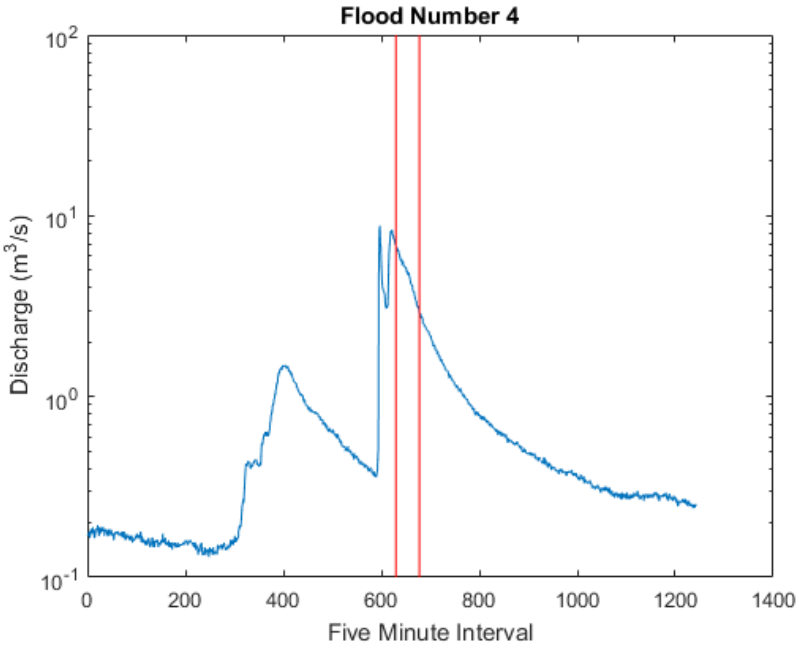
Flood Number 4
Discharge (m3/s)
Five Minute Interval


Flood 4Histograms of FDPA Attributes
Node 1
Node 2
Node 3
Node 4
Node 5
Node 6
B2 (Deg. of Pol.)
ΘH (Azimuth)
ΘV (Tilt)
φVH
φHH
Hz
Normalized Probability Per Frequency Bin

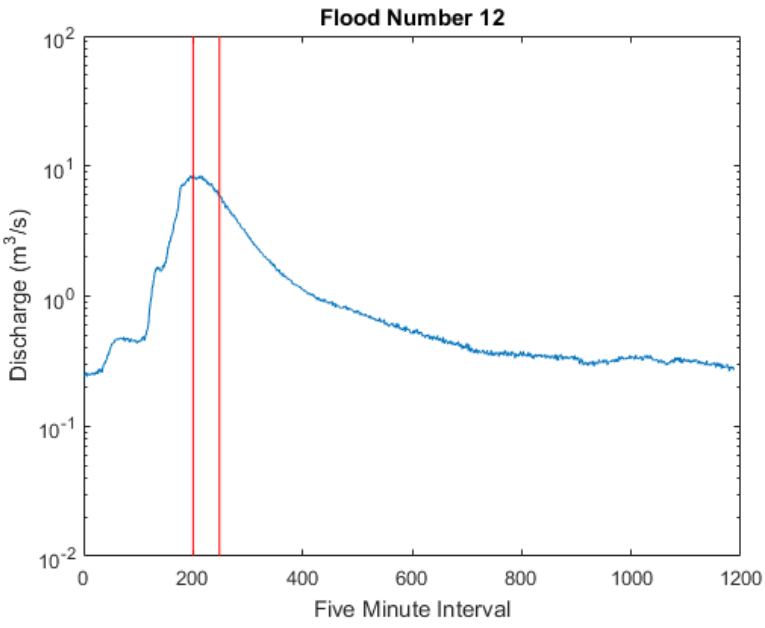

Flood 12 Histograms of FDPA Attributes

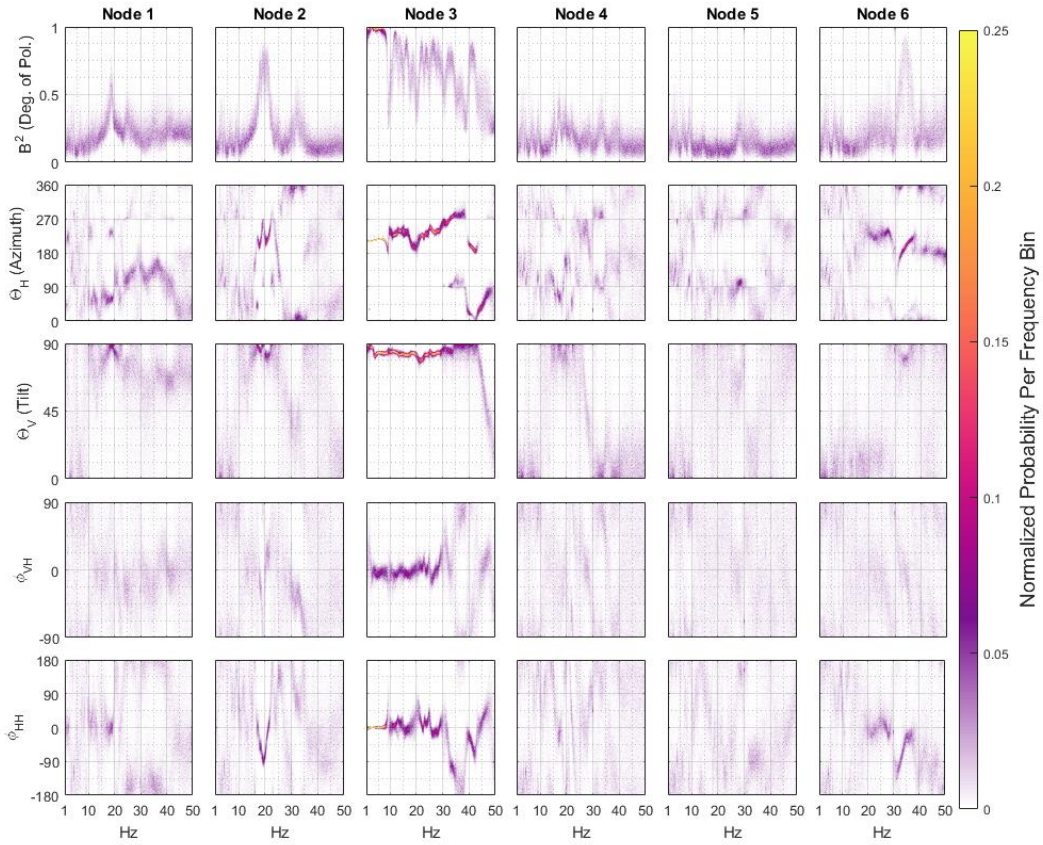

Appendix J: FDPA Results Using Varying Window Lengths

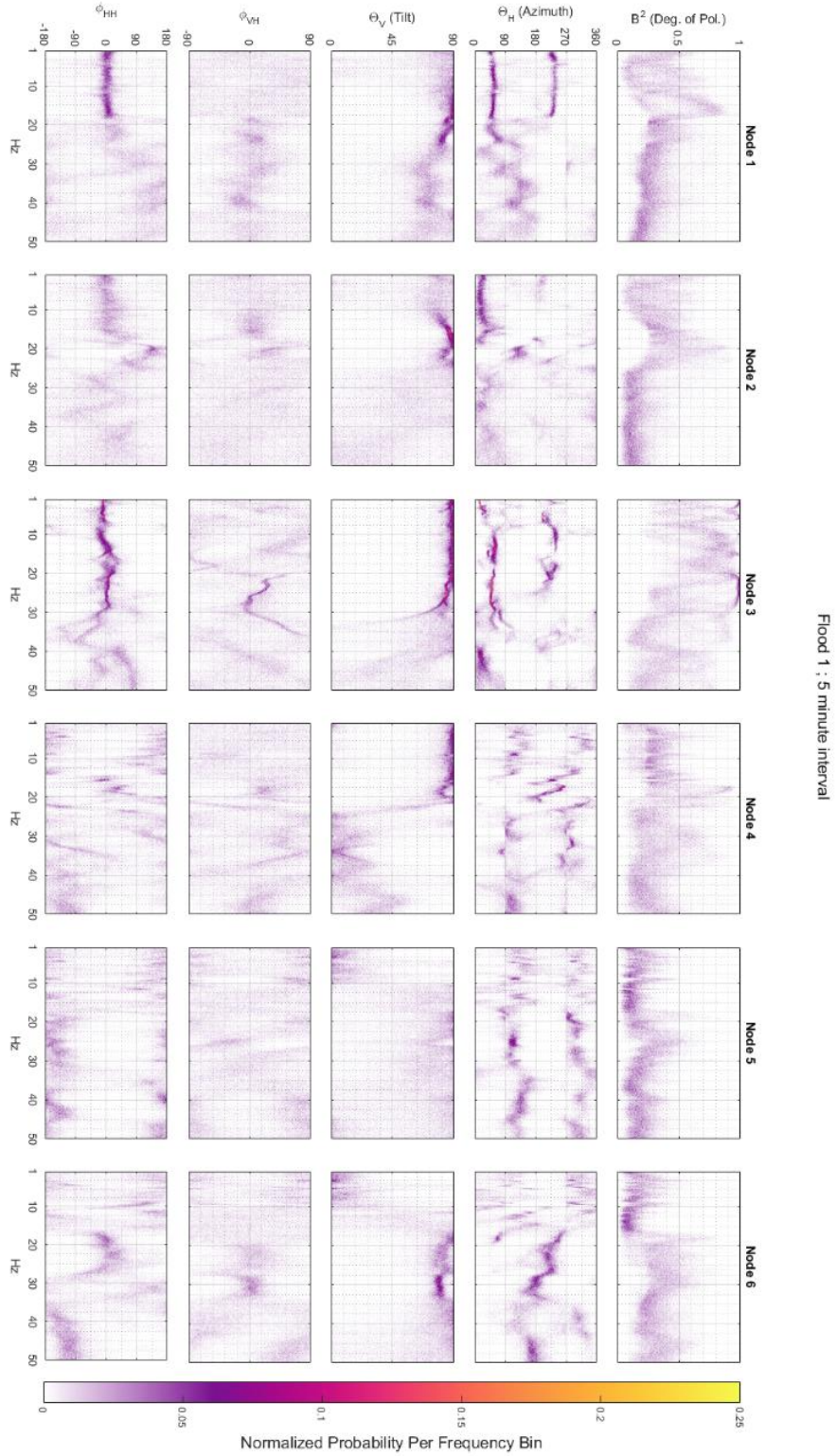

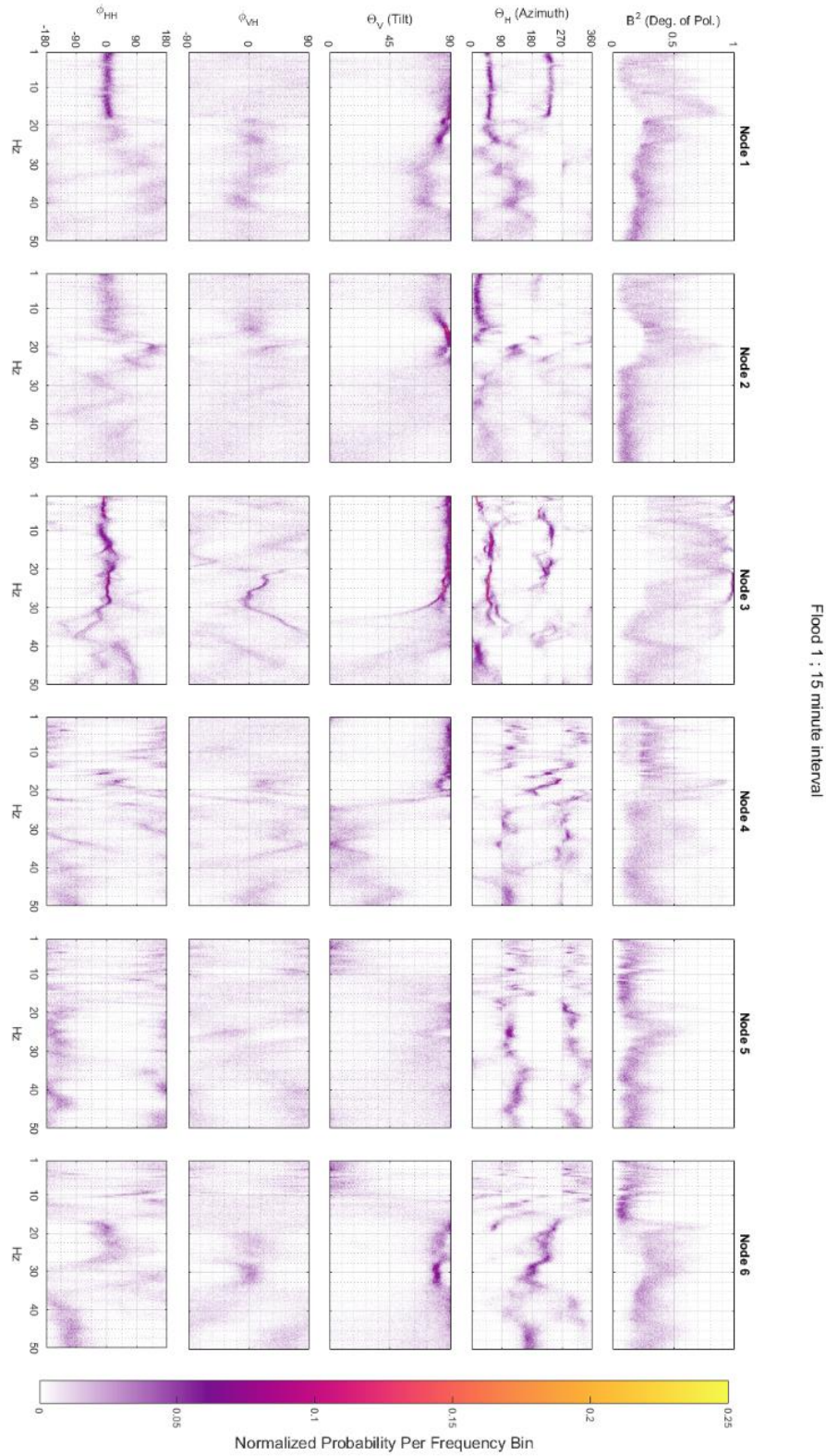
Flood 1 ; 15 minute interval
B² (Deg. of Pol.)
Θ_H (Azimuth)
Θ_V (Tilt)
Φ_VH
Φ_HH
Node 1
Node 2
Node 3
Node 4
Node 5
Node 6
Hz
Normalized Probability Per Frequency Bin

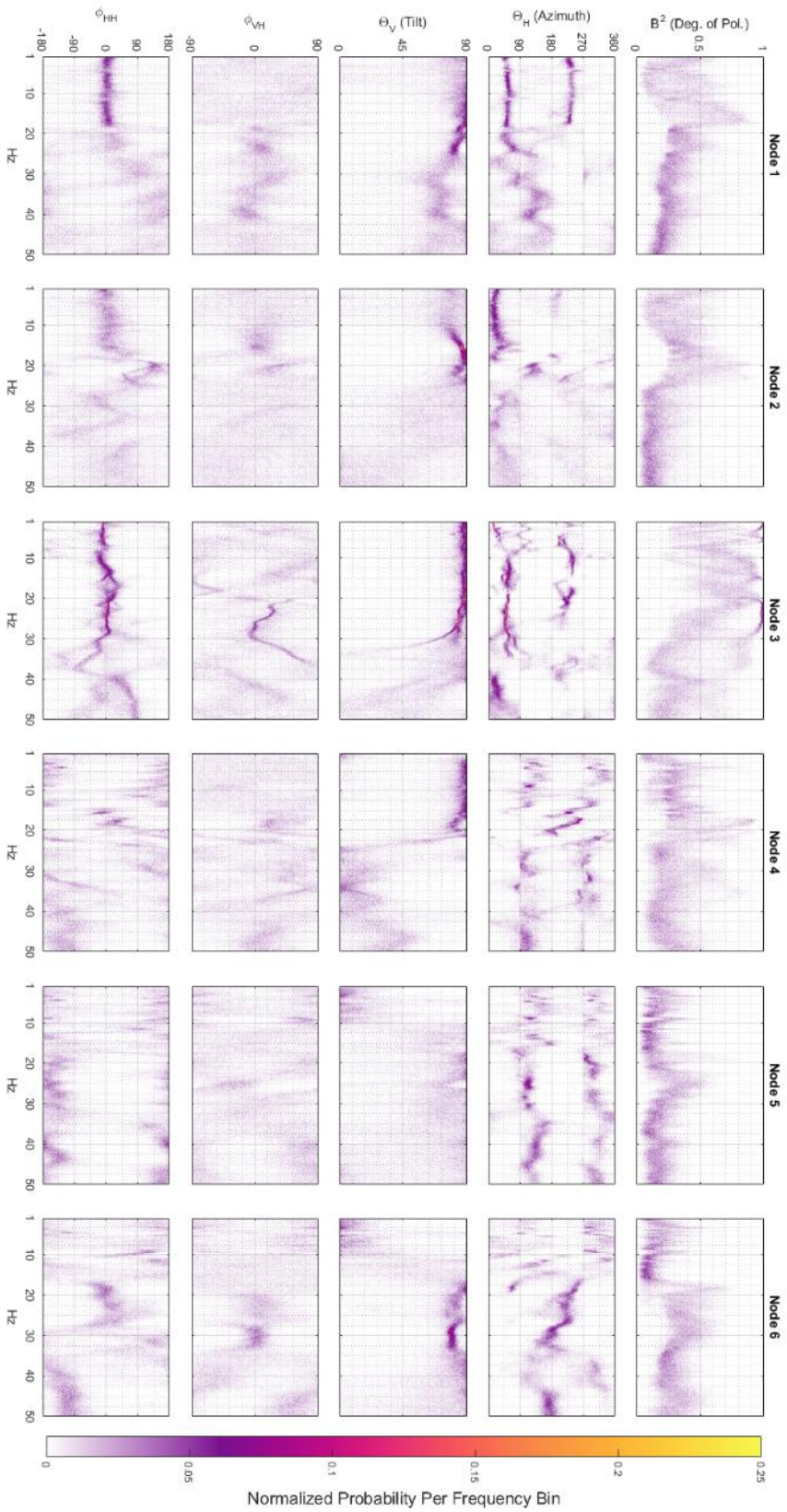

Flood 1 ; 30 minute interval

Appendix K: Evidence of Faulty Node Vertical Component

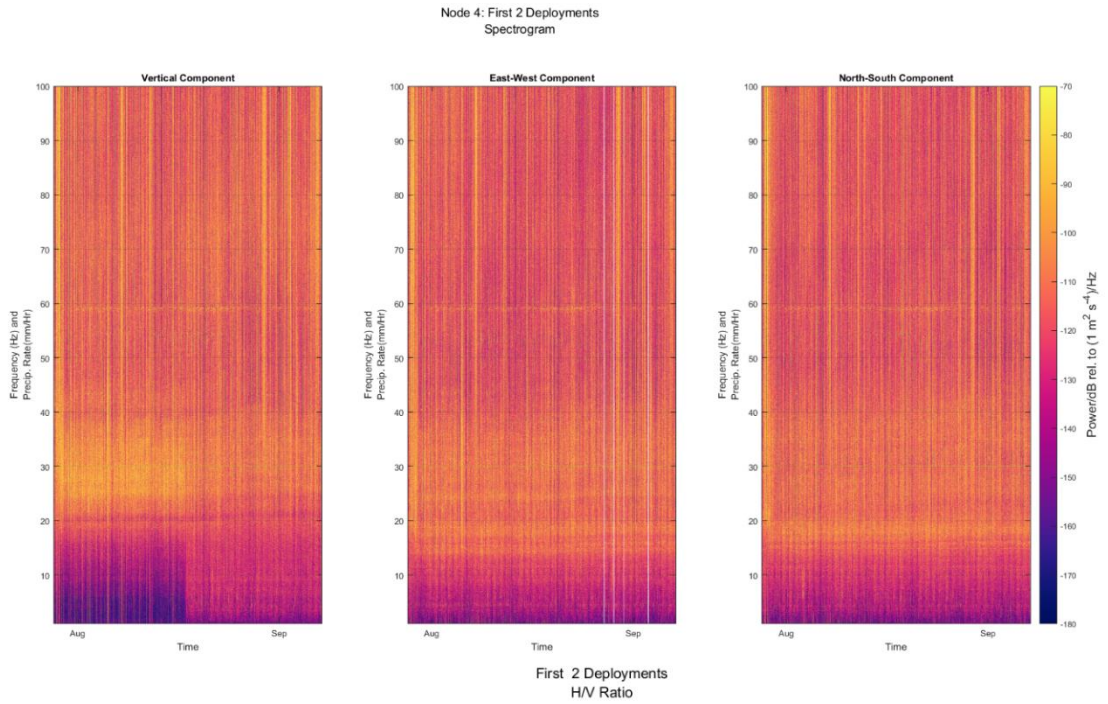

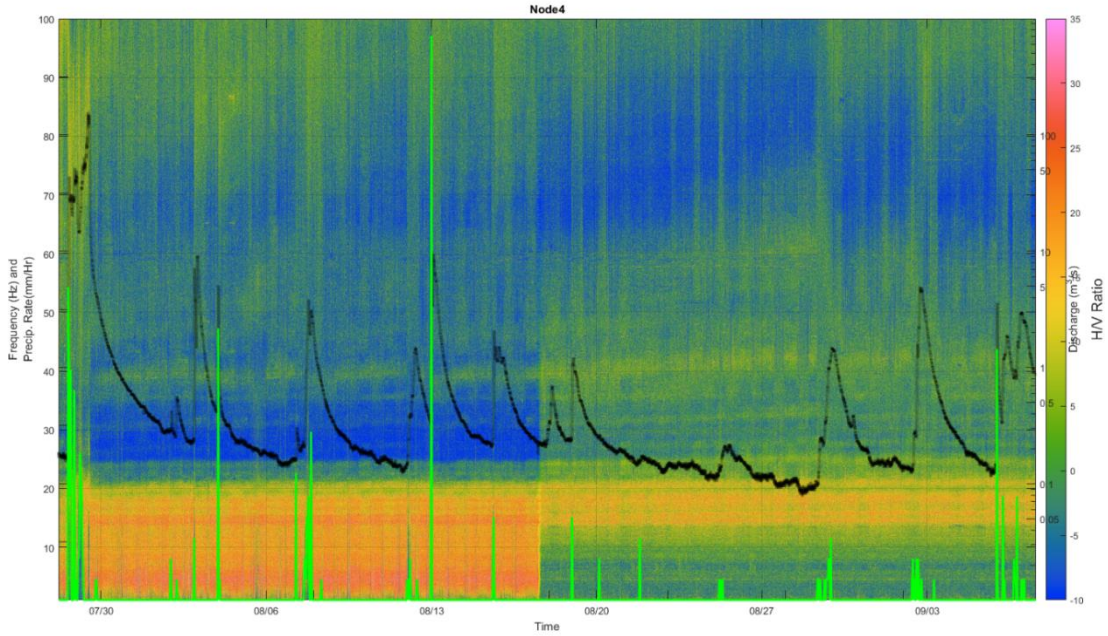

Bibliography

Anthony, R. E., Aster, R. C., Ryan, S., Rathburn, S., and Baker, M. G.: Measuring Mountain River Discharge Using Seismographs Emplaced Within the Hyporheic Zone, Journal of Geophysical Research: Earth Surface, 123, 210-228, 10.1002/2017JF004295, 2018.

Barrière, J., Oth, A., Hostache, R., and Krein, A.: Bed load transport monitoring using seismic observations in a low-gradient rural gravel bed stream, Geophys. Res. Lett., 42, 2294-2301, doi: 10.1002/2015gl063630, 2015.

Bea, R. G.: Preliminary Root Causes Analysis of Failures of the Oroville Dam Gated Spillway, Center for Catastrophic Risk Management, University of California, Berkeley, http://documents.latimes.com/report-finds-serious-design-construction-and-maintenance-defects-oroville-dam-emergency-spillway/, 31, 2017.

Beck, J. L.: Weight-induced stresses and the recent seismicity at Lake Oroville, California, B. Seismol. Soc. Am., 66, 1121, 1976.

Berkeley Digital Seismic Network (BDSN). UC Berkeley Seismological Laboratory. Dataset. doi:10.7932/BDSN, 2017.

Bonnefoy-Claudet, S., Cotton, F., and Bard, P.-Y.: The nature of noise wavefield and its applications for site effects studies: A literature review, Earth-Science Reviews, 79, 205-227, https://doi.org/10.1016/j.earscirev.2006.07.004, 2006.

Burtin, A., Bollinger, L., Vergne, J., Cattin, R., and Nabelek, J. L.: Spectral analysis of seismic noise induced by rivers: A new tool to monitor spatiotemporal changes in stream hydrodynamics, J. Geophys. Res.-Sol. Ea., 113, 14, doi: 10.1029/2007jb005034, 2008.

Burtin, A., J., V., L., R., and P., D.: Location of river-induced seismic signal from noise correlation functions, Geophysical Journal International, 182, 1161--1173, doi: 10.1111/j.1365-246X.2010.04701.x, 2010.

Burtin, A., Cattin, R., Bollinger, L., Vergne, J., Steer, P., Robert, A., Findling, N., and Tiberi, C.: Towards the hydrologic and bed load monitoring from high-frequency seismic noise in a braided river: The "torrent de St Pierre", French Alps, J. Hydrol., 408, 43-53, doi: 10.1016/j.jhydrol.2011.07.014, 2011.

California Department of Water Resources: Water Continues Down Oroville Auxiliary Spillway. 2, http://www.water.ca.gov/news/newsreleases/2017/021117_pm_release_oroville_auxiliary_spillway.pdf, 2017a.

California Department of Water Resources: Oroville Dam LiDAR-Derived Elevation Points. Personal Communication, 2017b.

California Department of Water Resources: Oroville Dam's Auxiliary Spillway Begins Flowing. http://www.water.ca.gov/news/newsreleases/2017/021117spillway_begins_flowing.pdf, 2017c.

California Department of Water Resources: Lake Oroville Releases Slowed to Avoid Erosion. 2, http://www.water.ca.gov/news/newsreleases/2017/021017oroville.pdf, 2017d.

California Department of Water Resources: Department of Water Resources Operations and Maintenance Data Exchange. https://cdec.water.ca.gov/, 2017e.

Chin, A.: Urban transformation of river landscapes in a global context, Geomorphology, 79, 460 - 487, https://doi.org/10.1016/j.geomorph.2006.06.033, 2006

Crampin, S.: Distinctive Particle Motion of Surface Waves as a Diagnostic of Anisotropic Layering, Geophys. J. Roy. Astr. S., 40, 177-186, doi: 10.1111/j.1365-246X.1975.tb07045.x, 1975.

Franca, M. J., and Brocchini, M.: Turbulence in Rivers, in: Rivers-Physical, Fluvial and Environmental Processes, edited by: Rowinski, P., and RadeckiPawlik, A., GeoPlanet-Earth and Planetary Sciences, Springer-Verlag Berlin, Berlin, 51-78, 2015.

Gimbert, F., Tsai, V. C., and Lamb, M. P.: A physical model for seismic noise generation by turbulent flow in rivers, J. Geophys. Res.-Ea. Surf., 119, 2209-2238, doi: 10.1002/2014jf003201, 2014.

Gimbert, F., Tsai, V. C., Amundson, J. M., Bartholomaus, T. C., and Walter, J. I.: Subseasonal changes observed in subglacial channel pressure, size, and sediment transport, Geophys. Res. Lett., 43, 3786-3794, doi: 10.1002/2016gl068337, 2016.

Govi, M., Maraga, F., and Moia, F.: Seismic Detectors For Continuous Bed-Load Monitoring In A Gravel Stream, Hydrolog. Sci. J., 38, 123-132, doi: 10.1080/02626669309492650, 1993.

Haney, M. M., Power, J., West, M., and Michaels, P.: Causal Instrument Corrections for Short-Period and Broadband Seismometers, Seismol. Res. Lett., 83, 834-845, doi: 10.1785/0220120031, 2012.

Hsu, L., Finnegan, N. J., and Brodsky, E. E.: A seismic signature of river bedload transport during storm events, Geophys. Res. Lett., 38, 6, doi: 10.1029/2011gl047759, 2011.

Hunt, S. L., and Kadavy, K. C.: Energy Dissipation On Flat-Sloped Stepped Spillways: Part 2. Downstream Of The Inception Point, Transactions of the Asabe, 53, 111-118, 2010a.

Hunt, S. L., and Kadavy, K. C.: Energy Dissipation On Flat-Sloped Stepped Spillways: Part 1. Upstream Of The Inception Point, Transactions of the Asabe, 53, 103-109, 2010b.

Komatitsch, D., Vilotte, J.-P., Cristini, P., Labarta, J., Le Goff, N., Le Loher, P., Liu, Q., Martin, R., Matzen, R., Morency, C., Peter, D., Tape, C., Tromp, J., and Xie, Z.: SPECFEM2D v7.0.0. Computational Infrastructure for Geodynamics, https://geodynamics.org/cig/software/specfem2d/, 2012.

Komar, P. D.: Selective grain entrainment by a current from a bed of mixed sizes; a reanalysis, Journal of Sedimentary Research, 57, 203-211, 10.1306/212F8AE4-2B24-11D7-8648000102C1865D, 1987.

Koper, K. D., and Hawley, V. L.: Frequency dependent polarization analysis of ambient seismic noise recorded at a broadband seismometer in the central United States, Earthquake Sci., 23, 439-447, doi: 10.1007/s11589-010-0743-5, 2010.

Koper, K. D., and Burlacu, R..: The fine structure of double-frequency microseisms recorded by seismometers in North America, J. Geophys. Res.-Sol. Ea., 120, 1677--1691, doi: 10.1002/2014JB011820, 2015.

Kovesi, P.: Good Colour Maps: How to Design Them, CoRR, abs/1509.03700, 2015.

Langbein, W. B., and Leopold, L. B.: River meanders - Theory of minimum variance, Washington, D.C., Report 422H, H1-H15, 1966.

Leopold, L. B., Bagnold, R. A., Wolman, M. G., and Brush Jr, L. M.: Flow resistance in sinuous or irregular channels, Washington, D.C., Report 282D, 134-, 1960.

Leopold, L. B., and Maddock Jr, T.: The hydraulic geometry of stream channels and some physiographic implications, Washington, D.C., Report 252, 64, 1953.

McLaughlin, K. L., and Jih, R. S.: Finite Difference Simulations of Rayleigh Wave Scattering by 2-D Rough Topography, Air Force Geophysics Laboratory Report AFGL-TR86-0269, Hanscom AFB, MA, 56, 1986.

Maryland State Highway Administration, Internet Traffic Monitoring System (I-TMS), accessed at: http://maps.roads.maryland.gov/itms_public/, 2018.

McNamara, D. E., and Buland, R. P.: Ambient Noise Levels in the Continental United States, B. Seismol. Soc. Am., 94, 1517-1527, doi: 10.1785/012003001, 2004.

Oroville Dam Spillway Incident Independent Forensic Team (ODSIIFT): Preliminary Findings Concerning Candidate Physical Factors Potentially Contributing to Damage of the Service and Emergency Spillways at Oroville Dam (Memorandum), http://www.water.ca.gov/oroville-spillway/pdf/2017/Memorandum_050517.pdf, 3, 2017a.

Oroville Dam Spillway Incident Independent Forensic Team (ODSIIFT): Interim Status Memorandum, 7, 2017b.

Park, J., Vernon, F. L., and Lindberg, C. R.: Frequency-Dependent Polarization Analysis Of High-Frequency Seismograms, J. Geophys. Res.-Solid, 92, 12664-12674, doi: 10.1029/JB092iB12p12664, 1987.

Parker, G., and Klingeman, P. C.: On why gravel bed streams are paved, Water Resources Research, 18, 1409-1423, 10.1029/WR018i005p01409, 1982.

Petit, F., Houbrechts, G., Peeters, A., Hallot, E., Van Campenhout, J., and Denis, A.-C.: Dimensionless critical shear stress in gravel-bed rivers, Geomorphology, 250, 308-320, https://doi.org/10.1016/j.geomorph.2015.09.008, 2015.

Planès, T., Mooney, M. A., Rittgers, J. B. R., Parekh, M. L., Behm, M., and Snieder, R.: Time-lapse monitoring of internal erosion in earthen dams and levees using ambient seismic noise, Géotechnique, 66, 301-312, doi: 10.1680/jgeot.14.P.268, 2016.

Powell, D. M.: Flow resistance in gravel-bed rivers: Progress in research, Earth-Sci. Rev., 136, 301-338, doi: 10.1016/j.earscirev.2014.06.001, 2014.

Prestegaard, K. L.: Bar resistance in gravel bed streams at bankfull stage, Water Resour. Res., 19, 472--476, doi: 10.1029/WR019i002p00472, 1983.

Ringler, A. T., Anthony, R. E., Karplus, M. S., Holland, A. A., and Wilson, D. C.: Laboratory Tests of Three Z-Land Fairfield Nodal 5-Hz, Three-Component Sensors, Seismological Research Letters, 89, 1601-1608, 10.1785/0220170236, 2018.

Roth, D. L., Brodsky, E. E., Finnegan, N. J., Rickenmann, D., Turowski, J. M., and Badoux, A.: Bed load sediment transport inferred from seismic signals near a river, J. of Geophys. Res.-Ea. Surf., 121, 725-747, doi: 10.1002/2015jf003782, 2016.

Roth, D. L., Finnegan, N. J., Brodsky, E. E., Rickenmann, D., Turowski, J. M., Badoux, A., and Gimbert, F.: Bed load transport and boundary roughness changes as competing causes of hysteresis in the relationship between river discharge and seismic amplitude recorded near a steep mountain stream, J. Geophys. Res.-Ea. Surf., 122, 1182-1200, doi: 10.1002/2016jf004062, 2017.

Saucedo, G. J., and Wagner, D. L.: Geologic Map of the Chico Quadrangle, California, Regional Geologic Map No. 7A, 1:250,000 scale California Geological Survey, 1992.

Schmandt, B., Aster, R. C., Scherler, D., Tsai, V. C., and Karlstrom, K.: Multiple fluvial processes detected by riverside seismic and infrasound monitoring of a controlled flood in the Grand Canyon, Geophys. Res. Lett., 40, 4858-4863, doi: 10.1002/grl.50953, 2013.

Schmandt, B., Gaeuman, D., Stewart, R., Hansen, S. M., Tsai, V. C., and Smith, J.: Seismic array constraints on reach-scale bedload transport, Geology, 45, 299-302, doi: 10.1130/g38639.1, 2017.

Tromp, J., Komattisch, D., and Liu, Q.: Spectral-element and adjoint methods in seismology, Commun. Comp. Phys., 3, 32, 2008.

Tsai, V. C., Minchew, B., Lamb, M. P., and Ampuero, J. P.: A physical model for seismic noise generation from sediment transport in rivers, Geophys. Res. Lett., 39, 6, doi: 10.1029/2011gl050255, 2012.

United States Bureau of Reclamation (USBR): Design Standards No. 14: Appurtenant Structures for Dams (Spillways and Outlet Works). In: Chapter 3: General Spillway Design Considerations, 2014.

Weather Underground, Personal Weather Station KMDSILVE44, accessed at: https://www.wunderground.com/personal-weather-station/dashboard?ID=KMDSILVE44#history, 2018

Wilkinson, S. N., Keller, R. J., and Rutherfurd, I. D.: Phase-shifts in shear stress as an explanation for the maintenance of pool–riffle sequences, Earth Surface Processes and Landforms, 29, 737-753, 10.1002/esp.1066, 2004.